

Computer simulation of boundary effects and multiphase flows on the mesoscopic scale

Citation for published version (APA):

Schmieschek, S. M. P. (2015). *Computer simulation of boundary effects and multiphase flows on the mesoscopic scale*. [Phd Thesis 1 (Research TU/e / Graduation TU/e), Applied Physics and Science Education]. Technische Universiteit Eindhoven.

Document status and date:

Published: 01/01/2015

Document Version:

Publisher's PDF, also known as Version of Record (includes final page, issue and volume numbers)

Please check the document version of this publication:

- A submitted manuscript is the version of the article upon submission and before peer-review. There can be important differences between the submitted version and the official published version of record. People interested in the research are advised to contact the author for the final version of the publication, or visit the DOI to the publisher's website.
- The final author version and the galley proof are versions of the publication after peer review.
- The final published version features the final layout of the paper including the volume, issue and page numbers.

[Link to publication](#)

General rights

Copyright and moral rights for the publications made accessible in the public portal are retained by the authors and/or other copyright owners and it is a condition of accessing publications that users recognise and abide by the legal requirements associated with these rights.

- Users may download and print one copy of any publication from the public portal for the purpose of private study or research.
- You may not further distribute the material or use it for any profit-making activity or commercial gain
- You may freely distribute the URL identifying the publication in the public portal.

If the publication is distributed under the terms of Article 25fa of the Dutch Copyright Act, indicated by the "Taverne" license above, please follow below link for the End User Agreement:

www.tue.nl/taverne

Take down policy

If you believe that this document breaches copyright please contact us at:

openaccess@tue.nl

providing details and we will investigate your claim.

COMPUTER SIMULATION OF
BOUNDARY EFFECTS AND MULTIPHASE FLOWS
ON THE MESOSCOPIC SCALE

Sebastian Schmieschek

Cover design: Sebastian Schmieschek
Printing: Ridderprint BV, www.ridderprint.nl

Copyright © 2015 by Sebastian Schmieschek. All rights reserved.

ISBN: 978-94-6299-144-6

COMPUTER SIMULATION OF
BOUNDARY EFFECTS AND MULTIPHASE FLOWS
ON THE MESOSCOPIC SCALE

PROEFSCHRIFT

ter verkrijging van de graad van doctor aan de Technische Universiteit Eindhoven,
op gezag van de rector magnificus, prof.dr.ir. F.P.T. Baaijens, voor een commissie
aangewezen door het College voor Promoties in het openbaar te verdedigen op
woensdag 16 september 2015 om 16:00 uur

door

Sebastian Schmieschek

geboren te Göttingen, Duitsland

Dit proefschrift is goedgekeurd door de promotoren en de samenstelling van de promotiecommissie is als volgt:

voorzitter: prof.dr. H.J.H Clercx
1^e promotor: prof.dr. J.D.R. Harting
2^e promotor: prof.dr. A.A. Darhuber
leden: prof.dr. O.I. Vinogradova (M.V. Lomonosov Moscow State University)
prof.dr. P.V. Coveney (University College London)
prof.dr. F. Toschi
prof.dr. J.H. Snoeijer

The path is the destination

Freely adapted from a Chinese proverb

Contents

1	Introduction	1
1.1	A historical view	1
1.2	Motivation	3
1.3	Outline	5
2	Principles	7
2.1	A short history of fluid dynamics research	7
2.2	Fluid dynamics and kinetic theory	10
2.2.1	The Navier-Stokes equations	10
2.2.2	The Boltzmann equation	12
2.3	Relevant physical properties	14
2.3.1	Transport coefficients	15
2.3.2	Forces and energies	16
2.3.3	Phenomenological properties	17
2.3.4	Dimensionless numbers	20
2.4	The lattice Boltzmann method	23
2.4.1	Lattice Boltzmann multiphase models	26
2.5	Lattice Boltzmann method boundary conditions	28
2.5.1	Periodic boundaries	28
2.5.2	Wall boundary conditions	30
2.5.3	Knudsen regime boundary conditions	32
3	Tensorial slip of channels with anisotropic patterns	35
3.1	Introduction	36

3.1.1	Effective tensorial slip	37
3.1.2	Discussion of parameters and limits	37
3.2	Theory of tensorial slip	38
3.2.1	Relation of slip and permeability	40
3.2.2	Theoretical solutions for effective slip over patterned surfaces	41
3.3	Aspects of LB simulation of anisotropically patterned channels	46
3.3.1	Choice of boundary conditions	47
3.3.2	Scales and parameterisation	47
3.3.3	Spatial resolution and convergence in time	49
3.3.4	Measurement of effective slip	49
3.3.5	Discussion of error	51
3.4	Slip flow in anisotropically patterned channels	52
3.4.1	Stripe pattern in the thin channel limit	52
3.4.2	Stripe pattern in the thick channel limit	55
3.4.3	Stripe pattern in channels of arbitrary height	57
3.4.4	Cosine pattern in the thick channel limit	58
3.5	Drag force on a sphere approaching a slip striped plane	64
3.6	Conclusion and outlook	66
4	A ternary multi-component model for flows in porous media	69
4.1	Introduction	70
4.2	Modelling aspects	71
4.2.1	An amphiphilic fluid component	72
4.2.2	Multi relaxation time collision scheme	73
4.3	Validation	77
4.3.1	Surface tension	77
4.3.2	Wettability	81
4.3.3	Diffusivity	85
4.3.4	Permeability	87
4.4	Forced imbibition of a model porous medium	92
4.4.1	Overview	92
4.4.2	Force variation	93
4.4.3	Wettability variation	94
4.4.4	Surfactant concentration variation	96
4.5	Conclusion and Outlook	97

5	Contaminant transport in dilute gas flows	101
5.1	Introduction	101
5.2	Modelling aspects	104
5.2.1	Lattice Boltzmann methods for intermediate Knudsen flow . .	105
5.2.2	A Monte Carlo Model for Contaminants	106
5.2.3	Parameterisation	109
5.3	Validation	110
5.3.1	Intermediate Knudsen numbers - The LBM implementation . .	112
5.3.2	The Maxwell speed distribution - The coupling algorithm . . .	112
5.3.3	The second law of Fick - Diffusion in a binary mixture with large density contrast	113
5.3.4	The transport equation - The particle boundary condition . . .	115
5.4	Simulation of contaminant suppression by bezels	116
5.4.1	System setup	117
5.4.2	Contaminant suppression	120
5.5	Conclusion and Outlook	121
6	Summary and outlook	125
	Bibliography	129
	List of publications	153
	List of figures	155
	List of tables	163
	Summary	164
	Samenvatting	168
	Acknowledgements	172
	Curriculum vitae	175
	List of Symbols	176

Chapter 1

Introduction

This introductory chapter starts out with a general historical view in the context of the thesis, followed by notes concerned with the motivation of the work presented and closes with an outline of the remainder of the document.

1.1 A historical view

Fluids are all around us and in fact in us as well. From the air we breath to the water sustaining all life on earth, the physics of fluids must have been subject to human curiosity since its very beginning. As every aspect of physics, fluid dynamics has seen exponential growth in insight, application and diversification over the course of the last 300 years [1]. The field of kinetic theory allows today to describe fluids in direct relation to the mechanical properties of their constituting molecules and their statistics. In particular, modern formalisms like the Bogoliubov Born Green Kirkwood Yvon (BBGKY) hierarchy [2–5] allow it to draw a continuous line from classical Hamilton mechanics of particle motion [6] to the Navier-Stokes continuum equations of fluid motion [7,8]. In the course of the paradigm shift towards a particle-centric view of the world, former phenomenological properties have become directly accessible to scientists and engineers [9].

Between the microscopic scale, where transport properties such as diffusivity and viscosity and heat conductance can be modelled according to molecular properties and the macroscopic description viewing a fluid as a continuum, the mesoscopic scale has been defined. The term is used here to designate a scale locally comprising enough particles for thermostatics to be valid and at the same time being fine

grained enough to capture non-continuum effects. This has to be distinguished from the use of mesoscopic physics in the context of quantum mechanics, where the scale is considered to still include quantum effects while this work is only concerned with statistical systems in the classical limit.

In today's fluid dynamics research, the level of complexity has led to the formation of various fields of specialisation, commonly divided along the lines of certain dominant phenomena like e.g. rarefied gas flows [10–13] or turbulence [1, 14]. Other fields of specialisation have been formed through the development of detailed descriptions of the non-ideal, real world such as multiphase flows [9, 15] and complex fluids where next to the fundamental fluid dynamics descriptions, the interplay of different fluids and solids results in different, new physics [15].

Another important aspect of a fluid dynamics description in all fields and on all scales is the formulation of accurate boundary conditions. Given *no-slip* boundary conditions, assuming the relative fluid velocity at a solid boundary is equivalent to the wall velocity, with the Poiseuille and Couette flow exact solutions to the Navier-Stokes equations can be obtained. However this is in general not the case [1, 16] (see section 2.2.1). The applicability of higher order continuum approximations, the *Burnett* and *Super-Burnett* equations [17, 18], suffers from difficulties to formulate boundary conditions at all. This is in part due to the fact that the higher order thermodynamics included here give especially in the boundary layer rise to inherently non-continuous effects, where in the *Knudsen-layer* (see 2.3.4) the kinetic properties of the particles constituting the fluid become dominant [10, 11]. A phenomenon occurring in the early onset of this regime is *slip-flow* (see section 2.3.3), where a fluid is observed to have a non-vanishing velocity relative to a solid boundary [11, 13]. This can also be the case at hydrophobic and super-hydrophobic surfaces, there due to repulsive solid-liquid interactions and entrapped gas, respectively [19, 20]. Moreover, certain multiphase flows can be modelled by means of boundary conditions as well, as it is done in numerical *boundary-* or *interface-tracking* methods [21–24].

Besides deeper theoretical insight and enhanced experimental capabilities, fuelled by new imaging [25–27] and fabrication technology [28–30], computer simulation techniques have made large contributions to the development as well as utilisation of fluid dynamics principles. From meteorology over architecture and mechanical and civil engineering to the life sciences, numerical fluid dynamics models on the micro, meso and macro-scale are an integral part of ongoing research and application. Increasingly accurate models of realist multiphase flow situations have only been enabled recently by the ever growing capabilities of modern microcomputers.

The term Computational Fluid Dynamics (CFD) algorithms [31, 32] commonly refers to solvers for the continuum (Navier-Stokes) equations, but particle based methods are applied to fluid dynamics simulations as well. While the applicability of Molecu-

lar dynamics (MD) simulations, modelling the mechanical equations of motions of all particles, is limited by the reachable time and length scales, so-called *coarse grained* approaches use thermostatics to dramatically reduce the necessary number of simulated particles. An important example in this class, employed for the simulation of rarefied gases, where the continuum approximation does no longer hold, is the Direct Simulation Monte Carlo (DSMC) method [33–35]. In the spirit of the Boltzmann equation representative particles execute free movement and random collisions parameterised by the laws of thermodynamics [33].

Developed from cellular automata [36–38] namely lattice gas automata [39, 40], the lattice Boltzmann method is another example for a coarse grained simulation method based on the statistics of the single particle distribution function formulated in analogy to the Boltzmann equation [38, 41–48] (see sections 2.2.2 and 2.4). Contrary to the DSMC approach it is however originally set up to efficiently solve the Navier-Stokes equations rather than Boltzmann approximations of higher order [45]. Here as well the algorithm is constructed by modelling free movement of particles and binary collisions, they are however executed in terms of a discretised single particle velocity distribution function on a discrete phase space [49]. Owing to the regular discretisation, locality and simplicity of the basic algorithm, the method has become a popular alternative to classical CFD codes and has seen a lot of extension and refinement [38, 46–48, 50]. Additions include turbulence [46, 48, 51–55] as well as multiphase models and phenomenological extensions to account for e.g. thermal fluctuations or rarefied gas properties in the lower Knudsen regime. Moreover the method has been coupled to various other numerical methods. Examples include here different strategies to integrate molecular dynamics particles as well as coupling to finite element and other mesoscopic discrete particle simulation algorithms.

Making use chiefly of the LBM as a Navier-Stokes solver, the work reported here focuses on aspects of dewetting surface interactions and slip modelling as well as the optimisation of a multiphase model for increased boundary accuracy. In the final results chapter a hybrid model integrating aspects of DSMC with LBM is aimed at simulation of the transition regime for non-negligible Knudsen numbers, where e.g. slip flow occurs. The relevance of these investigations is motivated in the next section, followed by a more in-depth outline of the thesis.

1.2 Motivation

In recent years developments in the engineering of functional surfaces and micro electromechanical systems (MEMS) [29, 30, 56, 57] have sparked a renewed interest in a deeper understanding of boundary conditions in fluid dynamics [19, 20]. Superhydrophobic surfaces are created by a combination of hydrophobic material and surface

roughness suitable to entrap gas in the surface and thus create partial slip areas, allowing the fluid to exhibit an effective slip [58–61]. MEMS are promising more efficient analysis of medical and chemical samples in so-called lab on a chip environments [62] with applications for example in stem cell research [63] or detection and identification of microorganisms [64, 65]. Other examples of current application include acceleration sensors used in airbags and mobile phones [66] as well as developments towards parallel micro reactors [67, 68]. Large slip lengths would allow to dramatically increase the efficiency of MEMS by improving flow rates. While early reports of large slip in the order of one micrometer could not be reproduced, it has been found that (super-)hydrophobic or dewetting surfaces indeed can exhibit slip length of several ten nanometers [69]. Ongoing research into a combination of hydrophobic surfaces and electroosmotically driven flow shows however promising results to increase this further [70]. Another area of interest in the field is both active and passive control of flow [71, 72]. In some sense combining the two aspects, this work reports on results into the investigation of patterns of varying slip length suitable to be applied to *bend* flow.

Another field of active research where the boundary condition is of grave importance, is concerned with the investigation of multiphase flows in porous media, where the surface to volume ratio is very large [73–75]. Examples here comprise an array of very different systems, ranging from enhanced oil recovery [76] and carbon dioxide capture over soil processes [77], reactor processes [78–81], filtration [82, 83] and printing [84] to food processing [85]. In most of these applications, besides two or more immiscible fluids like water and oils, components interacting with both of two respective immiscible species are of interest. These solvents and surfactants (SURFace ACTive AgeNTS) are dramatically influencing the behaviour of fluid mixtures [86]. For example in enhanced oil recovery, surfactants are used in a third step to extract oil after first relying on the reservoir pressure and second water injection generated pressure. Once these processes cease to produce oil up to 60 percent of oil remain in the reservoir [76]. This application suits the scope of our implementation very well as there are no reactive flows and no expected strong thermal effects.

In very small channels the continuum approximation made by the Navier-Stokes equation breaks down. The reason for this is that the mean free path of the particles becomes comparable with the typical length scales of the channel and the geometry rather than thermostatics governs the particle movement [10–13]. This regime is commonly referred to as Knudsen regime. Also here, one of the immediate effects is the existence of slip at solid boundaries, further however, the reduction in mean free path introduced by the additional collisions with the wall change the fluid properties at the wall resulting in the so-called Knudsen layer. From the argumentation it is clear that these effects do not only occur for very narrow channels, but very dilute systems as well, where the mean free path becomes very large compared to the geometries as it is the case e.g. in vacuum technology applications [87] or flight in the

outer atmosphere [34]. In current UV lithography machines used in CPU production [88, 89], contaminants emitted by plastic parts of the setup cause *hazing* of the immensely complex optical systems used to produce sharp images on the nanometer scale [90]. To avoid contamination with organic molecules the optics, operated at very low ambient pressures of a few Pascal, are flushed with Hydrogen. The prediction of the efficiency of such efforts has however proven difficult [91].

1.3 Outline

The chapter 2 gives an outline of the scientific context and details on physical processes as well as algorithms and boundary conditions as they are necessary for a closed presentation of the work. Starting from a brief historical discussion, the Navier-Stokes equations are introduced accompanied by an overview of their features and properties. This is followed by a brief introduction of the Boltzmann equation, its relation to general thermostatics as well as some solutions. The physical parameters relevant to the flow problems treated here are introduced and discussed. Starting with some comments on phase space models, the text introduces the lattice Boltzmann method followed by a discussion of its properties and some collision model aspects. Then follows an overview of multiphase extensions to the model, where the pseudo-potential method employed in chapter 4 is discussed in detail. The boundary conditions applied throughout are described with focus on in- and out-flux as well as solid boundary conditions.

In the first results chapter 3, the outcome of work towards the parameterisation and simulation of slip flow in anisotropically patterned channels is reported. Quantitative comparison with theoretical results suggesting the occurrence of tensorial effective slip is successfully made. The introduction describes the theoretical model and its solution as developed in prior research [92–97]. After a discussion of the simulation requirements and optimisations made [98], the results presentation starts out with slip flow over anisotropic surfaces in the thick channel limit where both discrete stripes and sinusoidal patterns are considered. Interesting features in this context are the effective slip as well as properties of the velocity field in the vicinity of the slip boundaries. The chapter closes with discussion of possible extensions of the model.

The following chapter 4 is concerned with an optimisation to a ternary LBM implementation, where a multi relaxation time collision scheme was introduced to improve accuracy and stability of the method for the simulation of flow in porous media. After describing the changes introduced to the model and its implementation, the algorithm is evaluated against standard problems. Here, surface tension, wettability, diffusivity and (relative) permeability are evaluated. As a showcase qualitative simulation results of forced imbibition into a pseudo-2d model porous medium are

presented. Pressure gradient, wettability, surfactant concentration and viscosity contrasts are varied, evaluating the resulting permeability and flow features. Finally, possible future applications and further corrections to the model are discussed.

The final results chapter 5 treats simulations in the intermediate Knudsen regime by means of a new hybrid simulation approach. Starting out with detailing the basic assumptions made in model development as well as discussing coupling aspects of the algorithms, the section goes on with a report of results to important benchmark simulations such as the recovery of the Boltzmann distribution in thermodynamic equilibrium and the accurate quantitative simulation of capture of diffusivity and the transport equation. As a model application for the formalism, contaminant suppression by a low pressure gradient flow through a wall opening is measured. The influence of flow rates and contaminant molecular weight on the suppression coefficient is reported in context of an example experiment reproduction.

The thesis closes with a summary of the presented work, concluding remarks and a discussion of future work suggested by the results.

Chapter 2

Principles

This chapter aims to put the research performed in the scope of this dissertation in context with the current scientific knowledge. It is attempted to give a general overview over the fluid dynamics phenomena considered here as well as to discuss modelling aspects of different approaches of numerical simulation. It is in part based on

H. LIU, Q. KANG, C. R. LEONARDI, B. D. JONES, S. SCHMIESCHEK, A. NARVÁEZ, J. R. WILLIAMS, A. J. VALOCCHI AND J. HARTING.

Multiphase lattice Boltzmann simulations for porous media applications - a review. *In press*, 2015. pre-print available from arXiv:1404.7523 [physics] [50].

2.1 A short history of fluid dynamics research

What is it that makes a fluid *fluid*? A scientific attempt to answer this question has of course to take into account successful models of fluid behaviour. Building on the continuum theory introduced by Euler [99], in the 19th century Navier [7] and Stokes [8] discovered that fluid dynamics can be modelled by assuming mass conservation and Newton's second law being fulfilled by each infinitesimal fluid volume as well as stress being proportional to strain (incompressibility).

The simple nature of the resulting equations (see section 2.2.1) easily betrays their inherent complexity. Employing suitable boundary conditions, exact solutions can be obtained for simple systems such as Poiseuille and Couette flow. In turbulent regimes,

characterised by the dominance of inertial over viscous forces (i.e. high Reynolds numbers, see section 2.3.4) however, the non-linearity of the equations gives rise to effects on numerous scales resulting in chaotic behaviour. The scope of this text will however be limited to non-turbulent flows at low Reynolds numbers [100].

The chapters 3 and 4 of this thesis focus on obtaining and evaluating solutions to the Navier-Stokes equations. The principles employed to obtain these solutions will however be rooted in the broader *kinetic theory* based on the assumption that all macroscopic properties of a fluid are determined by the state of individual particles constituting it [12, 101].

Atomistic views of the world have already been developed in ancient Greece, coining the term of the *indivisible* smallest particles constituting the world. While we today know that this is not the whole truth, this text will deal with classically describable particles at low energies. After the dark ages, Bernoulli was the first to revisit the idea in the eighteenth century, formulating his *Hydrodynamica* using the concept of all matter being comprised of particles and the consequences thereof to describe liquid properties and behaviour [102]. But it would take until the early twentieth century for the idea to reach general acceptance.

Pioneering works along the way include contributions by Lomonosov, Clausius who first introduced the mean free path as a concept [103, 104] and Maxwell formulating the first statistical physics equation to describe the dependency of mean particle velocity on the temperature [105]. Gibbs introduced the ensemble formalism in thermodynamics and did extensive work on free energy [106, 107]. Boltzmann formulated a minimal model for particle movement and collision, assuming only binary collisions independent in time. This allowed him to formulate the Boltzmann equation and derive a generalisation of the Maxwell distribution as well as the so-called H-Theorem providing a rational for entropy growth in thermostatic systems [108]. Einstein and Smoluchowski presented compelling treatments on the theory behind Brownian motion in the early 20th century which finally lead to broad acceptance of an atomistic view of the world [109, 110].

Around the same time Chapman [111, 112] and Enskog [113] independently developed a multivariate expansion of the Boltzmann equation yielding the continuum model expressions. In first order approximation those are the Euler and in second order approximation the Navier-Stokes equations, closing the gap between particle and continuum based fluid descriptions and enabling the extension of the formalism to higher orders as well [17, 18].

The middle of the 20th century saw more attention to kinetic theory, where in 1946 the BBGKY-hierarchy was introduced [2–5], providing solutions to the Liouville equation formulated by Gibbs to describe the phase space continuum of thermodynamic

ensembles in terms of probability distributions of 1, 2 . . . interacting particles. From which it follows that it contains the Boltzmann equation as second order approximation. Bhatnagar, Gross and Krook introduced a linear approximation of the collision operator, sufficient to approximate the Navier-Stokes equations in a regime close to equilibrium [114]. And in 1949, Harold Grad introduced a Hermite expansion method as a means to solve the Boltzmann equation for rarefied gas flows further from equilibrium [12].

Before, far from equilibrium, Knudsen had discovered fascinating effects in rarefied gases not accessible by the Navier-Stokes equations. In particular he observed the *Knudsen paradox* of increasing flow rates with decreasing pressure in very low pressure regimes. Another discovery is a pump relying only on temperature gradients to induce gas flows in rarefied regimes [10, 11]. The Knudsen number (Eq. 2.29), relates the mean free path of the fluid particles to typical length scales of the system. If it cannot be approximated as zero, the individual particles' movement cannot be ignored and the Navier-Stokes equations are not a valid model anymore [10]. Modelling of flow in this regime will be the subject of section 5.

While higher order approximations to the Boltzmann equation may be able to mend these shortcomings and are subject to ongoing research [101, 115, 116], the most promising models for flows in this regime have been developed in the field of numerical simulation.

The most straightforward way to describe a system of interacting classical particles is of course to directly solve all of their equations of motion and thereby implicitly solving the Boltzmann equation. With the advent of microcomputers this ludicrous proposition became thinkable for the first time. Molecular dynamics algorithms modelling particles behaving according to classical mechanics were among the first to be executed [117]. Since then the method has celebrated numerous successes in various fields from chemistry to engineering and there exist many mature, well maintained codes with large user bases [118–120]. Given the typical number of particles given by the Avogadro number in the order of 10^{23} it is however not surprising that even after more than 60 years of exponential growth in computing power and algorithm optimisations the use of such models to solve fluid dynamics problems on relevant time and length scales is still limited to very small systems, e.g. nano-droplets [121].

On the other end of the spectrum of approaches to the simulation of fluid dynamics and traditionally referred to as *computational fluid dynamics* methods are algorithms aiming to solve the Navier-Stokes equations iterative piece wise on a suitably discretised space [31, 32]. Following this principle various algorithms focusing on optimisations for various problems, most prominently turbulence, have been developed [32, 122, 123]. Many mature implementations of the algorithm exist [124–126].

Between the microscopic picture keeping account of every single atom and the macroscopic description of the fluid as a continuum, the insight into the collective properties of particle ensembles provided by thermostatics and in particular kinetic theory allows to take a middle ground commonly called the mesoscopic scale. With respect to the change in resolution stepping down from fully resolved molecular dynamics methods, this regime may also be referred to as *coarse grained*. Here, a host of different methods has been developed including dissipative particle dynamics (DPD) [127], Multi-particle Collision Dynamics (MPC) or Stochastic Rotation Dynamics (SRD) [128], Smooth Particle Hydrodynamics (SPH) [129], lattice Boltzmann methods (LBM) [41–45] and direct simulation Monte Carlo (DSMC) [33].

In the 1980s a class of algorithms named *cellular automata* became popular, which simulated dynamic system behaviour for interacting entities with minimal rule sets [36–38]. One of these, coined *lattice gas automata* simulated particles hopping along the edges of a (hexagonal [39, 40]) lattice and performed momentum conserving collisions when encountering each other [38–40]. It could be shown that this minimalist approach was in fact able to solve the Navier-Stokes equations in two dimensions, given sufficiently large time and spatial scales [40]. The model suffered however from difficulties such as noise and lack of Galileian invariance. To answer these problems, the individual particles were replaced by a projection of the Boltzmann distribution and the approach was subsequently called lattice Boltzmann method [41–45].

The lattice Boltzmann method [38, 41–48] and a variation of the DSMC method [33–35] will be employed in the scope of this thesis.

2.2 Fluid dynamics and kinetic theory

2.2.1 The Navier-Stokes equations

The Navier-Stokes equations are describing momentum conservation in a fluid with respect to any given infinitesimal volume. They have been derived from imposing Newton’s second law for such elements [7, 8]. A general formulation is given by

$$\rho \left(\frac{\partial \mathbf{u}}{\partial t} + \mathbf{u} \cdot \nabla \mathbf{u} \right) = -\nabla p + \nabla \sigma + \mathbf{F}, \quad (2.1)$$

in terms of the mass density ρ , the velocity \mathbf{u} , time t , pressure p , stress σ and body force \mathbf{F} . It relates inertia comprised of a term of local acceleration $\frac{\partial \mathbf{u}}{\partial t}$ and a convective term $\mathbf{u} \cdot \nabla \mathbf{u}$ scaled by the mass density ρ on the left hand side, to a pressure gradient ∇p , viscous stresses $\nabla \sigma$ and additional external forces \mathbf{F} on the right hand side, thus formulating a balance of momentum [130]. In incompressible,

Newtonian fluids $\nabla \mathbf{u} = 0$, and the contribution of viscous stresses can be shown to reduce to a scalar factor in a function of the second spatial derivative in the velocity, $\sigma \Delta \mathbf{u}$, interpretable as a diffusive term of momentum as well (compare sec. 2.3.1). To enable the formalism fully to describe fluid behaviour, mass conservation is assumed, introducing the continuity equation

$$\nabla \cdot \mathbf{u} = 0. \quad (2.2)$$

While numerical methods can produce solutions to these equations, the existence (and smoothness) of a general solution to the Navier-Stokes equation in three dimensions is still to be proven and part of the *Millennium Prize Problems* [16]. In a regime of large Reynolds number (Eq. 2.25), the non-linearity of the equation results in chaotic behaviour, i.e. turbulence [1, 14].

Many extensions as well as simplifications to the equations have been introduced to account for the application to specific systems and states. Of particular interest in the context of this work is the simplification of the model for *Stokes flow* or *creeping flow* for which the inertial terms on the right hand side of equation 2.1 vanish. Assuming in addition constant fluid density which can be interpreted as assuming an isothermal system, the continuity equation is as well reduced to only consider derivatives of the velocity. The equations read then

$$-\nabla p + \nabla \sigma + \mathbf{F} = 0. \quad (2.3)$$

This form of approximation was formulated by Stokes who in his work independent of Navier's focused on viscous effects rather than inertial [8]. It can also be seen as the limit of the equations 2.1 for a vanishing Reynolds number.

To extend the formalism to compressible flows, the continuity equation has to be generalised to include deviations in density to

$$\frac{\partial \rho}{\partial t} + \nabla \cdot (\rho \mathbf{u}) = 0. \quad (2.4)$$

Another important variation from the Navier-Stokes equations is made for the description of complex fluids, where the viscosity in general has to be expressed as a tensor, introducing non-linear strain response into the formalism (see 2.3.1) [130, 131].

Boundary Conditions

In order to formulate solutions to the Navier-Stokes equations as a differential equation, suitable boundary conditions have to be formulated [1, 130] (see sections 2.3.3,

2.5, 3.2.2). Here in principle Dirichlet boundary conditions, giving a variable at a boundary and Neumann boundary conditions giving the normal derivative to a variable at a boundary are to be distinguished. In the context of fluid dynamics this can oftentimes be related to Dirichlet boundary conditions defining the pressure at a boundary and Neumann BC defining velocity or mass flux (see section 2.5). A different kind of boundary conditions is to be applied to solid surfaces in the case of finite surface slip. While the no-slip case can easily be formulated in terms of a velocity of zero, in a partial slip case the effective treatment of parallel and normal components of variables at the boundary has to become anisotropic (see section 3.2.2).

2.2.2 The Boltzmann equation

The Boltzmann equation is a model for the statistical description of particle movement. In the introduction to his publication on a solution to the Boltzmann equation, Harold Grad gives a very concise overview of the formalism in relation to general thermostatics and continuum approximations [12]. A minimal complete introduction can be found for example in [38]. In-depth information on derivation and application of the formalism can be found in [132].

A central feature in Boltzmann's approach is that all particles in a system are in fact interchangeable, implying that all interactions do not depend on former events. This assumption is named *molecular chaos*. A second assumption, the *Stoßzahlansatz* designates the limitation to independent, binary interactions between particles. Together these form the basis for the description of a thermodynamical system based on the dynamics of a single representative. This implies that a model for the complete dynamics of a gas can be formulated entirely in terms of the single particle velocity distribution. The integro-differential equation for the single particle phase space distribution function $f(\mathbf{x}, \mathbf{u}, t)d^3\mathbf{x}d^3\mathbf{u}$, the Boltzmann equation

$$\partial_t f + \mathbf{u}\partial_{\mathbf{x}}f + \frac{\mathbf{F}}{m}\partial_{\mathbf{u}}f = \Omega(f, f), \quad (2.5)$$

describes the probability to find a particle at time t in a phase space volume $d^3\mathbf{x}d^3\mathbf{u}$ as changing over time $\partial_t f$, through movement $\mathbf{u}\partial_{\mathbf{x}}f$ and through acceleration by an external body-force $\frac{\mathbf{F}}{m}\partial_{\mathbf{u}}f$. Therein m is the particle mass. This is balanced by collisions on the right hand side represented in the approximation of independent binary collisions by the collision integral

$$\Omega(f, f) = \int d^3\mathbf{u}_1 \int d\Phi \sigma(\Phi) |\mathbf{u} - \mathbf{u}_1| [f(\mathbf{x}, \mathbf{u}', t)f(\mathbf{x}, \mathbf{u}'_1, t) - f(\mathbf{x}, \mathbf{u}, t)f(\mathbf{x}, \mathbf{u}_1, t)], \quad (2.6)$$

wherein σ is the *collisional cross section* and Φ is the area of the unit sphere. Primes denote post collisional values. The double integral therefore covers all existing particle

velocities \mathbf{u}_1 and collision normals. The repeated use of the distribution designation f emphasises here that both the particle 0 and 1 are of properties *drawn* from the *same* single particle velocity distribution.

While Boltzmann was not able to obtain a closed solution to the original equation, working with its properties allowed him to extract ground breaking results - a general formulation of the Maxwell-Boltzmann distribution of temperature dependent particle equilibrium velocities as well as the H-Theorem, providing a rationale for entropy and the irreversibility of thermodynamical processes [108,132,133]. By taking into account the invariants of the collision integral Ω , it can be shown that distribution functions exist for which it vanishes [132]. One of these is the Maxwell distribution [134]

$$f^{\text{MB}}(\chi, \mathbf{u}, t) = n \left(\frac{1}{2\pi\alpha^2} \right)^{3/2} \exp \left[-\frac{1}{2\alpha^2} (\mathbf{u} - \langle \mathbf{u} \rangle)^2 \right]. \quad (2.7)$$

It is the distribution of a combination of three orthogonal normal distributed variables (i.e. momentum vector components). With the particle density n and the mean velocity $\langle \mathbf{u} \rangle = \frac{1}{n} \int d^3\mathbf{u} \mathbf{u} f(\chi, \mathbf{u}, t)$. Boltzmann extended this result by identifying the thermal molecular speed as the scaling argument

$$\alpha = \alpha^T = \sqrt{\frac{k_B T}{m}}, \quad (2.8)$$

with the Boltzmann constant k_B , temperature T and particle mass m .

Only ten years after Boltzmann's suicide, Chapman and Enskog independently formulated a multivariate expansion in the collisional invariants around a smallness parameter interpretable as the Knudsen number (A measure for the applicability of the continuum approximation formulated as the ratio of the mean free path λ^0 of a particle and a typical system length, details on which are given in section 2.3.4 and section 5.1). This is a valid assumption since the continuum approximation is implying small deviations from thermodynamic equilibrium as well, but is not required for the formalism in general. Thus taking small deviations from the equilibrium distribution 2.7 into account, they were able to devise solutions to the Boltzmann equation turning out to coincide with the continuum approximations. Here, in first order the Euler equation is found. The expansion up to second order produces the Navier-Stokes equations. An important aspect of their work is the direct accessibility of transport coefficients such as the diffusivity (section 2.3.1) in the formalism. In the 1930s Burnett extended the expansion to higher orders [17, 18]. The resulting equations named Burnett and Super-Burnett equations have due to difficulties to formulate boundary conditions however been without broad application [135]. In what is called Chapman Enskog theory the method was extended to multiphase flows as well [9].

Another approach to an approximation of the Boltzmann equation in order to obtain a closed solution has been made by means of expansion of the particle distribution

function in Hermite polynomials by Harold Grad. Using Hermite coefficients as state variables, he finds that without approximations the first significant coefficients are the stresses and heat flow, which treatment he details [12]. He further states that he believes that the approach is able to accurately reproduce higher order thermodynamics in general, something which is still subject of ongoing research [101, 115, 116].

In 1954 Bhatnagar, Gross and Krook introduced a linear approximation for the collision integral which was shown to be sufficient to recover the Navier-Stokes equations for systems close to equilibrium [114]. Introducing a single relaxation time scale τ for a linear approach to equilibrium, the resulting collision operator reads.

$$\Omega(\mathbf{x}, t) = -\frac{1}{\tau} (f(\mathbf{x}, t) - f^{\text{MB}}(\mathbf{x}, t)). \quad (2.9)$$

Here, the assumption of small deviations from the equilibrium imposes an additional restriction to low Mach numbers, necessary for the expansions to accurately recover the Navier-Stokes equations. It has been widely applied as a simplification of the lattice Boltzmann method (see section 2.4) [43, 45].

2.3 Relevant physical properties

An important aspect of modelling physical systems is the balancing of simplification and completeness of an abstraction. The underlying assumptions and limitations of the model determine the applicability of a model here in the same way as the level of complexity which may prohibit a universal approach. In this section the properties and parameters relevant to the employed numerical models, chiefly the LBM with few additions for the DSMC hybrid approach are discussed. In addition to the physical properties dimensionless numbers used for the characterisation of system behaviour are introduced.

Even though the LBM is as derived from the Chapman Enskog expansion in principle weakly compressible [38, 47], incompressible behaviour can be assumed as well. Furthermore, the models employed are isothermal as only small deviations from equilibrium are considered. These limitations imply that heat flux can be neglected as a transport coefficient, leaving viscosity and diffusivity to be discussed.

In the context of multiphase simulations, surface tension or surface energy are the governing properties determining system behaviour. In case of the multi-component pseudo-potential model detailed below, it is modelled as an explicit forcing term proportional to density contrasts.

Finally with contact angles, surface slip and permeability some phenomenological

properties are introduced as they are required for a closed description here.

2.3.1 Transport coefficients

Viscosity

The viscosity of a fluid can be understood as a measure of its response to a given strain rate $\dot{\epsilon}_{kl} = \partial \mathbf{u}_k / \partial x_l$ quantifying the change of deformation. Here and throughout, the Einstein summation convention is applied with lower case Latin letters designating Cartesian coordinate direction indices. It enters the Navier-Stokes equations 2.1 as viscosity tensor in the definition of the deviatoric stress

$$\sigma_{ij} = \boldsymbol{\eta}_{ijkl} \dot{\epsilon}_{kl}. \quad (2.10)$$

In an isotropic Newtonian fluid the viscosity tensor can be shown to have but two degrees of freedom, allowing to formulate it as

$$\boldsymbol{\eta}_{ijkl} = \nu (\delta_{ik} \delta_{jl} + \delta_{il} \delta_{jk}) + \left(\nu^v - \frac{2}{3} \nu \right) \delta_{ij} \delta_{kl}, \quad (2.11)$$

in terms of the kinematic shear viscosity ν measuring the response to shearing deformation and the bulk or volume viscosity ν^v related to volume deformations as e.g. occurring in pressure waves.

Instead of the kinematic shear viscosity, many calculations make use of the dynamic viscosity $\eta = \nu \rho$ which is scaled with the mass density ρ .

Diffusivity

Diffusion is the process moving a substance in direction of a density gradient, leading to equal concentration throughout a system in thermodynamic equilibrium. The diffusivity \mathcal{D} is a parameter for the speed of spreading. The first and second law of Fick defines diffusivity with respect to density gradients in time and space. The first one relates the diffusive flow rate \dot{Q} to the concentration gradient

$$\dot{Q}_i = -\mathcal{D} \frac{\partial n}{\partial x_i}, \quad (2.12)$$

while the second one defines the diffusion equation, with the diffusivity relating the dynamics of the concentration to its second spatial derivative

$$\frac{\partial n}{\partial t} = \mathcal{D} \frac{\partial^2 n}{\partial x_i^2}. \quad (2.13)$$

In section 4.3.3 equation 2.13 is used for the measurement of the mutual diffusivity in binary and ternary mixtures.

The quantitative prediction of diffusivity is in general very complex. Depending on the context different properties can be taken into account for a prediction. A very intuitive approach is given in the context of the mean free path theory. There the (self-)diffusivity, the process observed to equilibrate density fluctuations in a single component fluid (defined via the chemical potential [136]), is considered. It can be shown to be expressible directly proportional to the mean free path λ^0 and mean thermal speed u^T of a substance as

$$\mathcal{D} = \frac{1}{3}\lambda^0 u^T. \quad (2.14)$$

This approximation is however far from accurate in the case of general substance mixtures as is discussed in chapter 5 (see also [9]).

2.3.2 Forces and energies

Body force and pressure

In the scope of the lattice Boltzmann method, a straightforward way to drive a flow is given by applying a constant body force throughout the system. The accuracy of this approach can be impeded by issues arising from discretisation and boundary conditions, as well as low order accurate force integrations [137–139]. In plain channels, a straightforward integration yields however a simple equivalence to a given pressure gradient

$$\nabla p = -\rho F. \quad (2.15)$$

This allows for relative ease in driving flow in our benchmark problems as well as coupling different methods able to express interactions as forces or pressure gradients at an interface.

Surface tension

The physical effect stabilising a free interface is called surface tension. Depending on the point of view it can be expressed as a force per unit length or, as surface energy, rather as an energy per unit area. For fluid systems, both formulations can be shown to be equal, while the formalism of surface energy can also be extended to describe solid surfaces.

Following Gibbs [107], the surface energy

$$\gamma = \left(\frac{\partial G}{\partial A} \right)_{T,V,N} \quad (2.16)$$

is formulated as the change of free energy G with area A for a given temperature T , volume V and particle count N . In section 4.3.1 we evaluate the surface tension via the Young-Laplace equation

$$\Delta p = \gamma k, \quad (2.17)$$

which contains the surface tension as proportionality factor between the Laplace pressure Δp across an interface to its curvature k . The latter is defined as the sum of reciprocals of the principal radii of curvature per surface dimension $k = \sum_i^{D-1} 1/R_i$. In what is called its mechanical definition, the surface tension γ is given by the anisotropy of the normal p^\perp and transversal p^\parallel eigenvalues of the pressure tensor integrated over an interface area A

$$\gamma = \int_A dA p^\parallel - p^\perp. \quad (2.18)$$

2.3.3 Phenomenological properties

Contact angle

The contact angle is an important phenomenological measure for the wetting properties of a surface. It is defined as the angle a droplet surface spans with a solid surface at the contact line. In this definition, neutral wetting can be expressed in terms of a contact angle of $\Theta = \pi$ or 90° while perfectly wetting surfaces exhibit a contact angle of $\Theta = 0$ (0°) a perfectly dewetting surface of $\Theta = 2\pi$ (180°). This phenomenological description can for static force free systems be related to the surface tension γ existing between a solid s , a liquid l and a gas g in a straightforward way by the Young law

$$\Theta = \tan^{-1} \left(\frac{\gamma_{sg} - \gamma_{sl}}{\gamma_{lg}} \right). \quad (2.19)$$

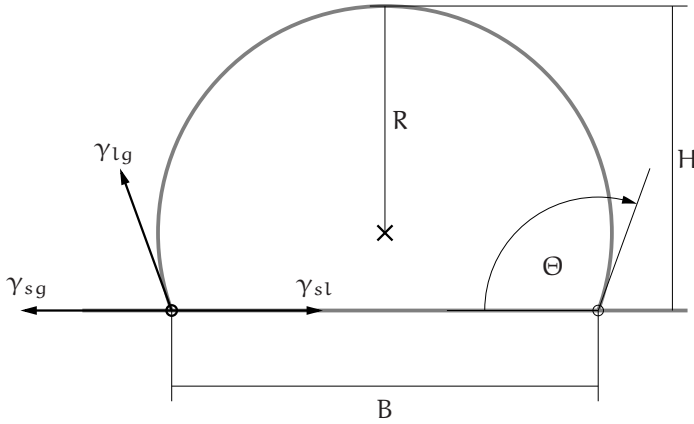


Figure 2.1: Illustration of the static contact angle and Young's law, Eq. (2.19). The contact angle is measured as the inner angle the droplet fluid component encloses with the surface. It can be related to the surface tensions $\gamma_{\alpha\bar{\alpha}}$ acting between the respective phases, solid s , liquid l and gas g . With zero gravity or for sufficiently small droplets, a spherical shape can be assumed. In this case the droplet Radius R and contact angle Θ can be calculated from the droplet base B and droplet height H via Eq. (2.20).

Figure 2.1 illustrates Young's law. Furthermore here the length of the droplet base B and droplet height H are marked. Together with the assumption of a droplet formed as a spherical cap, i.e. neglecting gravity effects (The simulations are free of gravity) these allow to calculate the radius R and contact angle as [140, 141]

$$\Theta = \pi - \tan^{-1} \left(\frac{B/2}{R - H} \right), \quad R = \frac{4H^2 + B^2}{8H}. \quad (2.20)$$

In realistic and application relevant contexts this description, which serves as excellent basic benchmark for our model, falls of course short of capturing additional effects like contact line pinning, surface roughness entrapped gas, effects of gravity or hysteresis, for which more elaborate formulations for the contact angle can be found [142, 143].

Surface slip

As discussed above, the assumption of the no-slip boundary cannot be motivated by first principles. Aware of this, already Navier formulated boundary conditions for the general case of finite velocity of a fluid at a boundary [144]. Here, he identified the

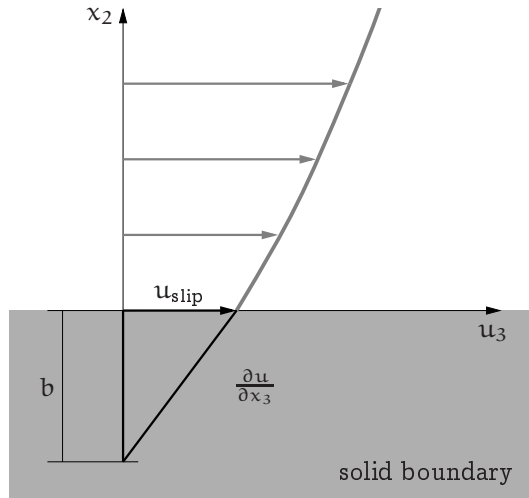


Figure 2.2: *Illustration of the slip boundary condition with the slip length b as introduced by Navier. The slip length is the depth in which linear extrapolation of the surface velocity in relation to the shear stress at the surface hypothetically reaches zero.*

slip-length

$$b = \frac{u_{\text{slip}}}{\left(\frac{\partial u}{\partial x}\right)}, \quad (2.21)$$

relating the speed u_{slip} at a boundary to the shear stress $\frac{\partial u}{\partial x}$, as a good parameter to characterise surface slip as a property independent of the actual flow velocity. It is illustrated in figure 2.2.

A Hagen-Poiseuille equation for the flow velocity in a plain channel adjusted for finite wall slip can be formulated. With regard to the specific situation of systems investigated in chapter 3, the flow velocity profile

$$u_3(y) = \frac{aH^2}{2\eta} \left(\frac{(y-H)^2}{H^2} - \frac{(y-H)+b}{(H+b)} \right), \quad (2.22)$$

in direction z is found. It is a function of the acceleration a over the channel height H in direction y with terms to account for a finite surface slip of b on the channel boundary at $y = 0$ and no-slip at the boundary at $y = H$.

Permeability

The permeability κ , together with viscosity, forms the proportionality factor for the flow rate \dot{Q} of fluid through a medium and an applied pressure gradient ∇p . It is a material property of porous media. It is defined by Darcy's law [145]

$$\dot{Q} = \frac{-\kappa}{\eta} \nabla p, \quad (2.23)$$

which is a phenomenological law derived from measurements in the late 19th century. For the case of fluid mixtures, the relative permeability κ_α^r of a component α is given as ratio of its permeability κ_α in the mixture to the absolute permeability of the medium for a fluid of the same viscosity

$$\kappa_\alpha^r = \frac{\kappa_\alpha}{\kappa}. \quad (2.24)$$

The definition of the property betrays the extraordinary complexity in determining meaningful approximations. Relative permeabilities are depending on the interplay of many parameters ranging from surface wetting, porosity, fluid fractions and percolation to the means driving a flow and hysteresis effects. Surfactants and diffusive effects on longer time scales complicate the modelling even more [75, 146, 147].

2.3.4 Dimensionless numbers

Effects in fluid mechanical systems can be characterised by their governing physical properties. To this extend, many dimensionless numbers have been formulated, allowing the qualitative assessment of system properties by a single number relating the magnitude of different parameters. Table 2.1 gives an overview of dimensionless numbers relevant to the work presented here, together with some values of interest.

The Reynolds number

$$\text{Re} = \frac{\rho u \mathcal{L}}{\eta}, \quad (2.25)$$

relates inertial forces to viscous forces. The former are here quantified by the product of momentum (the product of mass density ρ and mean speed u) and a characteristic length \mathcal{L} , the latter by the dynamic viscosity η . It is a measure for the presence and extend of turbulence in a flow system. Classically, systems are called purely laminar for $\text{Re} \leq 10$ and fully turbulent for $\text{Re} > 2000$ [1]. The systems considered in the scope of this work are always laminar (compare section 2.2.1).

Number	Symbol	Definition	Regimes
Reynolds	Re	$\frac{\text{Inertial forces}}{\text{Viscous forces}}$	Laminar flow: $Re \leq 10$ Fully turbulent flow: $Re > 2000$
Capillary	Ca	$\frac{\text{Viscous forces}}{\text{Surface tension}}$	Gov. surface tension: $Ca \leq 10^{-5}$
Peclét	Pe	$\frac{\text{Advective transport}}{\text{Diffusive transport}}$	Diffusivity negligible: $Pe \gg 1$
Mach	Ma	$\frac{\text{Flow speed}}{\text{Speed of sound}}$	Supersonic/Shock: $Ma \geq 1$ LBGK approx. valid: $Ma \leq 0.03$
Knudsen	Kn	$\frac{\text{Mean free path}}{\text{System length}}$	Continuum approx.: $Kn \approx 0$ Slip flow regime: $Kn \leq 0.1$ Transition regime: $Kn \approx 1$ Free molecular flow: $Kn > 100$

Table 2.1: Overview of some dimensionless numbers and their regimes.

The Capillary number

$$Ca = \frac{\eta \mathcal{U}}{\gamma}, \quad (2.26)$$

relates viscous forces, quantified by the product of the viscosity η with a representative flow velocity \mathcal{U} to surface tension forces. For very small capillary number $Ca \leq 10^{-5}$ a system can be thought of as governed by surface tension effects, while these become negligible for larger values of Ca .

The Peclét number

$$Pe = \frac{\mathcal{U}\mathcal{L}}{\mathcal{D}}, \quad (2.27)$$

relates advective effects given by the product of a typical speed \mathcal{U} and length-scale \mathcal{L} and the diffusivity coefficient \mathcal{D} in order to measure whether diffusivity has to be taken into account. It can be formulated both for mass and heat transport. Here, in the context of isothermal systems, only mass diffusion is of interest.

The Mach number

$$\text{Ma} = \frac{u}{c_s}, \quad (2.28)$$

relates the mean speed u in a system to the speed of sound in the material c_s . Its transition through 1 is designating transition to a super-sonic regime where shock wave effects become important. Certain lattice discretisations and collision approximations used in the LBM require it to be small for the Chapman Enskog expansion to recover the Navier-Stokes equations.

The Knudsen number

$$\text{Kn} = \frac{\lambda^0}{\mathcal{L}}, \quad (2.29)$$

is relating the mean free path λ^0 of the molecules constituting a fluid to a typical length scale \mathcal{L} of the system taken into consideration. In order for continuum approximations to be fully valid it has to vanish. Systems exhibiting finite Knudsen numbers include dilute gas flows (compare as well section 5) or small geometries [13].

The most prominent macroscopic effect exhibited by flows at a finite Knudsen number is the breakdown of the hydrodynamic (no-slip) boundary condition at a solid surface. A consequence of this *Knudsen Paradox* is that the flow rate through a thin pipe of radius r , resulting from a fixed pressure gradient ∇p does not linearly decrease with the mean pressure p but rather exhibits a minimum once the mean free path λ^0 associated with the pressure p becomes of the order of r ($\text{Kn} \approx 1$) [10]. Another interesting feature of this non-intuitive regime allows to construct a pump without moving parts as a temperature gradient in a thin pipe is found to induce a pressure gradient [11].

Both phenomena can be explained by the existence of a boundary layer in which discontinuities in velocity- and temperature fields exist. This *Knudsen layer* can extend to the order of several mean free paths from a boundary. In this region, the collision rate between fluid particles is reduced. This is due to the collisions between particles and the surface. As the ratio drops, it reaches a threshold beyond which a local equilibrium description of the flow is void. While this has no implications for the validity of the kinetic picture of the Boltzmann equation, the linear relations for shear stress and heat flux assumed in the formulation of the Navier-Stokes equations are no longer valid. However different strategies can be employed to recover working macroscopic models. For the *slip flow regime* at Kn of the order of 0.1 the integration of slip flow boundary conditions into the Navier-Stokes formalism is possible [148]. Up to the so called *transition regime*, starting at Kn of the order

of 1, higher order approximations of the Boltzmann equation or moment equations of the single particle velocity distribution can constitute analytical solutions to some flow fields and provide valuable information about the transport properties in the system [12, 149–151]. Systems comprising flows at Knudsen numbers of an order of $\text{Kn} \geq \mathcal{O}(10)$ require in general discrete particle models to be correctly resolved. As directly solving the Boltzmann equation due to the high dimensionality and general complexity remains a formidable task, models of the transition regime rely on numerical methods. For *free molecular flow* at even higher Knudsen numbers $\text{Kn} > 100$, collision-less Boltzmann models are employed in which kinetic particle interactions are neglected altogether [152].

2.4 The lattice Boltzmann method

The lattice Boltzmann equation was originally formulated as extension of a lattice gas formalism [41–45, 153], but can be derived directly from the Boltzmann equation by discretisation in time and phase space as well [49, 154]. For a k -dimensional lattice comprising $k - 1$ discrete velocities \mathbf{c}_k and a rest-vector, it reads

$$f_k(\mathbf{x} + \mathbf{c}_k \Delta t, t + \Delta t) - f_k(\mathbf{x}, t) = \Omega_k(\mathbf{x}, t). \quad (2.30)$$

Furthermore the formalism requires a discretised formulation of the Maxwell Boltzmann distribution of particle velocities in thermodynamic equilibrium. Throughout this thesis, an expansion to third order

$$f_k^{\text{eq}} = w_k \rho \left[1 + \frac{1}{c_s^2} \mathbf{c}_k \cdot \mathbf{u} + \frac{1}{2c_s^4} (\mathbf{c}_k \cdot \mathbf{u})^2 - \frac{1}{2c_s^2} |\mathbf{u}|^2 + \frac{1}{2c_s^6} (\mathbf{c}_k \cdot \mathbf{u})^3 - \frac{1}{2c_s^4} (\mathbf{c}_k \cdot \mathbf{u}) |\mathbf{u}|^2 \right],$$

is employed, which has been shown to increase numerical stability in combination with the ternary multi-component model described in detail below. Therein the lattice weights w_k and the speed of sound c_s are determined by the lattice discretisation chosen [43, 155]. Figure 2.3 shows the widely used so-called D3Q19 lattice of $Q = 19$ velocities, comprising 18 discrete velocity vectors \mathbf{c}_k and a zero velocity in $D = 3$ dimensions with implementation specific indexing

$$\mathbf{c} = \begin{bmatrix} 1 & -1 & 0 & 0 & 0 & 0 & 1 & -1 & 1 & 1 & -1 & -1 & -1 & 0 & 0 & 0 & 0 & 0 \\ 0 & 0 & 1 & -1 & 0 & 0 & 1 & -1 & 0 & 0 & 1 & -1 & 0 & 1 & 1 & -1 & -1 & 0 \\ 0 & 0 & 0 & 0 & 1 & -1 & 0 & 0 & 1 & -1 & 0 & 0 & 1 & -1 & 1 & -1 & -1 & 0 \end{bmatrix}.$$

It will be employed throughout the work presented here, their values are given by

$$w_k = \begin{cases} k = 1 \dots 6: & 1/18 \\ k = 7 \dots 18: & 1/36 \\ k = 19: & 1/3 \end{cases} \quad (2.31)$$

Here, indices $1 \dots 6$ designate the main axes, $7 \dots 18$ the vectors pointing to the centre of the edges of a cube and vector 19 is the rest vector of zero length.

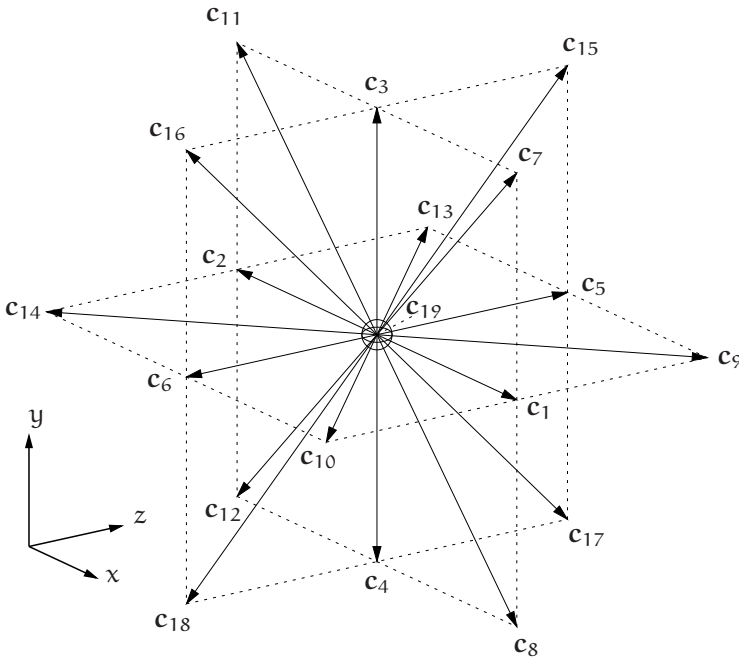


Figure 2.3: The so-called D3Q19 lattice, comprising 19 velocities in 3 dimensions. Illustration adapted from [156].

The speed of sound is given by:

$$c_s = \frac{1}{\sqrt{3}} \frac{\Delta x}{\Delta t}, \quad (2.32)$$

with the lattice constant of discretisation, the length Δx and the modelled time-step Δt . Typically these units are chosen as unity. They do however indicate the entry points for conversion to SI-units as well.

Physical properties can be expressed as moments of the discretised single particle velocity distribution f . Of central interest are the conserved moments, the density given by the zeroth order moment

$$\sum_{\mathbf{k}} f_{\mathbf{k}}(\mathbf{x}, t) = \rho(\mathbf{x}, t), \quad (2.33)$$

and the momentum given by the first order moment

$$\sum_{\mathbf{k}} f_{\mathbf{k}}(\mathbf{x}, t) \mathbf{c}_{\mathbf{k}} = \rho(\mathbf{x}, t) \mathbf{u}(\mathbf{x}, t). \quad (2.34)$$

The shear stress is given by the second order moment

$$\sum_k f_k(\mathbf{x}, t) c_k^i c_k^j \approx \rho(\mathbf{x}, t) T \delta_{ij} + \rho(\mathbf{x}, t) u_i(\mathbf{x}, t) u_j(\mathbf{x}, t), \quad (2.35)$$

wherein the term $\rho(\mathbf{x}, t) T \delta_{ij}$ represents the pressure of a non-ideal gas [157]. In the usual athermal interpretation of the model this is equivalent to the equation of state below, relating the temperature parameter to the lattice speed of sound.

The above discussion has left out the complexity of the collision term. In 1954, Bhatnagar, Gross and Krook published a very simple and elegant model for collision processes in gases, relying on the assumption that all collision processes serve to approach thermodynamic equilibrium. By introducing a single relaxation time scale, this yields the so called BGK, or discretised - lattice BGK (LBGK) collision operator

$$\Omega_k(\mathbf{x}, t) = -\frac{\Delta t}{\tau} (f_k(\mathbf{x}, t) - f_k^{\text{eq}}(\mathbf{x}, t)). \quad (2.36)$$

It has been shown to provide above properties and is for many systems a sufficient approximation to allow to calculate solutions to the Navier-Stokes equation up to second order. The Chapman Enskog expansion requires here a small Mach number (compare Eq. 2.28) with respect to the lattice speed of sound, Eq. 2.32.

In the LBGK approximation this fixes the viscosity, which is determined by the relaxation time τ by

$$\nu = c_s \Delta t \left(\frac{\tau}{\Delta t} - \frac{1}{2} \right), \quad (2.37)$$

where kinematic shear viscosity ν and bulk viscosity ν^v are equal.

The equation of state for the case of a single component fluid system is simply

$$p = c_s^2 \rho. \quad (2.38)$$

It is equivalent to the isothermal ideal gas equation. Naturally model extensions for non-ideal fluids and multiphase flows will introduce additional terms here.

Another algorithm to model particle collisions in the framework of the lattice Boltzmann model is given by so-called multiple-relaxation-time (MRT) models. Conceptually similar to Grad's 13 moment method for the approximation of the Boltzmann equation, this approach performs relaxation on various time-scales in a space formed by a subset of moments of the single particle velocity distribution function [158–160].

2.4.1 Lattice Boltzmann multiphase models

Already around the time of its perception, the LBM was extended to include multiple phases [161], building on a multiphase model introduced for lattice gas models, already [162]. From there, a number of different multiphase models with different strengths and limitations has been devised [161, 163–168]. Here, different principle approaches can be discriminated, the most commonly employed models are the *colour-field models* [161, 169–172], *pseudo-potential models* [163, 164, 173–178], *free-energy models* [165, 166, 179–181, 181, 182], *mean-field models* [167, 168, 183, 184] and hybrid models employing e.g. the immersed boundary methods [21, 185] or level-set methods [22] for interface tracking.

Colour-field Originally devised for the simulation of binary immiscible fluids in the context of lattice gas automata [161], so-called *colour-field* models for the LBM have been extended to model arbitrary number of fluid components [161, 169–172]. In addition to separate velocity distributions for the respective components, the dynamics of an order-parameter field are modelled, resulting in sharp interfaces compared to e.g. the free-energy and pseudo-potential models. The collision operator comprises additional terms to the LBGK model, namely a perturbation step introducing a surface tension term into the model, as well as a recolouring step instating phase separation for a minimal interface thickness. The original algorithms has here been modified to recover correct two-phase NS equations and surface tension [172, 186]. Also the original recolouring approach, assuming maximal work of the recolouring operator has been modified, greatly improving the range of stability and Galileian invariance of interactions [171].

Free-energy Based on the phase-field model, the free-energy functional approach to multiphase and multi-component LB methods introduces interfacial interaction in a thermodynamically consistent formulation [165, 166, 187]. In the multi-component formulation, in addition to a velocity density field, an order parameter field is evolved on the LB lattice. Introducing conservation laws and suitable equilibrium distributions the formalism can be shown to recover the NS equations. By comparison to free-energy models, direct parameterisation by thermodynamic properties is possible [187]. Extensions of the model include modifications to instate Galileian invariance [179, 180] and increase the achievable density ratios by modification of the interface integration [181, 181, 182]. Recently, the formulation has been shown to be algorithmically equivalent to inter-particle potential models, where the latter are however parameterised phenomenologically (see also below) [188].

Mean-field theory So-called mean-field models are based on employing a velocity density distribution and an additional order parameter evolved on a lattice of the same discretisation as well [167, 168, 183, 184]. Instead of the free-energy functional, in these models the interaction is calculated from inter-molecular interactions. While this approach is in general numerically more robust than colour-field and free-energy models as well as the pseudo-potential method, it is quite limited in the achievable density gradients between the components just the same.

The Shan and Chen pseudo-potential method

In 1993 Shan and Chen introduced a simple efficient way to qualitatively simulate multiphase fluid phenomena. To simulate multiple fluid components they introduced a two-fold coupling relying on the modification of the equilibrium velocity used to calculate the equilibrium distribution, Eq. (2.4).

The first modification required is the definition of a collective equilibrium velocity \mathbf{u}_Φ of Φ components in the absence of interactions. It is calculated as the ratio of the summed local momentum over the summed local mass density as

$$\mathbf{u}_\alpha = \mathbf{u} = \frac{\sum_\alpha m^\alpha \sum_k \mathbf{c}_k f_k^\alpha}{\sum_\alpha m^\alpha \sum_k f_k^\alpha}, \quad (2.39)$$

which can be shown to correctly model a mixture behaving as an ideal gas [43, 45]. Therein m^α is the molecular mass and f_k^α is the density of the single particle distribution function on the k th lattice vector.

In a second step an inter-component potential is defined as $\Psi = \mathcal{G}_{\alpha\bar{\alpha}}\psi^\alpha\psi^{\bar{\alpha}}$. This general formulation is simplified by limiting interactions to nearest neighbour lattice sites and choosing the green function $\mathcal{G}_{\alpha\bar{\alpha}}$ to be approximated by a scalar value. For thermodynamic consistency [164] the density dependent pseudo-potential is chosen to be

$$\psi^\alpha = 1 - e^{-\rho^\alpha}. \quad (2.40)$$

The momentum change imposed by this definition of a potential can then be formulated as the force

$$\mathbf{F}^\alpha(\mathbf{x}, t) = \mathcal{G}_{\alpha\bar{\alpha}}\psi^\alpha(\mathbf{x}, t) \sum_k w_k \psi^{\bar{\alpha}}(\mathbf{x} + \mathbf{c}_k \Delta t, t). \quad (2.41)$$

The modified momentum equation for a component α then reads

$$\rho_\alpha \mathbf{u}_\alpha = \rho_\alpha \mathbf{u} + \tau_\alpha \mathbf{F}^\alpha. \quad (2.42)$$

While this implies that local momentum is not conserved anymore, it was shown that the global conservation of momentum is still assured by this approach [163].

This method can be applied two-fold to yield either a phase transition within a single fluid component as well as to simulate a system of immiscible components. The respective behaviour is determined by the coupling parameter $\mathcal{G}_{\alpha\bar{\alpha}}$. If it is chosen to be negative, thus implying attractive interactions, a van der Waals like behaviour is observed and for coupling above a critical value a phase transition towards a liquid and a steam phase can be observed. For repulsive interactions the miscibility of fluid components is determined by the coupling strength again in a fashion to exhibit phase separation above a critical coupling value.

A major drawback of this phenomenological approach is the absence of a proper energy formulation. The model is still isothermal or even athermal and energy conservation laws cannot be formulated. From this it is clear that while phase transitions are modelled, there is no dynamic temperature model included here.

Later extensions of the formalism include multi-range interactions, allowing to tune the surface tension independently from the phase separation governing order parameter [177, 178, 189].

Further theoretical investigation of the formalism has produced solutions to the pressure tensor resulting from the model. Here it could be shown that the formulation is equivalent to free energy multi-component models [190].

Stability and accuracy has been improved by reformulating the force integration as well as modifications of the potential [175, 176]

2.5 Lattice Boltzmann method boundary conditions

2.5.1 Periodic boundaries

The most basic boundary condition commonly applied to domain boundaries in the LBM are periodic boundary conditions. They are implemented by copying the lattice velocity density values of lattice vectors pointing out of the simulated domain to their inwards pointing counterparts on the domain opposite boundary and vice versa. In one Cartesian coordinate x for a domain comprising $1..n \times$ lattice sites this reads

$$\mathbf{c}_k(x = 1) = \mathbf{c}_k(x = nx), \quad \text{where} \quad \chi(\mathbf{c}_k) = 1 \quad (2.43)$$

and

$$c_k(x = nx) = c_k(x = 1) \quad \text{where} \quad x(c_k) = -1 \quad (2.44)$$

The local nature of the lattice Boltzmann formalism requires the application of this condition in general only to be applied in the advection step. The resulting system resembles an infinite array of identical copies of the domain in x -direction. This simple approach conserves mass and momentum and can be apply in any number of Cartesian coordinates. Furthermore, the combination with other boundary conditions such as the bounce-back BC (sec. 2.5.2) and on-site-velocity BC (sec. 2.5.2) is straightforward when executed in the right order (periodic BC first).

When nearest neighbour information is required by elements of the algorithm, such as in the calculation of the pseudo-potential force Eq. 2.41, it becomes more convenient to not only copy the minimal required data(sub-)set but rather create copies of the lattice sites on the opposite domain boundary, sometimes referred to as halo or ghost layers - a strategy also employed in domain decomposition in parallelised systems. The computational domain is then extended beyond the physical boundaries, allowing to otherwise keep the algorithm kernel unmodified, e.g.

$$f(x = 0) := f(x = nx) \quad \wedge \quad f(x = nx + 1) := f(x = 1). \quad (2.45)$$

In this case the existence of a halo layer on either side of a simulation domain already anticipates the need for full site information in these regions as it arises e.g. for the calculation of Shan Chen interaction forces. More simplified cases may reduce to communicate a minimal half-set of velocities and that in one direction only. Of course on the other end of the spectrum kernels requiring information from yet extended shells might require to even further extend the halo region. Another possible motivation for this is the optimisation of parallel algorithms for minimal numbers of communication operations (The information provided by a five lattice site deep halo remains accurate at the physical domain boundary for four time steps).

While periodic boundaries allow for enormous gains in efficiency when dealing with inherently periodic problems such as the patterned surfaces treated in section 3 or the simple Poiseuille flow benchmarks in section 4.3.4, in general close attention has to be paid to avoid artefacts introduced into a system due to periodicity. For example, the droplets used for surface tension and contact angle measurement in section 4.3 may in a too small domain interact with their mirror counterparts and coalesce to form lamellae and films. As well, the jet-like outflow of the bezel opening in section 5 would have the potential to disturb the homogeneous inflow if periodic boundaries were employed there. In these cases the use of periodic boundaries may, in order to minimise or avoid artefacts, require the simulation of significantly larger domains than the problem size initially suggests.

2.5.2 Wall boundary conditions

As motivated above, appropriate treatment of boundaries is essential for the successful modelling of fluid flow. The choice of boundary condition to be employed in a numerical model depends here on different aspects. First, of course the quality of surface properties to be included in the model has to be taken into account. The range of parameters includes here without limitation for example no-slip vs. slip boundary conditions [156, 191–197], wettability [61, 198, 199], static vs. moving boundaries [200–204], resolution of curvature [200, 205] and inclination with respect to the discretisation axes [206, 207] as well as Knudsen layer correction beyond the slip flow regime, typically introducing additional wall functions which take effect beyond the immediate boundary layer [193, 196, 208–215].

Simple mid-grid bounce back boundary condition

Originally developed in the context of lattice gas models, bounce-back boundary conditions provide a straightforward way to model solid surfaces imposing no-slip at a wall [216–218]. As the name suggests this is achieved by reflecting velocity components pointing into the boundary *back* into the inverse parallel direction, rendering the resulting mean velocity zero. In case of the simple mid-grid bounce back this is implemented by modifying the advection step such that

$$f_{\mathbf{k}}(\mathbf{x} + \mathbf{c}_{\mathbf{k}}t, t + 1) = f_{\bar{\mathbf{k}}}(\mathbf{x} + \mathbf{c}_{\mathbf{k}}t, t), \quad (2.46)$$

where $\mathbf{c}_{\mathbf{k}}$ points towards a site defined as boundary and the index $\bar{\mathbf{k}}$ signifies the inverse direction $\mathbf{c}_{\bar{\mathbf{k}}} = -\mathbf{c}_{\mathbf{k}}$. The resulting plane of zero velocity is then located *mid-grid* between the centre of the fluid and boundary node. In LBGK models the exact wall position is however depending on the relaxation time and especially for under-relaxed systems at high values of τ the error growing super-linear with it becomes large [219, 220]. A context in which this can lead to significant error is the simulation of porous media [139, 160]. Computational constraints here oftentimes lead to small features being resolved by a few lattice sites only which dramatically increases the relative error [221]. Multi relaxation time collision models allow, given adequate parameterisation [222], to eliminate the viscosity dependence of the boundary position, while more sophisticated bounce back boundary conditions implementing interpolation schemes allow to reduce the error [160, 223]. In the scope of this work it was opted to integrate MRT collisions in order to preserve the simplicity of the bounce back scheme, especially in the light of the straightforward combination with multi-phase boundary conditions (see section 2.5.2).

Pseudo-potential interactions

The prudential interaction model described in section 2.4.1 can not only be employed to introduce non-ideal terms into the equation of state, but also offers an elegant way of adding fluid solid interactions to a system [224]. Here, in addition to the simple mid-grid bounce back boundary condition used to close the surface, a wall potential is defined simply as

$$s = \begin{cases} 0 & \text{: fluid} \\ 1 & \text{: solid} \end{cases} \quad (2.47)$$

Then in the calculation of pseudo-potential interaction for the fluid component α an additional interaction is taken into account. It is quantified by the force

$$\mathbf{F}^{\alpha\omega}(\mathbf{x}, t) = \mathcal{G}_{\alpha\omega} \psi^\alpha(\mathbf{x}, t) \sum_k w_k s(\mathbf{x} + \mathbf{c}_k \Delta t, t) \quad (2.48)$$

proportional to a new scalar wall interaction parameter $\mathcal{G}_{\alpha\omega}$ which can be interpreted as surface tension.

In single component systems, repulsive interaction of this type has been used to model dewetting surfaces exhibiting slip [225]. In single component multiphase models, the strength of attractive interaction determines whether the surface will behave wetting or dewetting for the liquid phase. If the coupling is chosen in the order of the attractive self-interaction of the minority phase dewetting behaviour will be induced, while for coupling strengths in the order of the liquid phase self interaction, wetting will be observed.

In chapter 4 two interaction parameters $\mathcal{G}_{\alpha\omega}$ and $\mathcal{G}_{\bar{\alpha}\omega}$ are introduced allowing to vary the contact angle Θ to be varied according to independent solid-fluid surface tension of the respective components. Here identical static contact angles can for example be achieved by difference in relative positive surface tension as well as positive to negative surface tension.

On-site velocity boundary conditions

A remarkable feature of the LBM is the direct access to the stress tensor local to a lattice site via the non-equilibrium part of the distribution

$$f^{\text{neq}} = f - f^{\text{eq}} \quad (2.49)$$

By combining this knowledge with a bounce-back scheme for the equilibrium portion of the distribution and using the conservation laws, Qisu Zou and Xiaoyi He arrived

at an elegant formulation for Dirichlet (pressure) boundary conditions and Neumann (velocity) boundary conditions for the LBM [226]. In combination, the two variants allow furthermore to fix the mass flow, a property used in the contaminant suppression simulations in section 5.4.

Originally formulated for D2Q9 lattices as well as D3Q15 lattices using both compressible and incompressible LBM formulations, the approach was subsequently extended to D3Q19 lattices [227, 228] and arbitrary flow orientation [156]. In order to achieve this, explicit correction terms for the transverse momentum had to be introduced. Details of the formalism used in this work are found in [156]. Since the ansatz relies on the continuity equation, Eq. 2.4 to hold, it is not sound to combine these boundary conditions with the pseudo-potential multiphase model, as it does in general not conserve local momentum.

A consequence of the extension to arbitrary flow orientation is the applicability of the formalism not only to inflow and outflow boundaries, but to solid boundaries as well. Here again, access to the stress tensor allows not only to formulate an on-site no-slip boundary condition, but enables the calculation of arbitrary slip flow velocities for a given slip length as the only free parameter as well [156, 229]. By introducing a *inverse accommodation coefficient* ζ varying between 0 in the case of no-slip, interpretable as stochastic limit of diffusive reflection and 1 in the case of full slip, resembling specular reflection on the lattice, the resulting slip length is found to be approximated by [229]

$$b = \frac{\lambda\zeta}{3(1-\zeta)}. \quad (2.50)$$

Evaluations show a remarkable accuracy of this formulation, allowing to tune slip lengths at the order of millions of lattice sites in systems resolved by only hundreds of lattice sites (see section 3.3.4). The boundary condition is used to simulate the slip properties in superhydrophobic striped channels in chapter 3.

2.5.3 Knudsen regime boundary conditions

As detailed in section 2.3, for flows in systems either at very low pressure or of geometry on the nanometer scale the characteristic dimensionless number, the Knudsen number Kn becomes none negligible. For $Kn > 0.01$ rarefaction effects gain noticeable influence on the flow characteristics and slip at the walls has to be taken into account [213]. Thus, to correct the lattice BGK (LBGK) Navier-Stokes solver for the discontinuous velocity field in the Knudsen layer, a slip boundary condition proposed by Zhang *et al.* [230] has been implemented. Other suitable boundary condition modifications were proposed by amongst others Tao *et al.* [213], Ansumali and

Karlin [196, 231] and Toschi and Succi who extended the Ansumali Karlin treatment by virtual collisions in the bulk [211]. Here, so-called wall-function approaches introduce phenomenological corrections either to the entire distribution calculation in the boundary layer, or its parameterisation. While Ansumali and Karlin and Toschi *et al.* chose to modify the equilibrium distribution function, in the scope of this thesis an approach proposed by Zhang *et al.* is used, modifying the relaxation parameterisation or effective viscosity at the boundary by adjusting it according to a Knudsen number in a LBGK model.

In the work conducted for this thesis a two-fold boundary modification is implemented, combining a slip boundary condition with the wall function correcting for the variable mean free path in the boundary layer outlined above. The first employed boundary condition allows to control the reflective behaviour and thereby implicitly the slip by an accommodation parameter α defined between $\alpha = 0$ relating to no-slip or *bounce-back* and $\alpha = 2$ implementing full-slip or *specular reflection*. In the simulations described in the scope of this work, an accommodation parameter of $\alpha = 1$ is chosen. This corresponds to model diffuse deflection at a rough wall, respectively [230]. As with higher Kn and/or increase in resolution the Knudsen layer extends to scales resolved by the simulation, simple slip boundary conditions overestimate the velocity at the boundary. The reason for this is a significant reduction in the mean free path of particles in the vicinity of a surface, effectively lowering the local Knudsen number. Recently, several methods have been introduced to reflect this by the introduction of an effective mean free path λ_e . Integrations with the lattice Boltzmann method have been introduced by Ansumali and Karlin, Tao *et al.*, Hyodo *et al.* and Zhang *et al.* [196, 213–215].

These boundary conditions are detailed and applied in chapter 5 to model the flow of a background gas. Evaluations of the proposed methods have shown the more elaborate phenomenological approaches to allow to reach higher Knudsen numbers than the model used here. The advantage of the given approach lies however in its relative simplicity - Beyond the input of a local relaxation parameterisation no modifications of the algorithms are necessary in order to account for the effective viscosity resulting from the shortened mean free path at the boundary. At the same time the algorithm works well in the considered low intermediate Knudsen range.

Chapter 3

Tensorial slip of channels with anisotropic patterns

The content of this chapter is based on

S. SCHMIESCHEK, A. V. BELYAEV, J. HARTING AND O. I. VINOGRADOVA.
Tensorial slip of superhydrophobic channels.
Physical Review E, 85:016324, 2012. [98]

and

E. S. ASMOLOV, S. SCHMIESCHEK, J. HARTING AND O. I. VINOGRADOVA.
Flow past superhydrophobic surfaces with cosine variation in local slip length.
Physical Review E, 87:023005, 2013. [232]

where all simulation data were contributed, as well as

A. L. DUBOV, S. SCHMIESCHEK, E. S. ASMOLOV, J. HARTING AND O. I. VINOGRADOVA.
Lattice-Boltzmann simulations of the drag force on a sphere approaching a superhydrophobic striped plane.
The Journal of Chemical Physics 140:034707, 2014. [233]

where simulations were supervised.

3.1 Introduction

Recent advances in the engineering of functional surfaces on the microscopic level [58–61] and their integration into micro electromechanical devices (MEMS) [29, 30, 56, 57] spark renewed interest in hydrodynamic boundary conditions [19, 234]. On the micro and nanometer scale, slip flow is identified not only in the Knudsen regime of very dilute and/or confined systems, but in hydrophobic and superhydrophobic systems as well [13, 29, 30, 56, 57]. Experimental and numerical investigations suggest here that the observed slip is in fact an effective property, emerging from the interplay of different system aspects, such as electromagnetic and/or chemical interactions, roughness and gas entrapment [60, 61, 235]. In the light of these results, theoretical models have been constructed which introduce effective local slip lengths of smooth surfaces to allow for a simplified treatment of complex hydrodynamic problems [19, 92, 234, 236, 237]. An example is the application to the *Cassie-Baxter-state* of superhydrophobic surfaces [238, 239], where gas entrapped in surface roughness features leads to very high contact angles and large contact angle hysteresis. Furthermore comparably large slip has been reported, making this state particularly interesting for engineering applications [240].

While the treatment of isotropic patterns has been shown to be exactly solvable in general, recent work has been aimed at models for anisotropically patterned surfaces. The most basic abstract model for this case is given by a pattern of stripes, introducing anisotropy in exactly one dimension. An interesting feature in this case is the applicability of such surface structures to not only optimise flow rates [96, 241], but also to *bend* flow, relevant in flow control as well as aiding passive mixing applications [97, 242].

In the following, effective slip over a striped surface is introduced as a tensorial property of a channel [92] with a discussion of applications of theoretical models in different limits of the governing parameters [98]. In section 3.2.1 the tensorial nature of the effective slip is motivated by comparison to the permeability of a channel exhibiting slip [92]. Section 3.2 outlines some general solution strategies for anisotropic flow problems and presents solutions to selected problems used in comparison with simulations in the section 3.4.

Section 3.3 is central to the work presented in that it discusses aspects relevant to the numerical investigations performed in the scope of this thesis. It comprises the selection of boundary conditions, derivation of numerical system scales and related parameters as well as criteria for convergence and error estimation in the context of different measurement techniques.

The chapter closes with the presentation of simulation results and their comparison

with theoretical predictions in the cases of stripe slip patterns in the thick and thin channel limit as well as a cosine varying slip pattern in the thick channel limit (section 3.4). Aspects of boundary modelling aiming at simulation of atomic force microscope systems are introduced as they are drawing from the results presented earlier [233]. Finally, a general summary and outlook of the chapter is given.

3.1.1 Effective tensorial slip

In earlier work, the concept of effective slip is exploited for *thick* (compared to the texture characteristic length, L) channels [56, 243]. For anisotropic textures, it is shown to depend on the direction of the flow and to be a tensor [236], $\mathbf{b}_{\text{eff}} \equiv \{b_{ij}^{\text{eff}}\}$, representable by a symmetric, positive definite 2×2 matrix

$$\mathbf{b}_{\text{eff}} = \mathbf{S}_{\Theta} \begin{pmatrix} b_{\text{eff}}^{\parallel} & 0 \\ 0 & b_{\text{eff}}^{\perp} \end{pmatrix} \mathbf{S}_{-\Theta}, \quad (3.1)$$

diagonalized by a rotation with angle Θ

$$\mathbf{S}_{\Theta} = \begin{pmatrix} \cos \Theta & \sin \Theta \\ -\sin \Theta & \cos \Theta \end{pmatrix}. \quad (3.2)$$

For all anisotropic surfaces its eigenvalues $b_{\text{eff}}^{\parallel}$ and b_{eff}^{\perp} correspond to the fastest (largest forward slip) and slowest (smallest forward slip) orthogonal directions [236]. In the general case of arbitrary flow orientation, inclined by an angle Θ , this means that the flow past such surfaces becomes misaligned with the driving force. This tensorial slip approach, based on a consideration of a *macro scale* fluid motion instead of solving hydrodynamic equations at the scale of the individual pattern, is supported by statistical diffusion arguments [236], and has recently been justified for the case of Stokes flow over a broad class of periodic surfaces [244].

The effective slip formalism represents a useful tool to quantify properties of superhydrophobic surfaces in thick and thin channels. In many situations however dramatic changes in flow can be observed in the critical regime between the two limiting cases, when the length scales of system height H and pattern length L are of the same order. Besides the limiting cases, section 3.2 thus includes a generalisation of the definition of the effective slip length tensor Eq. (3.1) to an *arbitrary* channel thickness as well [98].

3.1.2 Discussion of parameters and limits

Effective slip in a thick channel is a characteristic of a heterogeneous interface only (being expressed through its parameters, such as local slip lengths, fractions of phases,

and a texture period) [97,237]. Recently it was recognised and justified in the context of theory of heterogeneous porous materials [92], that a similar concept of effective slip can be also exploited for a flow conducted in a *thin* channel with two confining surfaces separated by a distance $H \ll L$. In such a situation, a natural definition of the effective slip length can be based on the permeability of a hypothetical uniform channel with the same flow rate. The *effective* tensorial slip is then determined by flow at the scale of the channel width, and in particular depends on the channel height H [92]. Thus, a so formulated effective boundary condition reflects not only parameters of the liquid-solid interface, but also depends on the flow configuration [97,98].

Further limits in the theoretical model can be identified by comparison of the pattern period length L and the local partial slip length b , where it is found that the system behaviour is governed by the respective smallest of the parameters of local partial slip b , periodicity length L and channel height H , where the no-slip fraction ϕ_1 and inflow angle Θ present additional variables for the stripe slip patterned surfaces. In the case of cosine variation of the local slip length, instead of ϕ_1 the mean slip b_0 and amplitude of the variation b_1 are considered. This is elaborated on in the next section.

There are furthermore results in the so-called weakly slipping stripe case in the thick channel limit reported. This case where the slip lengths are very small in comparison with system geometry parameters are originally discussed by Asmolov et al. [245].

3.2 Theory of tensorial slip

The basic assumptions of the theoretical model developed by collaborators in the group of Olga I. Vinogradova are as follows. A channel consisting of two parallel walls located at $y = 0$ and $y = H$ and unbounded in the x and z directions as sketched in Fig. 3.1 is considered. The upper plate is a no-slip hydrophilic surface, and the lower plate is a superhydrophobic surface. The origin of coordinates is placed in the plane of the liquid-gas interface in the centre of the region of partial slip. The x axis is defined along the pressure gradient. This (superhydrophobic vs. hydrophilic) geometry is relevant for various setups, where the alignment of opposite textures is inconvenient or difficult. Moreover such a geometry allows to avoid the gas bridging and long-range attractive capillary forces [246], which appear when dealing with interactions of two hydrophobic solids [247,248].

A superhydrophobic plate is modelled as a flat interface with no meniscus curvature, so that the superhydrophobic surface appears as perfectly smooth with a pattern of boundary conditions [94,96,237]. In this idealisation, by assuming a flat interface,

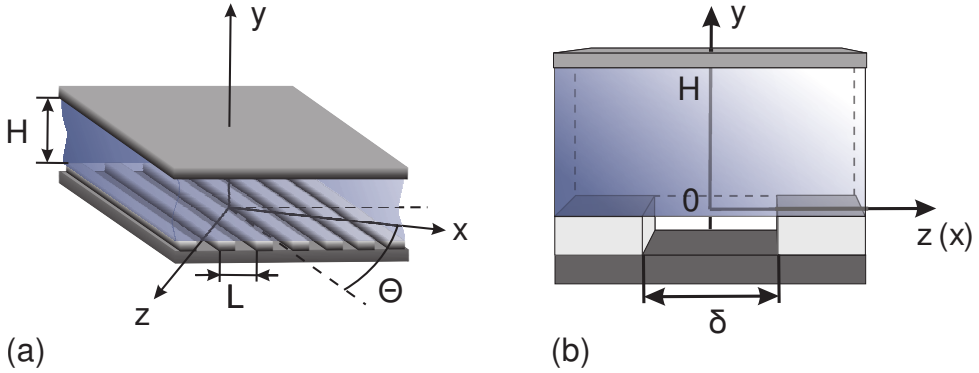


Figure 3.1: Sketch of a slip stripe surface (a): $\Theta = \pi/2$ corresponds to transverse stripes, whereas $\Theta = 0$ to longitudinal stripes; (b) situation in (a) is approximated by a periodic cell of size L , with equivalent flow boundary conditions on the gas-liquid and solid-liquid interfaces. Illustration as published in [98], courtesy of A. V. Belyaev.

additional mechanisms for dissipation connected with the meniscus curvature are neglected [249–251]. It may however be argued that in the limit of laminar flow an adjustment of the assumed partial slip length in the gas/liquid area could account for such effects when evaluating experimental data.

The flow is governed by the Stokes equation 2.3 and incompressible continuity equation 2.2, where assuming unit mass a pressure gradient is introduced by a constant acceleration in x -direction

$$\langle \nabla p \rangle = (-a, 0, 0). \quad (3.3)$$

The local slip boundary conditions at the walls are defined as

$$\mathbf{u}(x, 0, z) = b(x, z) \cdot \frac{\partial \mathbf{u}}{\partial y}(x, 0, z), \quad u_y(x, 0, z) = 0, \quad (3.4)$$

$$\mathbf{u}(x, H, z) = 0, \quad u_y(x, H, z) = 0. \quad (3.5)$$

Here the local slip length $b(x, z)$ at the striped surface is in general a function of both lateral coordinates.

At the striped surface $b(x, z)$ is comprised of a no-slip ($b_1 = 0$) portion over solid/liquid areas and partial slip ($b_2 = b$) over the regions of gas/liquid interface. The length δ is of typical scale of gas/liquid areas. The fraction of the solid/liquid areas is denoted $\phi_1 = (L - \delta)/L$, and of the gas/liquid areas $\phi_2 = 1 - \phi_1 = \delta/L$, respectively.

In case of the cosine varying slip, a one-dimensional periodic texture with the local slip length

$$b = b_0 + 2b_1 \cos(2\pi y) \quad (3.6)$$

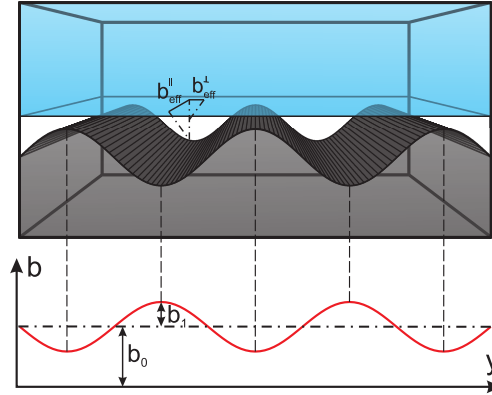


Figure 3.2: Sketch of a surface with a cosine relief and its equivalent representation in terms of flow boundary conditions. Illustration as published in [232], courtesy of E.S. Asmolov.

is considered. The coefficients therein are required to satisfy $b_0 \geq 2b_1 \geq 0$, in order to obey $b(y) \geq 0$ for any y .

The resulting effective slip length in each case is the slip length

$$b_{\text{eff}} = \frac{\langle u \rangle}{\left\langle \left(\frac{\partial u}{\partial y} \right) \right\rangle}, \quad (3.7)$$

determined from the mean values in the xz -plane denoted by $\langle \dots \rangle$.

3.2.1 Relation of slip and permeability

For anisotropic textures different ways exist to define an effective slip length. A natural approach is to define a slip-length tensor by evaluating the permeability of a channel exhibiting slip flow

$$\kappa^{\parallel, \perp} = \frac{H^3}{12} \left(1 + \frac{3b_{\text{eff}}^{\parallel, \perp}}{H + b_{\text{eff}}^{\parallel, \perp}} \right), \quad (3.8)$$

utilising the analogy with a hypothetical, uniform channel. This definition was introduced and justified for thin superhydrophobic channels, using the lubrication limit [92].

Considering a situation where the direction of largest forward slip of an anisotropic texture is inclined at an angle Θ to the pressure gradient, the downstream effective

permeability of the channel can be expressed in terms of the effective downstream slip length as

$$k_{\text{eff}}^{(x)} = \frac{H^3}{12} \left(1 + \frac{3b_{\text{eff}}^{(x)}}{H + b_{\text{eff}}^{(x)}} \right). \quad (3.9)$$

Following [236], it can also be obtained from the permeability tensor:

$$k_{\text{eff}}^{(x)} = \frac{k^{\parallel} k^{\perp}}{k^{\parallel} \sin^2 \Theta + k^{\perp} \cos^2 \Theta} \quad (3.10)$$

By substituting Eq. (3.8) into Eq. (3.10) and after subtracting the latter from Eq. (3.9) the effective downstream slip length tensor can be written in terms of its respective eigenvalues of largest and smallest slip length as

$$b_{\text{eff}}^{(x)} = \frac{b_{\text{eff}}^{\perp} H + 4b_{\text{eff}}^{\parallel} b_{\text{eff}}^{\perp} + (b_{\text{eff}}^{\parallel} - b_{\text{eff}}^{\perp}) H \cos^2 \Theta}{H + 4b_{\text{eff}}^{\parallel} - 4(b_{\text{eff}}^{\parallel} - b_{\text{eff}}^{\perp}) \cos^2 \Theta}. \quad (3.11)$$

Note that $b_{\text{eff}}^{(x)}$ does generally depend on H and $b_{\text{eff}}^{\parallel, \perp}(H)$. For this reason, $b_{\text{eff}}^{(x)}$ cannot be viewed as a *local* property of the surface, except for in the thick channel limit. Rather it is the effective slip length of the channel and thus in general its *global* characteristic.

3.2.2 Theoretical solutions for effective slip over patterned surfaces

To illustrate the general theory, this section focuses on flat patterned surfaces consisting of periodic stripes, where the local (scalar) slip length b varies only in one direction. The problem of flow past striped superhydrophobic surfaces has previously been studied in the context of a reduction of pressure-driven forward flow in thick [93–95] and thin [92] channels, and it is directly relevant for mixing [97, 242], and the generation of tensorial electro-osmotic flow [97, 252, 253]. The formalism is based on an ansatz for effective boundary conditions [97] and represents a theory for an arbitrary gap, which in the asymptotic limits describes the situation in thin and thick channels, respectively. Here merely sketches of the necessary steps to obtain the expressions for effective slip as needed for the comparison with simulation results are given, the interested reader finds details in [95, 98, 232, 245].

For transverse stripes, the velocity $\mathbf{u} = (u(x, y), v(x, y), 0)$, can be described by two components $u(x, 0) = b(x)u_y(x, 0)$, and $v(x, 0) = 0$. For longitudinal stripes, the flow is also two dimensional: $\mathbf{u} = (u(y, z), v(y, z), 0)$, $u(0, z) = b(z)u_y(0, z)$, and $v(0, z) = 0$. As the problem is linear in \mathbf{u} , a solution can be expressed as

$$\mathbf{u} = \mathbf{u}_0 + \mathbf{u}_1, \quad (3.26)$$

Property	Limits	Approximation
$b_{\text{eff}}^{\parallel}$	$H \ll L$	$b_{\text{eff}}^{\parallel} \Big _{H \rightarrow 0} = \frac{bH\phi_2}{H + b\phi_1}. \quad (3.12)$
$b_{\text{eff}}^{\parallel}$	$H \ll L,$ $b \ll L$	$b_{\text{eff}}^{\parallel} \Big _{H \ll b, L} \simeq \frac{\phi_2}{\phi_1} H \propto H \quad (3.13)$
$b_{\text{eff}}^{\parallel}$	$H \ll L,$ $b \gg L$	$b_{\text{eff}}^{\parallel} \Big _{b \ll H \ll L} \simeq b\phi_2 \propto b. \quad (3.14)$
b_{eff}^{\perp}	$H \ll L$	$b_{\text{eff}}^{\perp} \Big _{H \rightarrow 0} = \frac{bH\phi_2}{H + 4b\phi_1}. \quad (3.15)$
b_{eff}^{\perp}	$H \ll L,$ $b \ll L$	$b_{\text{eff}}^{\perp} \Big _{H \ll b, L} \simeq \frac{1}{4} \frac{\phi_2}{\phi_1} H \propto H, \quad (3.16)$
b_{eff}^{\perp}	$H \ll L,$ $b \gg L$	$b_{\text{eff}}^{\perp} \Big _{b \ll H \ll L} \simeq b\phi_2 \propto b. \quad (3.17)$
$b_{\text{eff}}^{(x)}$	$H \ll L$	$b_{\text{eff}}^{(x)} \simeq \frac{H\phi_2}{4\phi_1} \frac{4\phi_2 + \phi_1 + 3\phi_1 \cos^2 \Theta}{4\phi_2 + \phi_1 - 3\phi_2 \cos^2 \Theta}. \quad (3.18)$

Table 3.1: *Thin channel limit solutions of dual series (3.28), (3.29) and (3.30), (3.31) for the effective slip length tensor $b_{\text{eff}}^{(x)}$ and its maximum $b_{\text{eff}}^{\parallel}$ and minimum b_{eff}^{\perp} eigenvalues for channels with stripe slip pattern [98]. Considered are the limits of the channel height H and additional relations of local partial slip b and periodicity length L . The tensorial slip is governed by the respective smallest parameter. Additional parameters are the no-slip surface ratio ϕ_1 and partial slip surface ratio ϕ_2 as well as the inflow inclination Θ with respect to the pattern orientation.*

where \mathbf{u}_0 is the velocity of the usual no-slip parabolic Poiseuille flow

$$\mathbf{u}_0 = (u_0, 0, 0), \quad u_0 = -\frac{\sigma}{2\eta} y^2 + \frac{\sigma H}{2\eta} y \quad (3.27)$$

Property	Limits	Approximation
$b_{\text{eff}}^{\parallel}$	$H \gg L$	$b_{\text{eff}}^{\parallel} \simeq \frac{L}{\pi} \frac{\ln \left[\sec \left(\frac{\pi\phi_2}{2} \right) \right]}{1 + \frac{L}{\pi b} \ln \left[\sec \left(\frac{\pi\phi_2}{2} \right) + \tan \left(\frac{\pi\phi_2}{2} \right) \right]} \quad (3.19)$
$b_{\text{eff}}^{\parallel}$	$H \gg L,$ $b \ll L$	$b_{\text{eff}}^{\parallel} \Big _{b \ll L \ll H} \simeq b \frac{\ln \left[\sec \left(\frac{\pi\phi_2}{2} \right) \right]}{\ln \left[\sec \left(\frac{\pi\phi_2}{2} \right) + \tan \left(\frac{\pi\phi_2}{2} \right) \right]} \propto b \quad (3.20)$
$b_{\text{eff}}^{\parallel}$	$H \gg L,$ $b \gg L$	$b_{\text{eff}}^{\parallel} \Big _{L \ll b, H} \simeq \frac{L}{\pi} \ln \left[\sec \left(\frac{\pi\phi_2}{2} \right) \right] \propto L \quad (3.21)$
b_{eff}^{\perp}	$H \gg L$	$b_{\text{eff}}^{\perp} \simeq \frac{L}{2\pi} \frac{\ln \left[\sec \left(\frac{\pi\phi_2}{2} \right) \right]}{1 + \frac{L}{2\pi b} \ln \left[\sec \left(\frac{\pi\phi_2}{2} \right) + \tan \left(\frac{\pi\phi_2}{2} \right) \right]} \quad (3.22)$
b_{eff}^{\perp}	$H \gg L,$ $b \ll L$	$b_{\text{eff}}^{\perp} \Big _{b \ll L \ll H} \simeq b \frac{\ln \left[\sec \left(\frac{\pi\phi_2}{2} \right) \right]}{\ln \left[\sec \left(\frac{\pi\phi_2}{2} \right) + \tan \left(\frac{\pi\phi_2}{2} \right) \right]} \propto b \quad (3.23)$
b_{eff}^{\perp}	$H \gg L,$ $b \gg L$	$b_{\text{eff}}^{\perp} \Big _{L \ll b, H} \simeq \frac{L}{2\pi} \ln \left[\sec \left(\frac{\pi\phi_2}{2} \right) \right] \propto L \quad (3.24)$
$b_{\text{eff}}^{(x)}$	$H \gg L$	$b_{\text{eff}}^{(x)} \simeq \left(b_{\text{eff}}^{\parallel} - b_{\text{eff}}^{\perp} \right) \cos^2 \Theta + b_{\text{eff}}^{\perp} \quad (3.25)$

Table 3.2: Thick channel limit solutions of dual series (3.28),(3.29) and (3.30),(3.31) for the effective slip length tensor $b_{\text{eff}}^{(x)}$ and its maximum $b_{\text{eff}}^{\parallel}$ and minimum b_{eff}^{\perp} eigenvalues for channels with stripe slip pattern [98, 245]. In addition, relations of local partial slip b and periodicity length L are considered. The tensorial slip is governed by the respective smallest parameter out of b , H and L .

and \mathbf{u}_1 is the slip-driven superimposed flow.

For the case of longitudinal stripes, the flow is homogeneous in x -direction and periodic in z -direction, leaving the perturbation \mathbf{u}_1 with a single non-zero component in x -direction. It can be determined by solving the Laplace equation with the appropriate boundary conditions. Making use of the Fourier method, a trigonometric dual series

$$\begin{aligned} \alpha_0 \left(1 + \frac{b}{H}\right) + \sum_{n=1}^{\infty} \alpha_n [1 + b\lambda_n \coth(\lambda_n H)] \cos(\lambda_n z) \\ = b \frac{\sigma H}{2\eta}, \quad 0 < z \leq \delta/2, \end{aligned} \quad (3.28)$$

$$\alpha_0 + \sum_{n=1}^{\infty} \alpha_n \cos(\lambda_n z) = 0, \quad \delta/2 < z \leq L/2, \quad (3.29)$$

where

$$\alpha_0 = P_0; \quad \alpha_n = P_n(1 - e^{-2\lambda_n H}), \quad n \geq 1$$

is obtained, which provides a complete description of the hydrodynamic flow and effective slip. Simplified solutions to limits in the different scales are given in table 3.1 for the thin channel limit and table 3.2 for the thick channel limit, respectively. Details on the derivation and numerical solution can be found in [98] and references given there. Moreover the weakly slipping stripe solutions in the thick channel limit, Eqs. (3.20),(3.23) are discussed by Asmolov et al. [245].

For flow over transverse stripes, the calculation is more involved, making use of the stream function and vorticity vector to solve the flow perturbation in two dimensions. The principal strategy however remains the same. Using periodicity of the problem and boundary conditions, a trigonometric dual series

$$\begin{aligned} \alpha_0 \left(1 + \frac{b}{H}\right) + \sum_{n=1}^{\infty} \alpha_n [1 + 2b\lambda_n V(\lambda_n H)] \cos(\lambda_n x) \\ = b \frac{\sigma H}{2\eta}, \quad 0 < x \leq \delta/2, \end{aligned} \quad (3.30)$$

$$\alpha_0 + \sum_{n=1}^{\infty} \alpha_n \cos(\lambda_n x) = 0, \quad \delta/2 < x \leq L/2, \quad (3.31)$$

is obtained by the Fourier method. Herein,

$$\alpha_0 = P_0; \quad \alpha_n = \frac{\cosh(2\lambda_n H) - 2\lambda_n^2 H^2 - 1}{\lambda_n H^2} P_n, \quad n \geq 1$$

and

$$V(t) = \frac{\sinh(2t) - 2t}{\cosh(2t) - 2t^2 - 1}. \quad (3.32)$$

Its evaluation in terms of the limits in the respective scales is given in table 3.1 for the thin channel limit and table 3.2 for the thick channel limit.

If the stripes are inclined at an angle Θ , the effective slip length of the channel, $b_{\text{eff}}^{(x)}$ can be calculated with Eq. (3.11), making use of the solutions to the Eigenvalues detailed above.

It is noteworthy that the thin channel limit $b_{\text{eff}}^{(x)}$ does not depend on b , being a function of only H and the fraction of gas/liquid area. At small b according to Eqs. (3.14) and (3.17), $b_{\text{eff}}^{\parallel} \simeq b_{\text{eff}}^{\perp} \simeq b_{\text{eff}}^{(x)}$, so that the flow becomes isotropic.

In the limit of a thick channel and sufficiently large local slip, equation (3.11) can be simplified to define the downstream effective slip length, equation 3.25. In the limit of perfect local slip this can be further simplified to

$$b_{\text{eff}}^{(x)} \simeq b_{\text{eff}}^{\perp} (1 + \cos^2 \Theta). \quad (3.33)$$

Using Eqs. (3.20) and (3.23) it is found that the flow is isotropic $b_{\text{eff}}^{\parallel} \simeq b_{\text{eff}}^{\perp} \simeq b_{\text{eff}}^{(x)}$ if b is much smaller than the texture period.

The initial approach to the application of a cosine modulated slip length follows the same idea of introducing a perturbation component to the flow field which is subsequently solved by Fourier analysis and either consideration of convergence in limiting cases or solution by general numerical methods for linear systems under boundary conditions.

In the limit of large slip, $b_0 > 2b_1 \gg 1$, an asymptotic solution can be constructed, giving the effective slip eigenvalue

$$b_{\text{eff}}^{\parallel} = \sqrt{b_0^2 - 4b_1^2}. \quad (3.34)$$

This same ansatz can further be evaluated to obtain an expression for the velocity gradient

$$\frac{\partial u}{\partial z} = -\frac{2t_1 \exp(-2\pi z) [\cos(2\pi y) - q \exp(-2\pi z)]}{s}, \quad (3.35)$$

which can be integrated over z to give

$$u = -\frac{t_1}{2\pi q} \ln s, \quad (3.36)$$

with the parameters

$$\begin{aligned} q &= \frac{-(b_0/b_1) + \sqrt{(b_0/b_1)^2 - 4}}{2}, \\ t_1 &= \frac{b_1}{b_0 + qb_1}, \\ s &= 1 - 2q \cos(2\pi y) \exp(-2\pi z) + q^2 \exp(-4\pi z). \end{aligned}$$

For the transverse configuration it was found in [254] that the velocity components for the transverse configuration can be expressed in terms of the longitudinal one calculated for twice larger local slip, $u_2 = u [2b(y)]$

$$v_{\text{slip}} = \frac{u_2}{2}, \quad (3.37)$$

Using (3.37) the same expression for the effective slip is derived

$$b_{\text{eff}}^{\perp} = b_{\text{eff}}^{\parallel} = \sqrt{b_0^2 - 4b_1^2}. \quad (3.38)$$

Considering the velocity, the values q, t_1, s remain the same for a twice larger local slip length since they depend on the ratio b_1/b_0 alone. As a result, the obtained velocity perturbation term reads

$$u_2 = u = -\frac{t_1}{2\pi} \ln s,$$

and the additional components of the velocity vector are given by

$$\begin{aligned} v &= -\frac{t_1}{4\pi q} \ln s - \frac{zt_1 \exp(-2\pi z) [\cos(2\pi y) - q \exp(-2\pi z)]}{s}, \\ w &= \frac{zt_1 \exp(-2\pi z) \sin(2\pi y)}{s}. \end{aligned} \quad (3.39)$$

3.3 Aspects of LB simulation of anisotropically patterned channels

The successful verification of a theoretical framework is dependent on different aspects. After assessing the suitability of a method and determining appropriate boundary conditions, in general some effort is required to understand the quantitative relation of scales in the theoretical and numerical context in order to instate comparability. This goes hand in hand with the evaluation of measurement techniques to access the properties in question in the simulation data. Lastly, throughout the whole process sufficient resolution of a problem has to be ensured, balancing it with computational cost constrictions.

As detailed above, the theoretical model taken into consideration here is concerned with the solution of pressure driven Stokes flow in smooth channels under different velocity boundary conditions. While many simulation methods have the ability to simulate this quite minimal model system, the LBM offers some advantages over other methods. Efficient fluid dynamics solvers have to be parameterised with the exact theoretical boundary conditions. The LBM on the other hand by means of local boundary conditions allows to observe an emergent solution based on kinetic

theory assumptions. The local nature of the boundary conditions also implies that the resolution and convergence related errors and limits obtained in the framework of this evaluation can henceforth be applied in the context of arbitrary geometries.

3.3.1 Choice of boundary conditions

Within the LB method a common approach to describe the interaction between hydrophobic surfaces and the fluid is by means of a repulsive force term [191, 199, 249, 255, 256]. This force applied at the boundary can be linked to the contact angle to quantitatively describe the wettability of materials [140, 141, 199, 257]. Alternatively, slip can be introduced by generalising the no-slip bounce-back boundary conditions in order to allow specular reflections with a given probability [194, 195, 213], or to apply diffuse scattering [196, 197, 258]. The method applied here follows the latter idea and uses a second order accurate on-site fixed velocity boundary condition to simulate wall slippage, as introduced in section 2.5.2.

To adjust the parameterisation of the simulation to coincide with that of the theoretical model, a layer calculating the local slip according to the boundary definitions of the theory is implemented (see also the next section).

Figures 3.1 and 3.2 depict the boundaries assumed by the theoretical models. Assessing the periodicity of the problems, it is clear that the application of periodic boundary conditions (see section 2.5.1) in the two directions orthogonal to the pattern and parallel to the boundary can in these cases drastically reduce the simulation domain. Since these directions coincide with the x - and z - axes only in the case of inflow parallel to the pattern, $\Theta = 0$, it was furthermore important to be able to rotate the flow rather than the surface, something enabled by the on-site velocity boundary conditions as well (section 2.5.2).

3.3.2 Scales and parameterisation

Due to the Fourier analysis outlined in section 3.2.2, all heights H and slip-lengths b for the theoretical solutions of striped surfaces are non-dimensionalised for a stripe length of $L = 2\pi$. The resolution of the simulated system is then given by the lattice constant

$$\Delta x = \frac{H}{2\pi\mathcal{N}}, \quad (3.40)$$

where \mathcal{N} is the number of discretisation points used to resolve the height of the channel. Table 3.3 shows the resulting lattice measures (in lattice units (l.u.) for

the respective height to periodicity ratios H/L as well as the relative error $\epsilon(H/L)$ introduced by the discretisation.

Non-dim. Height H/L	Domain Height H [l.u.]	Domain Width L [l.u.]	Relative Error $\epsilon(H/L)$
100	1024	64	$+5.3 \cdot 10^{-3}$
10	102	64	$-4.0 \cdot 10^{-4}$
1	32	200	$+1.4 \cdot 10^{-3}$
0.1	70	4400	$+5.3 \cdot 10^{-3}$
0.01	102	64000	$+1.4 \cdot 10^{-3}$

Table 3.3: *Domain size parameters according to Eq. 3.40, employed for the simulation of striped surfaces presented in section 3.4. The relative error introduced by the discretisation can be kept in the order of 10^{-3} .*

In case of the solutions obtained by the cosine slip variation, no re-scaling is necessary, as only the thick channel limit is considered. Thus, all simulations are carried out with a height to periodicity ratio of $H/L = 10$ resolved by a domain of $960 \times 96 \times 1$ lattice sites size.

To model the slip stripe pattern, two simulation parameters are introduced, corresponding to the partial slip section length δ and periodicity length L , respectively (compare fig. 3.1). In contrast to the theoretical model, the origin is set to the onset of the partial slip portion of the surface rather than its centre, resulting in an offset of $-\delta/2$.

In case of the cosine pattern the parameters b_0 for the mean slip value and b_1 for the amplitude are introduced with appropriate calculations for the local slip to be set in the boundary condition, distributing a complete period of 2π over the given domain width (in y -direction).

The slip length in the on-site velocity boundary condition introduced in section 2.5.2 is entering the simulation as coefficient of the boundary condition

$$\zeta = \frac{3b}{\tau(1 + 3b/\tau)}. \quad (3.41)$$

To drive the flow, a pressure gradient is applied by means of a homogeneous acceleration, a , throughout the whole fluid domain (viz. sec. 2.3.2). The acceleration

is implemented to be applied along the Cartesian directions, thus flow rotation is imposed by parameterisation as

$$\mathbf{a} = (a \sin \Theta, 0, a \cos \Theta). \quad (3.42)$$

In all thin channel simulations the value of acceleration is chosen to be $a = 10^{-6}$ l.u. and $a = 10^{-7}$ l.u. in thick channel simulations, respectively. Furthermore, the LBGK relaxation time is set to $\tau = 1$ without loss of generality, throughout all presented simulations.

3.3.3 Spatial resolution and convergence in time

The number of time steps required to reach a steady state depends on the channel height, the velocity of the flow as determined by the driving acceleration as well as the fraction of slip and no slip area at the surface. For the simulations conducted in the thin channel limit a steady state velocity field exactly fitting the theoretical prediction develops after one to four million time steps. In the thick channel limit, however, the number of time steps required can be an order of magnitude larger, limiting the maximum feasible system height. Moreover, the transition between slip and no slip stripes induces a distortion of the flow field with a range of $\simeq 3\Delta x$. In order to keep the induced error below an acceptable limit, a minimum resolution of the channel length of $64\Delta x$ is maintained. Additionally, the maximum flow velocity is limited due to the low Mach number assumption of our lattice Boltzmann implementation. In effect, the acceleration modelling the pressure gradient has to be reduced increasing the time required for convergence. For example, a simulation domain of $1 \times 1024 \times 64\Delta x^3$ as used to model the thick channel limit at $H \simeq 100$ requires 12.5 million time steps to equilibrate.

3.3.4 Measurement of effective slip

To validate the concept of a tensorial slip by simulations of a flow past tilted stripes, it is feasible to not rotate the surface pattern with respect to the lattice, but rather change the direction of the acceleration in the yz -plane. This avoids discretisation errors due to the underlying regular lattice occurring in case of a rotated surface pattern. The downstream slip is extracted by projecting the slip measured on the main axes onto the pressure gradient direction.

Measurements of b_{eff} by permeability estimates and velocity profiles, respectively have been compared. The permeability is calculated from measurements of the flow rate, according to Eq. (2.23). This allows to determine the effective slip by Eq. (3.9).

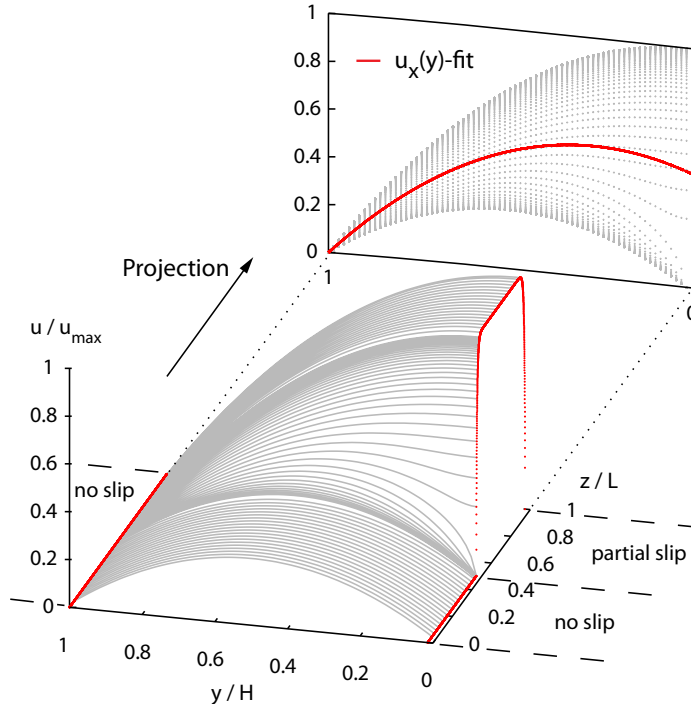


Figure 3.3: *Illustration of the measurement of effective slip eigenvalues from lattice Boltzmann simulations. The velocity information of the whole domain is projected onto a single plane. To this cloud of data, Eq. (3.43) is fitted, effectively averaging the flow field over the whole channel.*

Alternatively, the profiles of the velocity in flow direction are averaged over the whole system by projecting the velocity information of the whole domain onto a single plane. Then, the effective slip length b_{eff} is found by a Levenberg-Marquardt fit of the adjusted Hagen-Poiseuille equation

$$u_x(y) = \frac{aH^2}{2\eta} \left(\frac{(y-H)^2}{H^2} - \frac{(y-H) + b_{\text{eff}}}{(H + b_{\text{eff}})} \right), \quad (3.43)$$

with the known acceleration a and channel height H (see Fig. 3.3 for an illustration).

Due to the overall better data quality at reasonable resolutions, in the remainder of this thesis slip measurements by comparison of the flow profiles are presented (see also next section).

3.3.5 Discussion of error

The error of the effective slip measurements is determined by two factors, namely the resolution of the channel height and the absolute slip length of the partially slipping stripes. For poorly resolved channels with $10 < \mathcal{N} < 30$ and small slip lengths the permeability measurements still produce accurate results, whereas a fit of the velocity profiles does not converge or produces strongly deviating results. This is due to the mode of measurement in both cases, where the permeability approach is primarily limited by the accuracy with which the mean velocity in the channel is determined. The fit of slip flow is however primarily parameterised by the slip length, i.e. slip-velocity at the stripe boundary. Therefore, if $b \gg H$, the quality of the data obtained by permeability measurement declines as the measurement of the mean velocity in the channel is not sensitive enough to capture subtle changes in the boundary layer velocity. For an increase in resolution ($30 < \mathcal{N} \leq 100$) both approaches allow measurements with an error well below one percent for intermediate slip lengths of up to two orders of magnitude larger than the channel height. However, if b is increased further, due to the discretisation error in the effective slip determined by the permeability measurement again increases significantly, rendering this method inefficient since in order to reach the same precision of measurement, a higher resolution would be required. For example, to keep the error in the determination of a prescribed slip in the order of $10^5 \Delta x$ below 5% the permeability method requires the channel height to be resolved by 200 lattice sites, while for the measurement by fitting the velocity profiles 100 sites suffice.

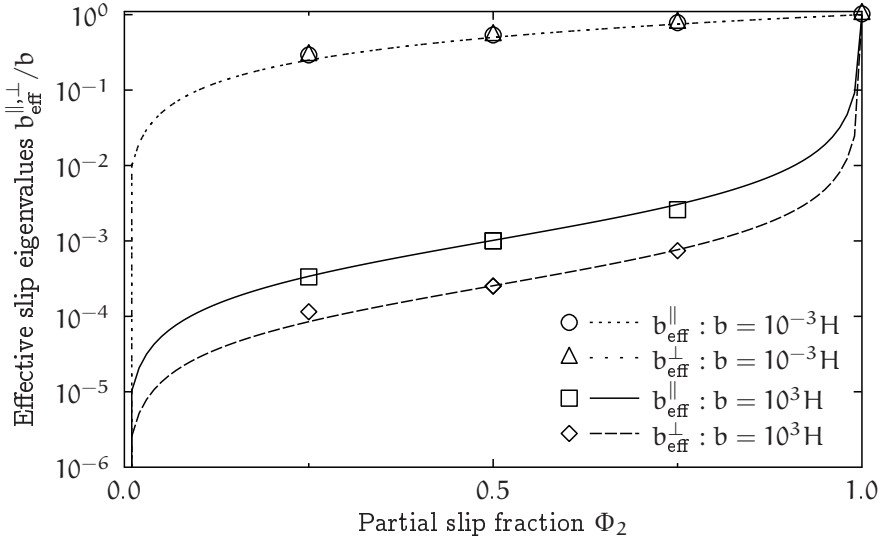


Figure 3.4: *Eigenvalues of the effective slip length tensors simulated in the limit of a thin channel (symbols). The lines represent results of theoretical calculations by Eqs. (3.12) and (3.15). The data show that at small b the eigenvalues of b_{eff} decrease as compared to a large local slip at the gas sector, and that the slip-length tensor becomes isotropic resulting in $b_{\text{eff}}^{\perp,||}$ to become hardly distinguishable in the $b = 10^{-3}H$ case.*

3.4 Slip flow in anisotropically patterned channels

3.4.1 Stripe pattern in the thin channel limit

In order to reach the thin channel limit, a dimensionless height of $H = 0.01$ is chosen. The slip lengths are set to $b = 10^{-3}H$ ($0.1\Delta x$) and $b = 10^3H$ ($102000\Delta x$), differing each three orders of magnitude from the channel height and reaching the limits of small - (cf. Eqs. (3.14) and (3.17)) as well as large slip (Eqs. (3.13) and (3.16)). A minimum channel height of $H = 100\Delta x$ is required to measure slip-lengths of $b = 10^3H$ corresponding to $10^5\Delta x$. For each of the two slip lengths, longitudinal and transverse flow was simulated for different fractions of surface gas phase, ranging from no-slip ($\phi_2 = 0$) to homogeneous partial slip ($\phi_2 = 1$).

Fig. 3.4 shows the exact eigenvalues of the effective slip tensor in the thin channel limit, Eqs. (3.12), (3.15), for both slip lengths b . The fit of the simulation data and

the analytical limits is excellent for all separations. In case of small local slip in a thin channel, the effective slip remains isotropic despite of the inhomogeneity of the boundary. For large local slip, truly tensorial effective slip is observed as well as highly anisotropic flow over the surface. These simulations demonstrate that finite size effects and resolution effects are well controlled, and the size of the system is sufficient to avoid artefacts. Another important point to note is that in the theoretical analysis, all equations were derived ignoring stripe edge effects. An excellent agreement between theoretical and simulation results indicates that the edge effects do not influence the simulation results significantly. The data show however, that already very small fractions of no slip surface have a profound impact on the magnitude of the resulting effective slip, where the relative effect is less pronounced for lower slip.

To check the validity of the tensorial slip approach, it is necessary to investigate the effects of rotating the texture relative to the x -axis, which here is synonymous with the direction of the applied pressure gradient. As mentioned above, in the simulation in fact the pressure gradient direction is varied rather than the boundary pattern in order to reduce discretisation effects. Figs. 3.5, 3.6 show a set of effective downstream slip lengths simulated with several Θ , but fixed $H = 0.1$ and $\phi_2 = 0.5$, which results in a maximum transverse flow in a thin channel situation [242].

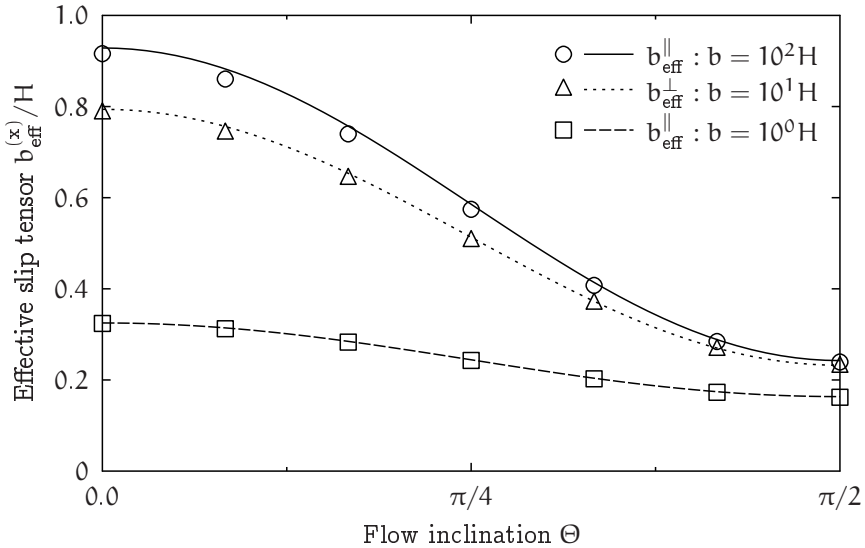


Figure 3.5: *Downstream effective slip lengths of the thin channel simulated at $\phi_2 = 0.5$ for stripes inclined at different angle Θ (symbols). Lines are theoretically predicted downstream slip lengths calculated by using Eq. (3.1) [or Eq. (3.11)] with eigenvalues of b_{eff} determined from numerical solutions of (3.28),(3.29) and (3.30),(3.31)*

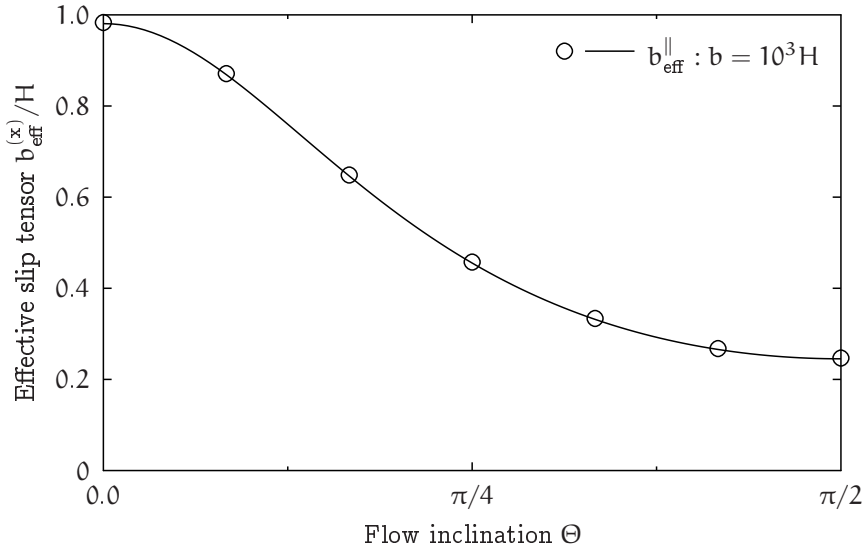


Figure 3.6: *Downstream effective slip lengths of the thin channel simulated at $\phi_2 = 0.5$ in the limiting case the value of $b_{\text{eff}}^{(x)}$, for stripes inclined at different angle Θ (symbols). Lines are theoretically predicted downstream slip lengths calculated with Eq. (3.18).*

Thin channels with varied relative slip lengths b/H from 1 to 1000 are considered. Fig. 3.5 shows simulation data obtained using a channel of height $H = 0.1$. Further, theoretical curves calculated with Eq. 3.1 are presented. Here, eigenvalues of the slip-length tensor are obtained by numerical solution of a dual series [98]. The simulation data are in very good agreement with the numerical solutions of the dual series suggesting the validity of the concept of a tensorial slip in a thin channel situation.

Note that the simulation results of Fig. 3.5 cannot be compared with the analytical expression, Eq. (3.18), because Fig. 3.5 is based on a relatively moderate value of local slip at the gas sectors, whereas Eq. (3.18) requires very large b . To validate predictions of this analytical formula, the channel height was decreased down to $H = 0.01$. Simulation results are presented in Fig. 3.6, confirming the surprising accuracy of a simple analytical expression, Eq. (3.18). In this important limit of validity of Eq. (3.18), $b_{\text{eff}}^{(x)}/H$ is quite large, although $b_{\text{eff}}^{(x)}$ itself is small. This may have implications for a reduction of a hydrodynamic drag force [96, 241].

Also passive mixing might be an interesting application, since the anisotropy of flow is very large, which is optimal for a transverse flow generation [242]. This simple asymptotic result could be intensively used to simplify the theoretical analysis of

these important phenomena. From the numerical model perspective, the agreement suggests this simulation setup to be applicable to model more complex systems, not directly accessible to theory as well.

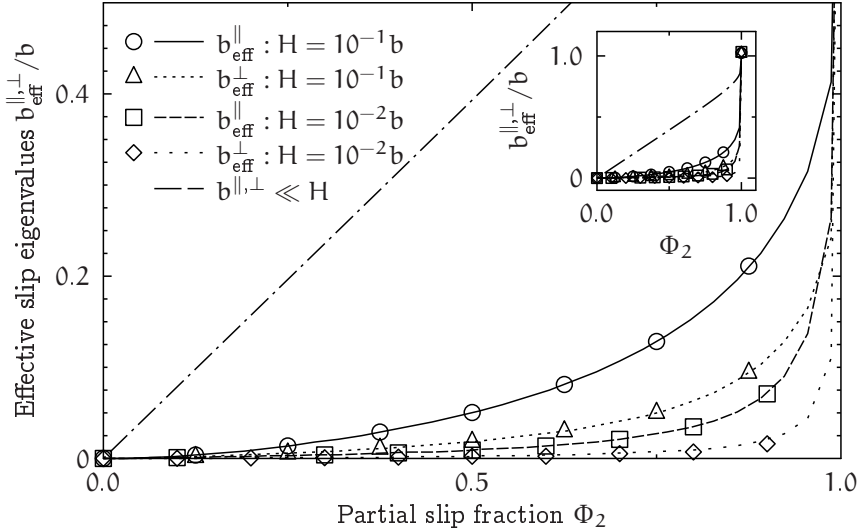


Figure 3.7: Simulation results of eigenvalues of b_{eff} as a function of fraction of gas sectors, ϕ_2 , in the limit of thick channel (symbols). Lines represent corresponding theoretical values obtained by a numerical solution of (3.28), (3.29) and (3.30), (3.31). Dash-dotted is the theoretical weakly slipping stripe solution, Eqs. (3.20), (3.23) as reported by Asmolov et al. in [245]. The inset shows the full curve including the full slip surface data point.

3.4.2 Stripe pattern in the thick channel limit

To evaluate the validity of the formalism in arbitrary channel geometries, an investigation of the thick channel limit is necessary. In addition, results found in this investigation are relevant to models of free surfaces as well. Fig. 3.7 shows the eigenvalues of the effective slip length tensor as a function of ϕ_2 for a thick gap. For these simulations the acceleration has been reduced down $a = 10^{-7} \Delta x / \Delta t^2$ to obey the low Mach number limit (see section 2.4). The time to reach a stable state increased then to $15 \cdot 10^6 \Delta t$. Simulation results are presented for two different slip lengths of $b = 1.0$ and $b = 10.0$ in a system of $H = 0.1$, where L is now resolved by 4400 lattice sites. The theoretical solutions represented by the lines were obtained by the dual series approach. The plot further contains the theoretical weakly slipping stripe solution,

Eqs. (3.20),(3.23) as reported by Asmolov et al. in [245] as limiting curve. The inset shows the full curve including the full slip surface data point. Excellent agreement for all fractions of slipping area is found, indicating that the semi-analytical theory is very accurate. The data presented in Fig. 3.7 show larger effective slip lengths for a lower slip to height ratio, i.e. a thicker channel. This illustrates well the earlier suggestion that effective boundary conditions for this channel geometry are controlled by the smallest length scale of the problem [96].

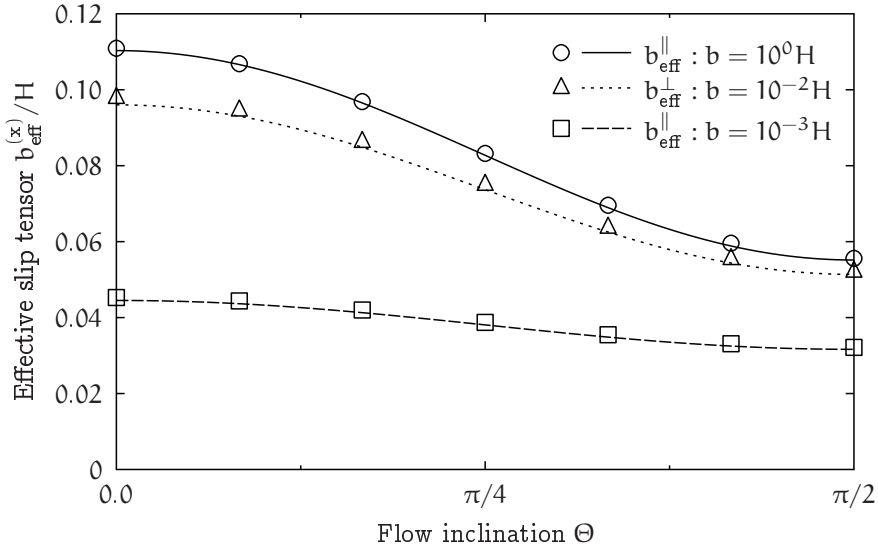


Figure 3.8: *Effective downstream slip lengths for tilted stripes (in the thick channel limit) simulated at $\phi_2 = 0.5$ (symbols). All the lines are predicted theoretically downstream slip lengths. Calculated by using Eq. (3.1) [or Eq. (3.11)] with eigenvalues of \mathbf{b}_{eff} determined from numerical solutions of (3.28), (3.29) and (3.30), (3.31).*

In the second set as shown in Figs. 3.8, 3.9 a thick channel (of height $H = 100$) is simulated. Fig. 3.8 depicts simulation results for several b/H varying from 10^{-3} to 1 (symbols). Similarly to previous examples, very good agreement between simulation results and predictions of tensorial Eq. (3.1) with eigenvalues computed by semi-analytical theory is found. Already for the case $b = H = 100$ the simulations reach the limit of large slip in the thick channel, so that the comparison with analytical solutions is possible. To examine this more closely, the simulation results obtained in this limit are reproduced in Fig. 3.9. Also included there are the theoretical results calculated with asymptotic formulae, Eqs.(3.21) and (3.24), which perfectly fit the simulation data.

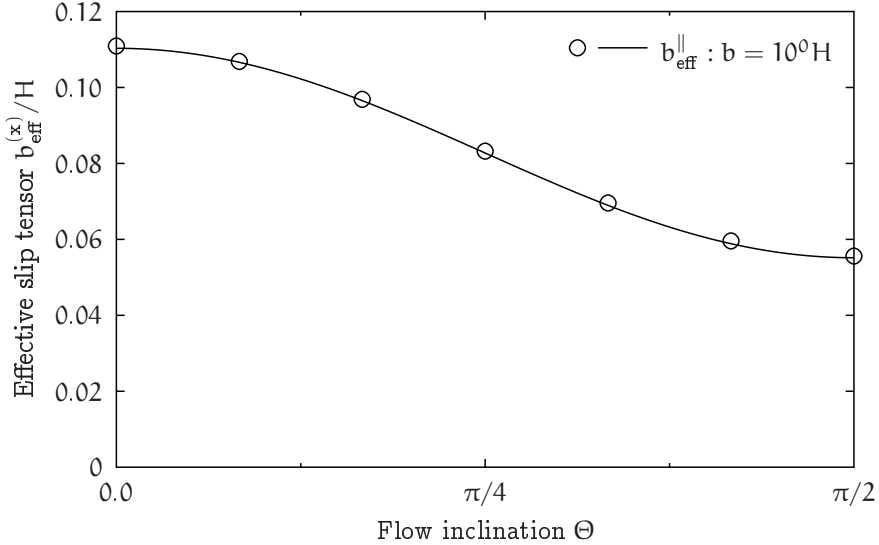


Figure 3.9: *Effective downstream slip lengths for tilted stripes (in the thick channel limit) simulated at $\phi_2 = 0.5$ (symbols). Lines are theoretically predicted downstream slip lengths calculated with Eq. (3.25) with eigenvalues evaluated with Eqs. (3.21) and (3.24).*

3.4.3 Stripe pattern in channels of arbitrary height

Lastly, the downstream slip length as a function of the channel thickness with the focus on the intermediate gap situation is investigated. Fig. 3.10 illustrates typical simulation results. The example given corresponds to parameters of $b/L = 5.0$ and $\phi_2 = 0.75$. It demonstrates that the effective slip lengths increase with H and saturate for a thick gap. This fully confirms the statement that an effective boundary condition is not a characteristic of the liquid-solid interface alone, but depends on the flow configuration and interplay between the typical length scales of the problem. Again, the simulation and theoretical data are in excellent agreement for longitudinal, transverse, and tilted stripes. Thus, Fig. 3.10 unambiguously shows that the tensorial slip boundary condition, originally justified for a thick channel, can be generalised to arbitrary channel thickness.

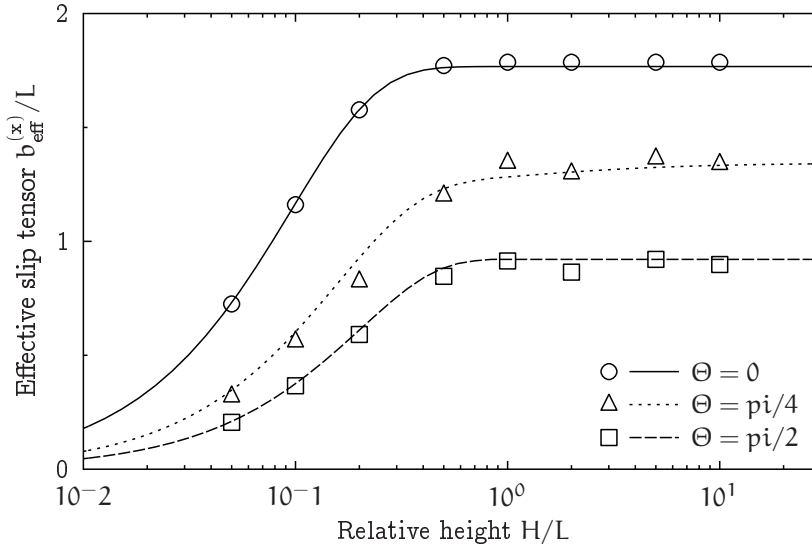


Figure 3.10: *Effective downstream slip lengths at different channel thickness ($\phi_2 = 0.75$, $b/L = 5.0$). Symbols illustrate the simulation data, and curves show theoretical predictions. Deviations stem from varying discretisation artefacts for the relative slip lengths and channel heights and stripe periodicity.*

3.4.4 Cosine pattern in the thick channel limit

In case of stripes the perturbation of piece-wise constant local slip has a step-like jump on the heterogeneity boundary, which leads to a singularity both in pressure and velocity gradient by introducing an additional mechanism for a dissipation [254]. It is natural to assume that an anisotropic one-dimensional texture with a continuous local slip could potentially lead to a larger effective tensorial slip. Therefore, in this section, work on the effective slip of flat surfaces with cosine variation in the local slip length, which corresponds to modulated hydrophobic grooved surfaces with a trapped gas layer (the Cassie state) as shown in Fig. 3.2 is presented.

For variation of the amplitude of cosine perturbations of the slip length, b_1 , at fixed $b_0 = 1$, Fig. 3.11 compares simulation data for $b_{\text{eff}}^{\parallel}$ and b_{eff}^{\perp} as a function of b_1/b_0 . The results show that the largest possible value of b_{eff}/b_0 is obtained when $b_1 = 0$, i.e. for a smooth hydrophobic surface with $b(y) = b_0$. In this situation the effective slip is (obviously) isotropic and equal to the area-averaged slip b_0 . When increasing the amplitude b_1 , a small anisotropy of the flow appears, and the eigenvalues of the slip-length tensor decrease. Therefore, in the presence of a cosine variation in slip length, the effective slip always becomes smaller than average. This conclusion is

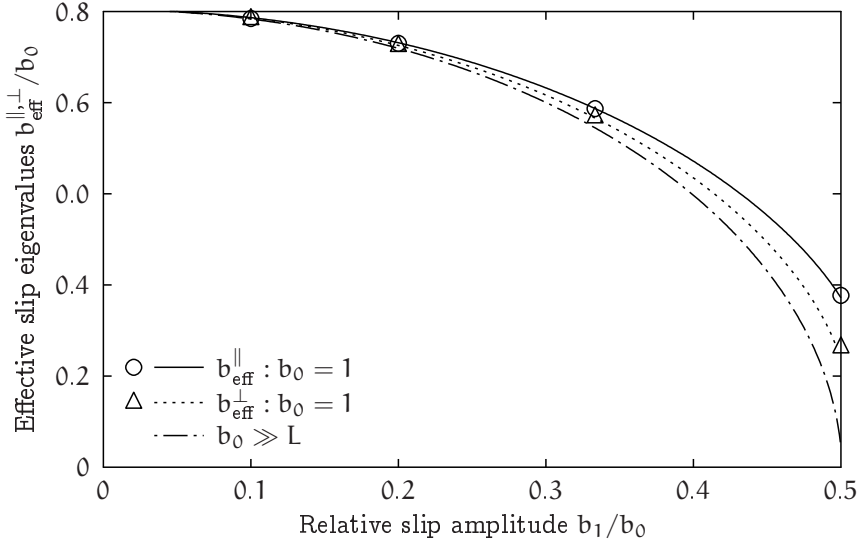


Figure 3.11: Eigenvalues of the effective slip-length tensor as a function of b_1 simulated at fixed $b_0 = 1$ (symbols). The longitudinal effective slip length, $b_{\text{eff}}^{\parallel}$, is shown by circles, and the transverse effective slip b_{eff}^{\perp} is presented by diamonds. Solid and dashed curves denote the corresponding theoretical values obtained by numerical Fourier-series solutions. The asymptotic (isotropic) solution, Eq. (3.38), expected in the limit $b_0 \gg L$ is shown by the dash-dotted line.

consistent with earlier observations made for different textures [97, 259].

To obtain theoretical values, a linear system is solved numerically [232]. Excellent agreement to simulations is found for all b_1/b_0 , indicating that the asymptotic theory is very accurate.

In particular, this confirms the factor 2 relation (3.37) between the longitudinal and transverse slip lengths. Also included in Fig. 3.11 is the asymptotic formula (3.38) obtained in the limit of large b_0 .

Fig. 3.12 (a) shows the simulation data for effective slip lengths as a function of an average slip, b_0/L , for a texture with a no-slip point ($b_1/b_0 = 1/2$). Also included are theoretical (Fourier series) curves. The agreement is quite good for b_0/L up to 10, but for larger average slip there is some discrepancy. The simulation results for $b_{\text{eff}}^{\parallel}$ and b_{eff}^{\perp} give smaller values than predicted by the theory. A possible explanation

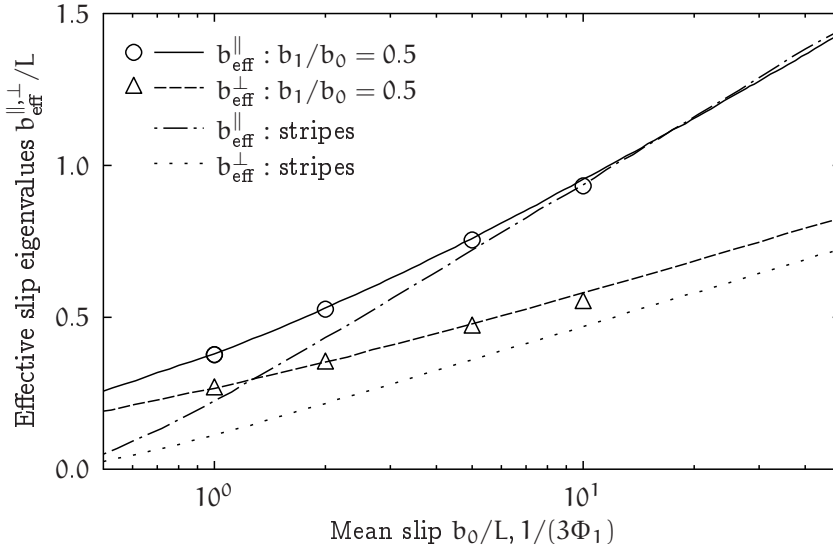


Figure 3.12: *Effective slip lengths computed for $b_1/b_0 = 0.5$, which correspond to a texture with no-slip lines, vs. average slip. The notations are the same as in Fig. 3.11. Dash-dotted and dotted lines show the effective lengths for longitudinal and transverse stripes as a function of $1/(3\phi)$ calculated with Eqs. (3.21),(3.24).*

for this discrepancy is that the major contribution to the shear stress at large b_0/L and $b_1/b_0 = 1/2$ comes from a very small region near the no-slip point (as discussed below). The discretisation error of the LB simulation becomes maximal in this region, and is particularly pronounced for the velocity gradients of systems with large effective slip. While deviations around the no slip extremal value are observed, the curves converge fast when stepping away from it and the excellent agreement of the measured effective slip suggests that the influence of discretisation errors on the mean flow is negligible at the resolution used.

Since the effective slip lengths for a texture decorated with perfect-slip stripes, Eqs. (3.21), (3.24), also show a logarithmic growth (with the no-slip area fraction $\phi_1 = 1 - \phi_2$), in order to compare these two one-dimensional anisotropic textures the theoretical curve for stripes is included in Fig. 3.12. It can be seen that in the limit of large average slip the asymptotic curves for longitudinal effective slip for stripes and a cosine texture nearly coincide. This means that both textures generate the same forward flow in the longitudinal direction. Simple estimates suggest $b_{\text{eff}}^{\parallel}(b_0) \simeq b_{\text{idéal}}^{\parallel}[1/(3b_0)]$. Perhaps the most interesting and important aspect of

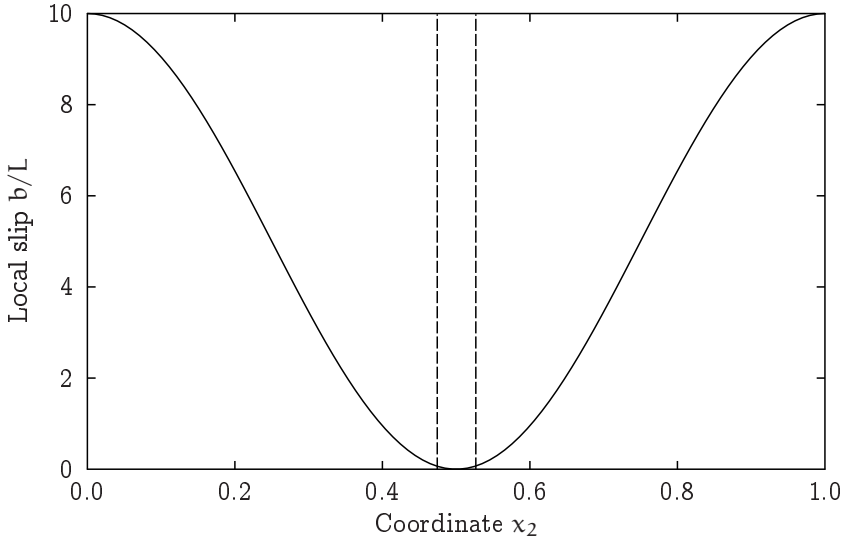


Figure 3.13: *The cosine profile of the local slip length with $b_0/L = 5$, $b_1/b_0 = 0.5$ (solid curve) and the stripe profile with $\phi = 0.06$ (dashed line) with the same longitudinal effective slip lengths.*

this observation is that, from the point of view of the longitudinal effective slip, the ‘wide’ cosine texture with $b_0 = 5$ is equivalent to patterns of stripes with the extremely low fraction of no-slip regions, $\phi = 0.06$ (see Fig. 3.13). These results may guide the design of superhydrophobic surfaces for large forward flows in microfluidic devices. Note, however, that in the situation when longitudinal slip for both textures are similar, the cosine texture shows a larger effective slip in the slowest (transverse) direction as seen in Fig. 3.12. This means that $b_{\text{eff}}^{\parallel}/b_{\text{eff}}^{\perp} < b_{\text{ideal}}^{\parallel}/b_{\text{ideal}}^{\perp} = 2$, so that textures with the cosine variation in the local slip length generate a less anisotropic flow as compared to a perfect stripe geometry.

In order to understand the pronounced effect on no-slip portions of the surface on the resulting effective slip, it is instructive to investigate the flow profile.

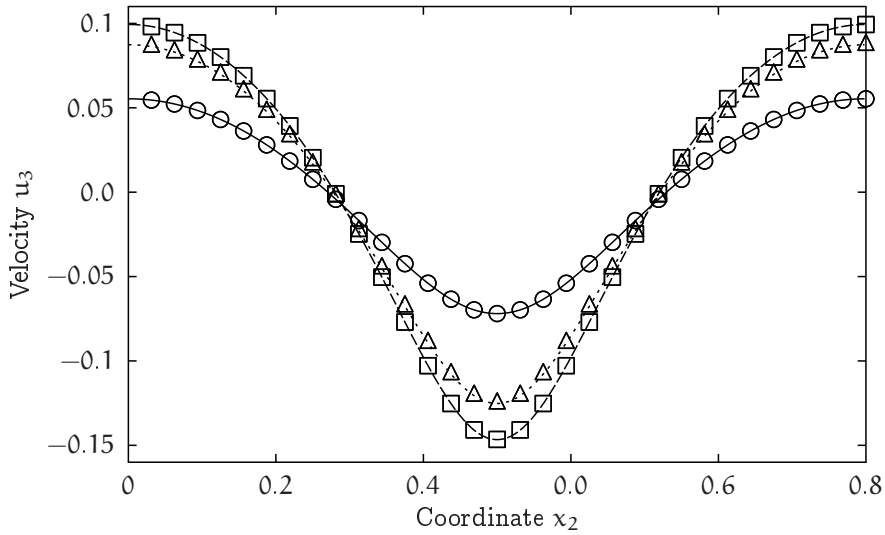


Figure 3.14: The velocities right along the wall for the textures with $b_1/b_0 = 1/3$, $b_0/L = 0.2$ (solid curve, diamonds), $b_0/L = 1$ (dashed curve, circles), $b_0/L = 5$ (dash-dotted line, crosses). Dotted curves show predictions of asymptotic formulae, Eqs. (3.36) and (3.35).

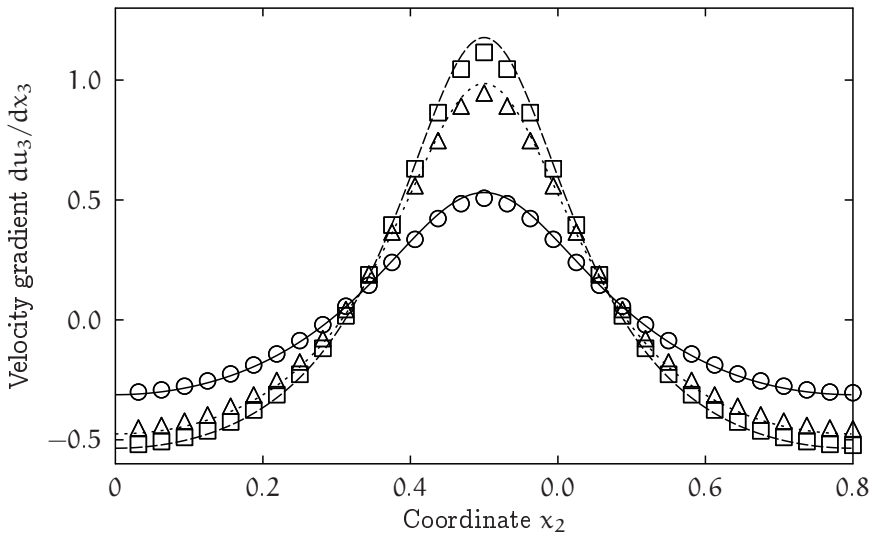


Figure 3.15: The normal velocity gradients along the wall for the textures with $b_1/b_0 = 1/3$, $b_0/L = 0.2$ (solid curve, diamonds), $b_0/L = 1$ (dashed curve, circles), $b_0/L = 5$ (dash-dotted line, crosses). Dotted curves show predictions of asymptotic formulae, Eqs. (3.36) and (3.35).

The flow direction is associated with hydrodynamic pressures in the film, which is related to the heterogeneous slippage at the wall. Fig. 3.14 shows the profiles of the velocity and Fig. 3.15 of the normal velocity gradient along the wall for different b_0 and $b_1/b_0 > 1/2$. The velocity dependence $u(x, y, 0)$ is smooth, and $\frac{\partial u}{\partial z}(x, y, 0)$ is finite for any b_0 and b_1 , unlike the striped textures with piece-wise-constant b [254]. Asymptotic predictions (3.36) and (3.35) are in a good agreement with numerical results and simulation data.

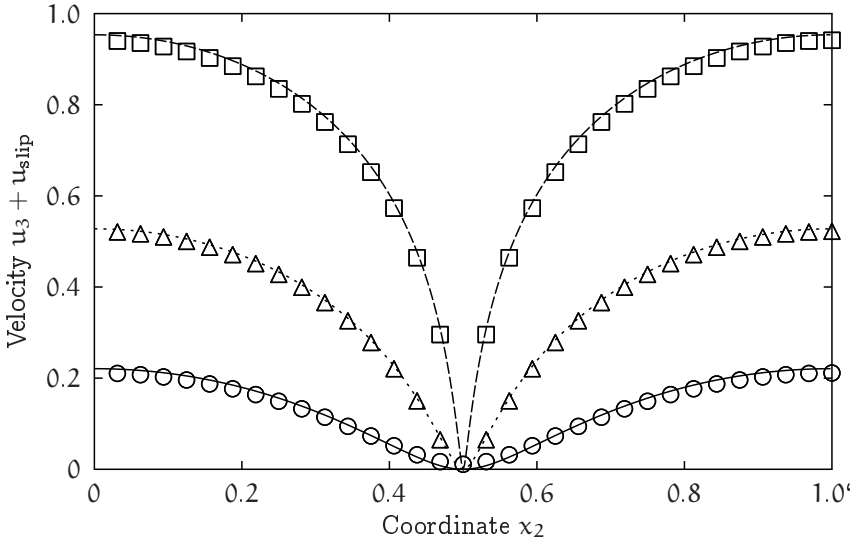


Figure 3.16: The velocities along the wall for the no-slip textures $b_1/b_0 = 1/2$, $b_0/L = 0.2$ (solid curve, diamonds), $b_0/L = 1$ (dashed curve, circles), $b_0/L = 5$ (dash-dotted line, crosses). Dotted curves show predictions of asymptotic formulae, Eqs. (3.36) and (3.35).

Similar theoretical and simulation results, obtained for a texture with no-slip point, $b_1/b_0 = 1/2$, are shown in Figs. 3.16 and 3.17. In this situation it is found that $\partial u/\partial z(1/2) = 2\pi b_0$ for all b_0 .

It should be emphasised, that a very small region near the no-slip point gives a main contribution to the shear stress at large b_0/L . For the major portion of the texture far from this region $\partial u/\partial z \simeq -1$, so that the total shear stress is zero, and this part of the texture is shear-free. Since the maximum values of the normal velocity gradients grow like b_0/L one can expect that a length scale of this small region is $L^2/b_0 \ll L$, or, equivalently, the curvature radius, $r = (d^2b/dy^2)^{-1} = L^2/(4\pi^2 b_0)$, at the no-slip point.

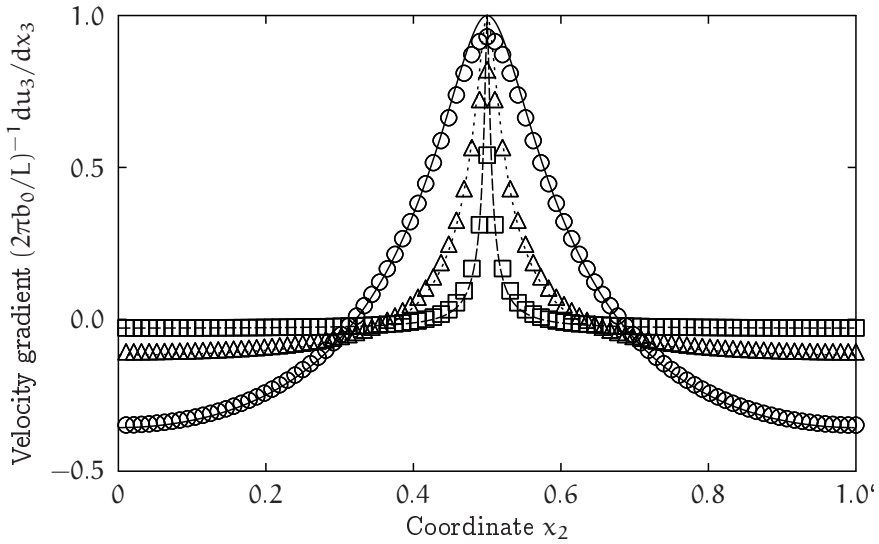


Figure 3.17: *The normal velocity gradients along the wall for the no-slip textures $b_1/b_0 = 1/2$, $b_0/L = 0.2$ (solid curve, diamonds), $b_0/L = 1$ (dashed curve, circles), $b_0/L = 5$ (dash-dotted line, crosses). Dotted curves show predictions of asymptotic formulae, Eqs. (3.36) and (3.35).*

In spite of deviations from theory caused by insufficient resolution of the simulation around the no-slip minimum, the simulation model is still able to capture the flow velocity in the remainder of the channel. This suggests that an extension of the slip patterning formalism to account for complex patterns derived from measurements might be feasible. In this spirit, in the next section a further reaching application of the model is discussed briefly.

3.5 Drag force on a sphere approaching a slip striped plane

The boundary condition extension and experiences with the parameterisation have been put to use in the context of an example application. The calculation of forces exerted on a spherical probe approaching a surface in a fluid is of interest in certain AFM setups. Simulations of this type for approaches to smooth wetting and rough surfaces have been conducted by Kunert [61]. The problem is sketched in Fig. 3.18. For plain surfaces, the problem has been solved theoretically by Brenner and Maude.

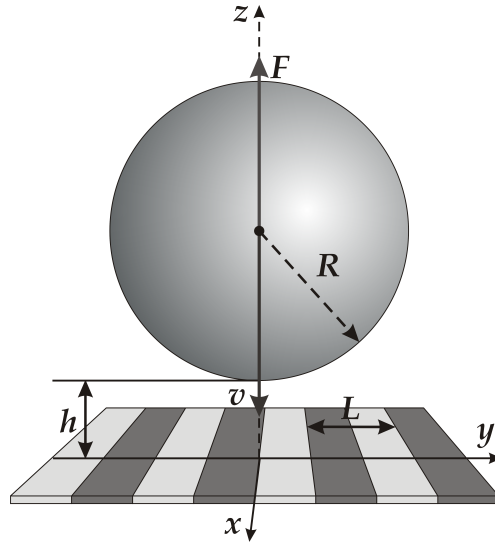


Figure 3.18: *Sketch of the simulated system. A sphere is approached towards a striped slip wall. Illustration as published in [233], courtesy of A.L. Dubov.*

Comparison of such such simulations with experiments furthermore offer an opportunity to gauge the model for boundary effects neglected by the theoretical approach. If effects of e.g. interface deformation can be factored into the boundary description in the numerical model, the accuracy and efficiency of the simulation of heterogeneous complex boundaries can be improved.

The boundary condition setup was used to model a (superhydrophobic) surface with striped slip pattern, approached by a sphere at a constant speed the force onto which was measured. The problem requires to simulate the system in full three dimensions. Figure 3.19 shows the velocity field in a plane above the surface, illustrating that important features of flow and hydrodynamic interactions are not captured by 2d simplifications of the model.

Another requirement introduced by the theoretical model is given by the assumption of the sphere radius being large as compared to the pattern periodicity. Moreover, employing periodic boundary conditions in the plane orthogonal to the sphere movement, the sphere has to keep several radii distance from the simulation domain boundary in order to minimise periodicity artefacts. Figure 3.19 shows that in y -direction parallel to the pattern this requirement is already hardly maintained as the vortex features at $x/L = -0.75, 0.25$ are clearly reaching to the y boundaries. Given the outlined limitations, in contrast to the high resolved pattern analysis detailed above, in this case the stripe resolution was limited to a periodicity length of $L = 16$ with a sphere radius of $R = 32$ and and domain width of 256 lattice sites, where the system height

in the direction of approach was chosen to comprise 512 lattice sites.

As it turns out, the grave changes in resolution of the surface and critical periodicity effects are however not the main source of error. In order to create a neutral interacting boundary, the upper edge of the simulation domain was bounded by a no-slip surface. Given that in the lubrication limit this boundary would be 16 sphere radii away, a minimal disturbance by this change in the model is originally assumed. Detailed analysis of the data shows that the assumption of minimal perturbation by the upper no-slip boundary is invalid. A quantitative correction could be determined as a function of radius and system height, indicating that confinement effects are prominent.

Despite the issues encountered with the modelling restrictions in this case, the model can serve as an important point of comparison of numerical results and experiment, ultimately allowing the assess the feasibility of effective slip models for systems exhibiting surface deformation and other quasi-static phenomena influencing friction and slippage behaviour.

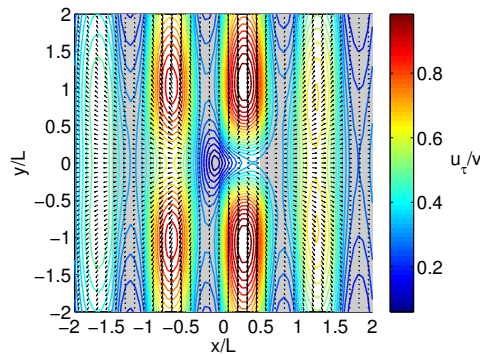


Figure 3.19: *Vector field of horizontal velocity for $z = L/8$, $h = 3L/4$, grey and white regions correspond to no-slip and slip stripes, respectively. Courtesy of A.L. Dubov.*

3.6 Conclusion and outlook

The development of theoretical and numerical models for the evaluation of complex functional surfaces like superhydrophobic surfaces in the context of MEMS can further advance the understanding of the hydrodynamic boundary as well as help to design such systems. Interesting parameters in this context are the flow rate as well as lateral velocities for flow control and passive mixing. They can be related to the tensorial

permeability as well as tensorial slip properties.

In this section a theoretical framework for the calculation of the effective slip tensor in smooth anisotropic patterned channels of arbitrary height has been evaluated by means of the LBM. At the same time the excellent agreement of the LBM and the theory allows confidence in the capability of LBM to model patterned surfaces exhibiting variation in local slip lengths in more complex cases beyond the theory.

Challenges in the original work where results were presented in sections 3.4.1 and 3.4.2 are detailed in section 3.3. Here included is the selection and parameterisation of boundary conditions. Further, the investigation of minimal resolution requirements of the local slip length and simulation steps required to reach fully developed flow have to be considered. The adaptation of suitable measurement techniques is closely related to this and is also of importance in the determination of error estimates to balance against minimal computational effort.

Besides the quantitative agreement found between the models, the consideration of anisotropic slip patterned surfaces allowed to revisit and verify some interesting qualitative observations with regard to such systems. The work presented clearly verifies effective slip in small geometries as a channel rather than a surface effect. Here it is found that the behaviour is governed by the smallest length scale parameterising the problem, between local slip b , pattern measure L and channel height H . Furthermore, a strong impact on even small no-slip portions on the shear-stress in the system and reduction of effective slip has been found. Re-investigation of the anisotropic boundary using cosine varying patterns to avoid possible influences of the slip *step* in striped channels verifies this. Here, rather than the (lack of) smoothness of slip variation, the existence of no-slip portions of the surface is impeding large effective slip.

The agreement with numerical simulations found was overall very satisfying. In the case of the very poorly resolved (single site) *zero-slip* point of the cosine variation simulation, a local deviation was found which was however without strong impact on the global field due to the individual local parameterisation of each lattice site, suggesting that robust parameterisation can to some extent make up for limited local resolution.

A key issue linked to this is the assessment of parameterisation of the numerical as well as theoretical model with respect to experimentally obtained data. To this end, the framework was applied to simulate a model system comparable to AFM measurement setups. While in the first instance problems with the boundary model suggested limited applicability, the formulation of a correction allows optimism towards evaluation measurements addressing the very important aspect of surface deformation in real superhydrophobic surfaces. There highly deformable interfaces exist between fluids and entrapped gas. Results here may be used to gauge the model.

These results allow confidence in the application of the created framework to model complex boundary conditions also for situations not accessible to theoretical models.

Another example for channel flow systems with local varying slip pattern where the evaluation of effective slip is of interest is given by electro-osmotically driven flow where local slip length can be influenced by the means of electro-magnetic fields. Collaborative work with Stefan Frijters [260], who implemented an extension of the LBM to include electrochemical interactions into LB3D, is currently in the state of boundary condition evaluations. Here qualitative agreement with theoretical prediction has been found, but work still is necessary towards scaling analysis and possible invalid boundary interactions in the hydrodynamic and electro-chemical model.

Chapter 4

A ternary multi-component model for flows in porous media

The content of this chapter is based on

H. LIU, Q. KANG, C. R. LEONARDI, B. D. JONES, S. SCHMIESCHEK, A. NARVÁEZ, J. R. WILLIAMS, A. J. VALOCCHI AND J. HARTING.

Multiphase lattice Boltzmann simulations for porous media applications - a review. *In press*, 2014. pre-print available from arXiv:1404.7523 [physics] [50]

S. SCHMIESCHEK, A. NARVÁEZ, J. HARTING.

Multi relaxation time lattice Boltzmann simulations of multiple component fluid flows in porous media.

High Performance Computing in Science and Engineering '12, 39-49, 2013 [261]

S. SCHMIESCHEK, P. V. COVENEY AND J. HARTING.

Evaluation of a MRT lattice Boltzmann model for the simulation of surfactant-containing multiphase flows in porous media

in preparation, 2015.

4.1 Introduction

Multiphase flows are ubiquitous in natural and technological processes. Following popular use, the term multiphase is used here not only to designate systems involving different aggregation states but general inhomogeneous systems including so-called complex fluids. The term complex fluids refers in general to emulsions and suspensions as well as mixtures of gases and liquids [15]. Examples include biological systems and fluids such as blood but also fluid processes in soil and industrial setups [131, 262]. For many systems of interest also complex geometries of porous systems have a significant impact on the flow properties. Porous media range in this context from freeze dried food stuffs over filters and membranes to sand and stone systems with applications like enhanced oil recovery [76] and carbon dioxide capture over soil processes [77], reactor processes [78–81], filtration [82, 83], printing [84] and food processing [85].

In order to successfully model such systems, besides the bulk flow properties of various fluids, their interaction with each other [263, 264] needs to be captured with sufficient accuracy. The same is true for the system geometry, since the surface to volume ratio is very large in porous materials [73–75]. Depending on the properties of interest different simplifications can be introduced. For example influences of turbulence can be neglected in laminar flows. In systems close to thermodynamic equilibrium many systems can be assumed to behave isothermal as well.

In many of the applications mentioned above, besides two or more immiscible fluids like water and oils, components interacting with both of two respective immiscible species are of interest. These solvents and/or surfactants (SURFace ACTive AgeNTS) are dramatically influencing the behaviour of fluid mixtures [86, 265]. Also particles in solution can alter the behaviour of mixtures. This field of ongoing research is however not part of this presentation [266–268]. For example in enhanced oil recovery, surfactants are used in a third step to extract oil after first relying on the reservoir pressure and second water injection generated pressure. Once these processes seize to produce oil up to 60 percent of oil remain in the reservoir [76]. Furthermore, many complex fluid systems do not only contain independently interacting components, but surfactants as well.

This chapter reports on work extending a ternary pseudo-potential lattice Boltzmann implementation to incorporate a multi relaxation time collision scheme. This is done in order to reduce and subsequently remove errors in the simulation introduced the interaction of bounce-back boundary models and LBGK collision schemes. These have been found to introduce non-resolvable errors introduced by dependence of the boundary position on the relaxation parameter [222]. In the context of permeability measurements in porous media the removal of this error is the most prominent

improvement introduced by utilising a MRT collision scheme. In addition, the MRT formalism has been found to increase numerical stability of the method [158–160] as well as allowing consistent introduction of thermal fluctuations [269–271]. The surfactant model in question has been introduced by Chen and Nekovee et al. [272, 273]. It comprises three fluid components, two of which are coupled by repulsive interaction to be partially miscible or immiscible, while the third models surfactant behaviour interacting with both the immiscible components as well as a dipole field representing the effective orientation of amphiphilic particles.

The next section 4.2 provides details on the additions to the method described above as implemented for this work. Following this in section 4.3, results of simulations verifying the correct behaviour of the implementation with respect to different benchmark problems are presented. After measurement of the surface tension by means of the Laplace law in a system of pseudo-2d droplets, a wall boundary is introduced to investigate the contact angle parameterisation. The effect of the surfactant component in both systems is studied. This is followed by a study on the diffusion behaviour for the case of miscible fluids where the influence of surfactant concentration is taken into account as well. Finally the absolute and relative permeability for the flow of the mixture in a square duct is compared against theoretical results. The quantitative analysis of the error introduced by viscosity variation shows that the exponential error exhibited by LBGK simulations of multi-component permeability can be reduced to an error linear in the viscosity. This can be further improved by use of a higher order force coupling mechanism.

The chapter closes with parameter studies of forced imbibition into a pseudo-2d porous medium. Here, the interplay of forcing, wettability and viscosity contrasts as well as surfactant concentration is investigated. These qualitative benchmarks hold up to benchmark results obtained by LBGK simulations performed in similar systems.

4.2 Modelling aspects

In addition to the basic LB algorithm properties and strategies introduced in chapter 2, this section elaborates on two concepts of relevance in the context of the work reported in this chapter, only. While the amphiphile or surfactant model used here is an unmodified version of the approach originally introduced by Chen et al. [273], the *combination* of this model with a multi-relaxation time collision scheme in a form introduced by d’Humières et al [158] is original code integration and evaluation work.

4.2.1 An amphiphilic fluid component

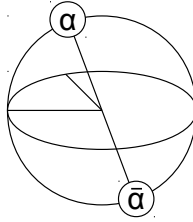


Figure 4.1: *Illustration of the dipole model introducing a directional interaction component between fluids α and $\bar{\alpha}$.*

Characteristic for surfactant molecules is their anisotropic interaction. Typically polar and non-polar components are present in parts of a single molecule resulting in hydrophilic and hydrophobic interactions, respectively. Most surfactant substances are organic compounds where examples include soaps and lipids. The textbook by Rosen and Kunjappu gives a broad overview of the matter [86]. Due to their relevance in industrial as well as natural processes, the configuration and behaviour of surfactants has been subject to a wealth of research [86, 274]. Numerical investigations span the whole range from molecular simulations [121] over finite-element treatments [275, 276] and diffuse interface models [277] to phase-field [278] and lattice Boltzmann investigations [273, 279–281].

Chen et al. [273] suggested an extension of the pseudo-potential interaction to include surfactant molecule effects. True to the idea of representing physical properties in terms of a discrete field of statistical properties, a field of dipole vectors \mathbf{d} , one at each lattice site is added to the model. The equilibrium orientation of these vectors is determined by a free energy approach, minimising the Gibbs measure. Here, two mean fields are considered calculating energy values including information from nearest neighbours with respect to the surfactant orientation relative to other surfactant molecules, which tend to (anti-)align, as well as with respect to a *colour* or component density gradient, respectively. Introducing an additional relaxation parameter τ_d , the dipole orientation is subsequently calculated using a process similar to the BGK approximation

$$\mathbf{d}(\mathbf{x}, t + \Delta t) = \frac{1}{\tau_d} [\mathbf{d}(\mathbf{x}, t) - \mathbf{d}^{\text{eq}}(\mathbf{x}, t)]. \quad (4.1)$$

It is relaxed on a single timescale towards an equilibrium orientation derived from the Boltzmann distribution to be

$$\mathbf{d}^{\text{eq}} = d_0 \left[\coth(\beta h) - \frac{1}{\beta h} \right] \hat{\mathbf{h}}, \quad (4.2)$$

with a free parameter d_0 , representing the strength of the dipole moment, and the inverse temperature β , both chosen to equal 1 here, as well a mean field of magnitude h and unit orientation $\hat{\mathbf{h}}$. The latter can be constructed from contributions of the fluid and dipole-dipole interactions. Furthermore, additional forcing terms parameterised by the coupling parameters $\mathcal{G}_{\alpha\sigma} = -\mathcal{G}_{\sigma\alpha} = \mathcal{G}_{\sigma\sigma} = -0.005$ are introduced.

Following this approach, additional forces can be formulated. These are, for the force imposed by the surfactant on the non-surfactant fluid components

$$\mathbf{F}^{\sigma\alpha}(\mathbf{x}, t) = -2\mathcal{G}_{\alpha\sigma}\psi^\alpha(\mathbf{x}, t) \sum_{k \neq 0} \mathbf{d}(\mathbf{x} + \mathbf{c}_k \Delta t, t) \cdot \boldsymbol{\theta}_k \psi^\sigma(\mathbf{x} + \mathbf{c}_k \Delta t, t), \quad (4.3)$$

wherein $\boldsymbol{\theta}_k = \mathcal{J} - D \frac{\mathbf{c}_k \mathbf{c}_k}{c_k^2}$, with the second rank unit tensor \mathcal{J} and the spatial dimension D is the component of a trace-less second rank tensor accounting for the alignment of surfactant molecule orientations. Similarly, the force imposed by the non-surfactant components on the surfactant component reads

$$\mathbf{F}^{\alpha\sigma}(\mathbf{x}, t) = 2\psi^\sigma(\mathbf{x}, t) \mathbf{d}(\mathbf{x}, t) \sum_{\alpha} \mathcal{G}_{\alpha\sigma} \sum_{k \neq 0} \boldsymbol{\theta}_k \psi^\alpha(\mathbf{x} + \mathbf{c}_k \Delta t, t). \quad (4.4)$$

Finally, the force acting between surfactant components on neighbouring sites is given by

$$\mathbf{F}^{\sigma\sigma}(\mathbf{x}, t) = -\frac{12}{|c_s|^2} \psi^\sigma(\mathbf{x}, t) \mathcal{G}_{\sigma\sigma} \sum_{k \neq 0} \psi^\sigma(\mathbf{x} + \mathbf{c}_k \Delta t, t) \cdot \left(\mathbf{d}(\mathbf{x} + \mathbf{c}_k \Delta t, t) \boldsymbol{\theta}_k \mathbf{d}(\mathbf{x}, t) \mathbf{c}_k + [\mathbf{d}(\mathbf{x} + \mathbf{c}_k \Delta t, t) \mathbf{d}(\mathbf{x}, t) + \mathbf{d}(\mathbf{x}, t) \mathbf{d}(\mathbf{x} + \mathbf{c}_k \Delta t, t)] \mathbf{c}_k \right). \quad (4.5)$$

Details on the derivation can be found in [272, 273]. These forces are added in the algorithm analogous to the pseudo-potential force inducing the phase transition in the binary multi-component system introduced in section 2.4.1.

The equations (4.3)-(4.5) introduce in principle three additional coupling parameters, $\mathcal{G}_{\alpha\sigma}, \mathcal{G}_{\alpha\sigma}$ and $\mathcal{G}_{\sigma\sigma}$, where for reasons of interaction symmetry to ensure global momentum conservation, however $\mathcal{G}_{\alpha\sigma} = -\mathcal{G}_{\sigma\alpha}$ at all times, resulting in a single simulation parameter. From the nature of surfactant interactions follows furthermore the requirement for the surfactant interactions to be attractive, i.e. $\mathcal{G}_{\sigma\sigma} \leq 0$ and $\mathcal{G}_{\sigma\sigma} \leq 0$.

4.2.2 Multi relaxation time collision scheme

In order to remove the dependency of the boundary position on the fluid viscosity, described in section 2.4, and increase stability and accuracy for the application of

the ternary fluid model, a multi relaxation time collision scheme was implemented. Starting from the work of d’Humières et al. [158] the collision operator is redefined introducing an invertible transformation matrix \mathcal{M} , such that it maps the discrete single particle velocity distribution f onto a suitable space of a subset of its moments

$$m_k = \mathcal{M}f_k, \quad f_k = \mathcal{M}^{-1}m_k. \quad (4.6)$$

The collision operator reads then

$$\Omega_{\text{MRT}} = -\mathcal{M}^{-1}S\mathcal{M}\left[|f(\mathbf{x}, t)\rangle - |f^{\text{eq}}(\mathbf{x}, t)\rangle\right], \quad (4.7)$$

where the equilibration rates are governed by the diagonal relaxation matrix S in the space of moments given in table 4.1. This allows for individual adjustment of the relaxation time scales of the respective hydrodynamic properties and non-hydrodynamic properties, or ghost-modes, represented by the moments. The diagonality of S follows from isotropy considerations. Its eigenvalues are not linearly independent but are related by the underlying physics, see e.g. [282]. By executing a Gram-Schmidt orthogonalisation, the transformation matrix

$$\mathcal{M} = \begin{pmatrix} 1 & 1 & 1 & 1 & 1 & 1 & 1 & 1 & 1 & 1 & 1 & 1 & 1 & 1 & 1 & 1 & 1 & 1 & 1 & 1 \\ -11 & -11 & -11 & -11 & -11 & -11 & 8 & 8 & 8 & 8 & 8 & 8 & 8 & 8 & 8 & 8 & 8 & 8 & 8 & -30 \\ -4 & -4 & -4 & -4 & -4 & -4 & 1 & 1 & 1 & 1 & 1 & 1 & 1 & 1 & 1 & 1 & 1 & 1 & 1 & 12 \\ 1 & -1 & 0 & 0 & 0 & 0 & 1 & 1 & 1 & 1 & -1 & -1 & -1 & -1 & 0 & 0 & 0 & 0 & 0 & 0 \\ -4 & 4 & 0 & 0 & 0 & 0 & 1 & 1 & 1 & 1 & -1 & -1 & -1 & -1 & 0 & 0 & 0 & 0 & 0 & 0 \\ 0 & 0 & 1 & -1 & 0 & 0 & 1 & -1 & 0 & 0 & 1 & -1 & 0 & 0 & 1 & 1 & -1 & -1 & 0 & 0 \\ 0 & 0 & -4 & 4 & 0 & 0 & 1 & -1 & 0 & 0 & 1 & -1 & 0 & 0 & 1 & 1 & -1 & -1 & 0 & 0 \\ 0 & 0 & 0 & 0 & 1 & -1 & 0 & 0 & 1 & -1 & 0 & 0 & 1 & -1 & 1 & -1 & 1 & -1 & 0 & 0 \\ 0 & 0 & 0 & 0 & -4 & 4 & 0 & 0 & 1 & -1 & 0 & 0 & 1 & -1 & 1 & -1 & 1 & -1 & 0 & 0 \\ 2 & 2 & -1 & -1 & -1 & -1 & 1 & 1 & 1 & 1 & 1 & 1 & 1 & 1 & -2 & -2 & -2 & -2 & 0 & 0 \\ -4 & -4 & 2 & 2 & 2 & 2 & 1 & 1 & 1 & 1 & 1 & 1 & 1 & 1 & -2 & -2 & -2 & -2 & 0 & 0 \\ 0 & 0 & 1 & 1 & -1 & -1 & 1 & 1 & -1 & -1 & 1 & 1 & -1 & -1 & 0 & 0 & 0 & 0 & 0 & 0 \\ 0 & 0 & -2 & -2 & 2 & 2 & 1 & 1 & -1 & -1 & 1 & 1 & -1 & -1 & 0 & 0 & 0 & 0 & 0 & 0 \\ 0 & 0 & 0 & 0 & 0 & 0 & 1 & -1 & 0 & 0 & -1 & 1 & 0 & 0 & 0 & 0 & 0 & 0 & 0 & 0 \\ 0 & 0 & 0 & 0 & 0 & 0 & 0 & 0 & 0 & 0 & 0 & 0 & 0 & 0 & 1 & -1 & -1 & 1 & 0 & 0 \\ 0 & 0 & 0 & 0 & 0 & 0 & 0 & 0 & 1 & -1 & 0 & 0 & -1 & 1 & 0 & 0 & 0 & 0 & 0 & 0 \\ 0 & 0 & 0 & 0 & 0 & 0 & 1 & 1 & -1 & -1 & -1 & -1 & 1 & 1 & 0 & 0 & 0 & 0 & 0 & 0 \\ 0 & 0 & 0 & 0 & 0 & 0 & -1 & 1 & 0 & 0 & -1 & 1 & 0 & 0 & 1 & 1 & -1 & -1 & 0 & 0 \\ 0 & 0 & 0 & 0 & 0 & 0 & 0 & 0 & 1 & -1 & 0 & 0 & 1 & -1 & -1 & 1 & -1 & 1 & 0 & 0 \end{pmatrix} \quad (4.8)$$

can be obtained. It yields the moments detailed in table 4.1, from the D3Q19 lattice vector set. The transformation has been adapted from [158] with respect to a different lattice indexing in the employed code which may in general result in a shift in

parameters, but reduces here to a mere resorting of elements. The equilibrium moments were recalculated using a third order equilibrium distribution which has been shown to improve the stability of the surfactant force integration in earlier LBGK simulation and was preserved to keep the simulation setup comparable. The equilibrium properties described in the table are functions of the conserved kinetic moments, the density ρ and momentum \mathbf{j} . The employed pseudo-potential method breaks local momentum conservation, but can be shown to still ensure it globally [283]. Due to this, the relaxation parameter for the momentum, described in table 4.1 is kept at 1.0, since the originally conserved property needs to be integrated (its information kept) in order to be conserved. The equilibria of all moments are describable in terms of these. As this model is isothermal (or athermal) the energy of the system and the related moments, the density independent kinetic energy e and its square ϵ are not conserved. Furthermore the mass flux independent energy flux \mathbf{q} and the viscous stress tensor \mathbf{p} as well as a quartic order moment of equivalent symmetry $\boldsymbol{\pi}$ and a third order moment \mathbf{m} are taken into account.

Special attention has to be paid to the parameterisation of this collision approach. Besides the free weight parameters $w_\epsilon, w_{\epsilon j}$ and $w_{\mathbf{w}\mathbf{w}}$ resulting from the orthogonalisation, in principle there are 19 relaxation parameters λ to be determined. Taking into account the physics described here, this number reduces immediately to six as the components of tensorial properties represented by different moments still need to behave in the same way. This is further reduced by conservation requirements. As is directly clear the relaxation of the conserved moments is arbitrary and the parameters are chosen $\lambda_0 = 0, \lambda_3 = \lambda_5 = \lambda_7 = 1$. Furthermore owing to isotropy of the system considered, components of a single property represented by different moments are assigned equal relaxation parameters. In detail these are the ones for the energy flux $\lambda_4 = \lambda_6 = \lambda_8 = \lambda_{\mathbf{q}}$, the viscous stress tensor $\lambda_9 = \lambda_{11} = \lambda_{13} = \lambda_{14} = \lambda_{15} = \lambda_{\mathbf{v}}$ the fourth order moment of viscous stress tensor symmetry $\lambda_{10} = \lambda_{12} = \lambda_{\boldsymbol{\pi}}$ and the third order moment $\lambda_{16} = \lambda_{17} = \lambda_{18} = \lambda_{\mathbf{m}}$.

In order to recover the LBGK relaxation behaviour with $\tau = 1.0$, the weights need to be set $w_\epsilon = 3, w_{\epsilon j} = -11/2$ and $w_{\mathbf{w}\mathbf{w}} = -1/2$ as well as all relaxation parameters $\lambda_0 \dots \lambda_{18} = 1.0$.

Researching the accuracy of solutions obtained by the generalised lattice Boltzmann formalism, Ginzburg et al. introduced a two relaxation time (TRT) scheme in which two relaxation parameters are defined for moments of even and odd order respectively (which is equivalent to apply relaxation rules per signum of the lattice vector, dependent on the form) [284]. This approach can be shown to completely remove the viscosity dependent error of boundary conditions. Moreover certain different choices of relaxation parameter relations allow for optimisation of accuracy in other properties, such as diffusivity [222]. An in depth evaluation of the influence of collision schemes and boundary conditions can be found in [285].

Index	Moment	Equilibrium	Relaxation frequency λ		
			BGK	TRT	MRT
0	ρ	ρ	0	0	0
1	e	$-11\rho + \frac{19}{\rho_0} (j_x^2 + j_y^2 + j_z^2)$	1	λ_v	λ_e
2	ϵ	$w_\epsilon \rho + \frac{w_{\epsilon j}}{\rho_0} (j_x^2 + j_y^2 + j_z^2)$	1	λ_v	λ_ϵ
3	j_x	j_x	0	1	1
4	q_x	$-\frac{2}{3}j_x + \frac{5}{2} \frac{j_x}{\rho^2} (j_y^2 + j_z^2)$	1	λ_q	λ_q
5	j_y	j_y	0	1	1
6	q_y	$-\frac{2}{3}j_y + \frac{5}{2} \frac{j_y}{\rho^2} (j_z^2 + j_x^2)$	1	λ_q	λ_q
7	j_z	j_z	0	1	1
8	q_z	$-\frac{2}{3}j_z + \frac{5}{2} \frac{j_z}{\rho^2} (j_x^2 + j_y^2)$	1	λ_q	λ_q
9	$3p_{xx}$	$\frac{1}{3\rho_0} [2j_x^2 - (j_y^2 + j_z^2)]$	1	λ_v	λ_v
10	$3\pi_{xx}$	$\frac{w_{ww}}{3\rho_0} [2j_x^2 - (j_y^2 + j_z^2)]$	1	λ_v	λ_π
11	p_{ww}	$\frac{1}{\rho_0} (j_y^2 - j_z^2)$	1	λ_v	λ_v
12	π_{ww}	$\frac{w_{ww}}{\rho_0} (j_y^2 - j_z^2)$	1	λ_v	λ_π
13	p_{xy}	$\frac{1}{\rho_0} j_{xy}$	1	λ_v	λ_v
14	p_{yz}	$\frac{1}{\rho_0} j_{yz}$	1	λ_v	λ_v
15	p_{xz}	$\frac{1}{\rho_0} j_{xz}$	1	λ_v	λ_v
16	m_x	$\frac{3}{2} \frac{j_x}{\rho^2} (j_y^2 - j_z^2)$	1	λ_q	λ_m
17	m_y	$\frac{3}{2} \frac{j_y}{\rho^2} (j_z^2 - j_x^2)$	1	λ_q	λ_m
18	m_z	$\frac{3}{2} \frac{j_z}{\rho^2} (j_x^2 - j_y^2)$	1	λ_q	λ_m

Table 4.1: Overview of the moments, equilibria and relaxation parameters employed by different models. Different to models prominently reported on, the third order expansion equilibrium distribution, Eq. (2.4) yields additional terms $\propto \frac{j_i}{\rho^2} (j_j^2 \pm j_k^2)$ in the odd ordered energy flux related moments q and m . Weights are kept at the BGK parameterisation $w_\epsilon = 3, w_{\epsilon j} = -11/2$ and $w_{ww} = -1/2$ for all collision schemes.

As we are using the equilibrium formulation of the TRT approach, the shear viscosity determining relaxation parameter for the non-conserved moments of even order remains

$$\lambda_v = \frac{1}{\tau} = \frac{1}{3\nu + \frac{1}{2}}, \quad (4.9)$$

and the one for the non-conserved moments of odd order, the energy flux q and ghost

modes m is [284, 285]

$$\lambda_q = 8 \frac{(2 - \lambda_v)}{(8 - \lambda_v)} = 8 \frac{(2\tau - 1)}{(8\tau - 1)} = \frac{16\nu}{8\nu + 1}. \quad (4.10)$$

Even though the development of the method started some decades ago in the context of lattice gas systems already [286], there are still current developments especially in the understanding and extending of collision formalisms, including discussions on energy conserving schemes [287]. This is also relevant in the context of a consistent parameterisation of the MRT collision scheme making use of the bulk viscosity parameterisation. Only recently it has been found that in order to be able to vary the relaxation times of the energy modes another constant relation has to be established [282].

4.3 Validation

In order to validate the implementation of the multi relaxation time collision scheme introduced in section 4.2.2 benchmark runs were executed to evaluate the behaviour of the model with respect to variation of the relevant coupling and transport parameters on their own and in the interplay with boundary conditions, respectively.

4.3.1 Surface tension

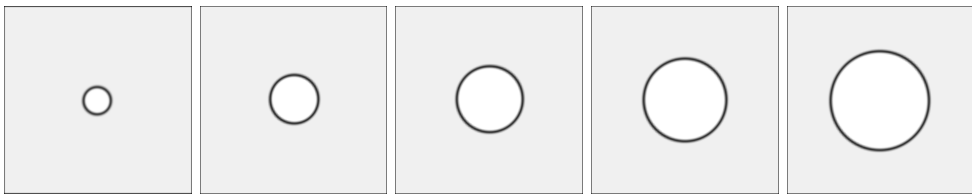


Figure 4.2: *Illustration of simulated systems used to measure the surface tension via the Laplace pressure in a pseudo-2d system. The post-processing defines the mean density of the droplet component α as black. This is emphasising the interface in renditions of the density data as the mean value is assumed only there. Depicted are system states for droplets initialised with discrete radii of 15, 20, 25, 30 and 35 lattice sites in a system with no surfactant and a coupling of $\mathcal{G}_{\alpha\bar{\alpha}} = 0.12$ in the steady state after 200,000 time steps.*

The surface tension parameterisation of the model is tested by evaluation of the Laplace law, Eq. (2.17), in pseudo-2d systems as depicted in Fig. 4.2. In this case,

the curvature term is given by $k = 1/R$ and as expression for the surface tension follows

$$\gamma = R\nabla p. \quad (4.11)$$

The pressure inside and outside of the droplet is measured by an extended pressure term taking into account the non-ideal contributions of the pseudo-potential forces

$$p(\mathbf{x}) = c_s [\rho^\alpha + \rho^{\bar{\alpha}} + \rho^\sigma + 2(\mathcal{G}_{\alpha\bar{\alpha}}\psi^\alpha\psi^{\bar{\alpha}} + \mathcal{G}_{\alpha\sigma}\psi^\alpha\psi^\sigma + \mathcal{G}_{\alpha\sigma}\psi^{\bar{\alpha}}\psi^\sigma) + \mathcal{G}_{\sigma\sigma}\psi^\sigma\psi^\sigma]. \quad (4.12)$$

Herein restrictions of the coupling have been included, namely the equality of interactions of the immiscible components with the surfactant $\mathcal{G}_{\bar{\alpha}\sigma} = \mathcal{G}_{\alpha\sigma}$ and the absence of self interactions in those components $\mathcal{G}_{\alpha\alpha} = \mathcal{G}_{\bar{\alpha}\bar{\alpha}} = 0$.

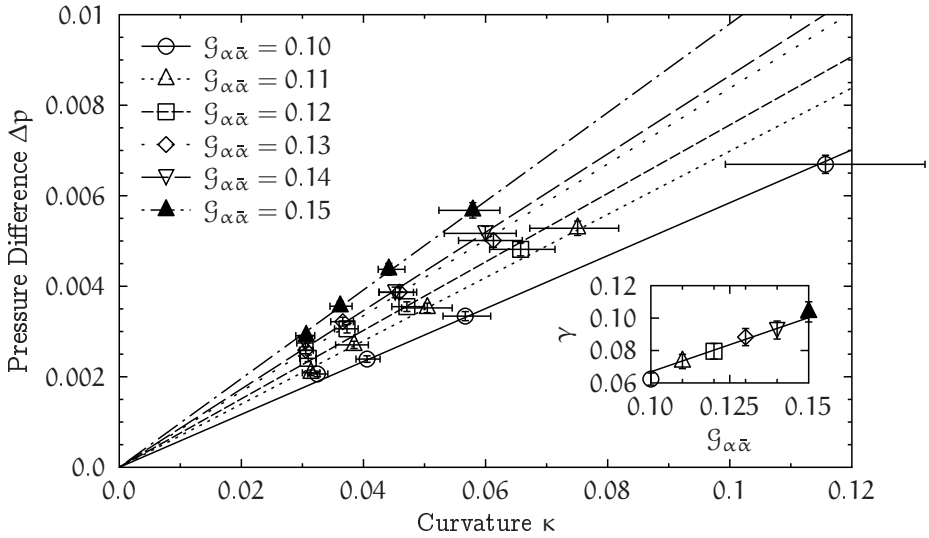


Figure 4.3: *Reproduction of the Young-Laplace law in a pseudo-2d system of size $128 \times 128 \times 2$. Plotted is the pressure difference across the surface of a droplet as determined by measurement of the lattice Boltzmann lattice density in the system centre and a corner point. The surface tension observed in the system increases with the coupling parameter $\mathcal{G}_{\alpha\bar{\alpha}}$ (see inset). Deviations in linearity can be attributed to slight differences in system initialisation pressures for different droplet sizes (As the droplet mass doubles as parameter for the pressure as well - compare Eq. (4.12)). Error bars of the curvature values are given by the deviations in droplet radius measurement due to the diffuse interface. The error is in particular pronounced for droplets with high curvature, i.e. small radii.*

For the measurements we initialise a system of size $128 \times 128 \times 2$ lattice sites with a centred droplet of varied radius $R_{\text{init}} \in \{15, 20, 25, 30, 35\}$ in lattice units. Taken into

account the chosen form of the pseudo-potential Eq. (2.40) and stability considerations, initial densities are chosen to be $\rho_\alpha = \rho_{\bar{\alpha}} = 0.7$. The surface tension is varied by the coupling strength $\mathcal{G}_{\alpha\bar{\alpha}} \in \{0.10, 0.11, 0.12, 0.13, 0.14, 0.15\}$. Where the lower bound is motivated by a restriction to a maximum interface width of 5 lattice sites taken into consideration. The upper bound is determined by numerical instability arising for higher interaction strengths. Depending on the coupling parameter the systems equilibrate after a run time between 100,000 and 200,000 time steps, where for convenience we measure all values at 200,000 time steps.

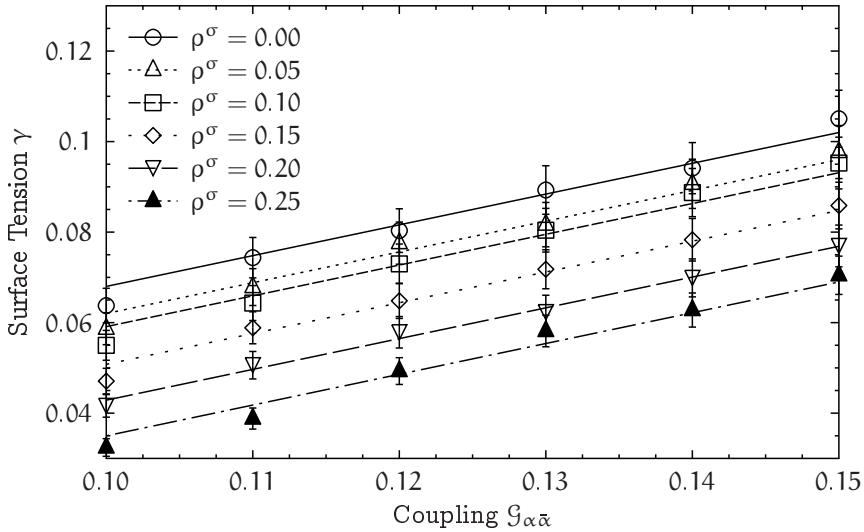


Figure 4.4: *Surface tension as a function of the coupling parameter $\mathcal{G}_{\alpha\bar{\alpha}}$ for different initial surfactant densities ρ_σ^{init} , measured in a pseudo-2d droplet system. A consistent reduction in surface tension can be observed. The derivation of these values from perturbed surface tension data points increases the error observed to the order of 6 per cent. Nonetheless, the qualitative reduction of surface tension by added surfactant in the order of 40 to 50 per cent can be seen.*

Due to the diffuse interface and the non-negligible minority concentration of the droplet fluid component in the equilibrated system outside of the droplet, the resulting droplet radius differs from the initial values and has to be measured for each case. This is done measuring the droplet volume with respect to an effective density, a procedure introduced by Stefan Frijters [260]. In order to account for the finite minority density the effective density is defined as the difference between the majority density ρ_α^+ measured in the droplet centre and the minority density $\rho_{\bar{\alpha}}^-$ measured in the system corner at the point of maximum distance to the droplet centre $\rho_\alpha^{\text{eff}} = \rho_\alpha^+ - \rho_{\bar{\alpha}}^-$. With this, the mass of the droplet is equivalent to the integral over the effective density in

the system $m = \sum \rho_\alpha^{\text{eff}}$ and the radius can be calculated as

$$R = \sqrt{\frac{1}{4\pi} \frac{m}{\rho_\alpha}}. \quad (4.13)$$

Alternatively, the droplet radius has been determined by simple measurement of the radius proportional to a density offset of

$$\rho_\alpha = \frac{\rho_\alpha^+ - \rho_\alpha^-}{2} \quad (4.14)$$

from the density field of the droplet component α . The variance in the radius as determined by the two methods is in the order of a few percent.

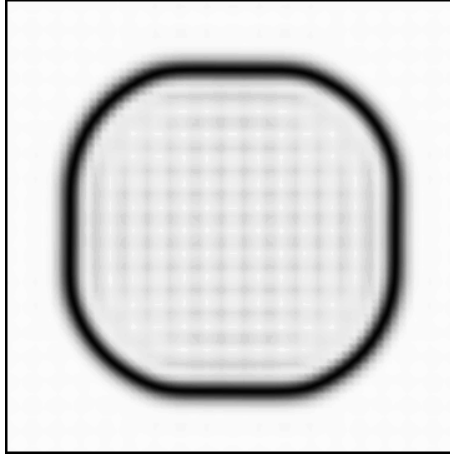


Figure 4.5: *Illustration of over-saturation effects for initial surfactant densities larger than $\rho_\sigma^{\text{init}} = 0.25$ (Depicted is a snapshot for $\rho_\sigma^{\text{init}} = 0.30, \mathcal{G}_{\alpha\bar{\alpha}} = 0.12$). The interaction of the dipole field modelling the surfactant orientation introduces a dominant interaction alongside the lattice edges rendering the model nonphysical. The droplet radius in comparison to the simulation domain ($R = 35$ l.u. vs $X = 128$ l.u.) is contributing to the error as well.*

The expected linear dependence of the surface tension on the coupling strength is found. Figure 4.3 shows the measured pressure difference between the centre of the droplets and a corner of the system for different coupling strength and initial droplet radii together with a fitted line through the origin. Deviations can here be attributed to variations in the initial pressure of the system in the order of under one per cent and, more prominently, errors in the geometrical measurement of the droplet curvature. The diffuse interface introduces here especially for small droplets with high curvatures errors of up to 10 per cent.

Values for the surface tension are determined by a Levenberg-Marquart fit of a linear function through the origin. Despite the variation the error in the fitting algorithm is

controlled well in the order of a few percent. Omitting the extremal coupling values, excellent agreement of the surface tension as linear function of the coupling is found for

$$\gamma = 0.67 \cdot \mathcal{G}_{\alpha\bar{\alpha}}. \quad (4.15)$$

In order to investigate the influence of added surfactant on the surface tensions measured in the system, the surfactant concentration is varied by adding an initially homogeneous surfactant concentration $\chi_{\text{init}}^{\sigma} \in \{0.05, 0.10, 0.15, 0.20, 0.25, 0.30\}$. Here, in order to limit the parameter space, the coupling strengths are kept to values determined by stability considerations $\mathcal{G}_{\alpha\sigma} = \mathcal{G}_{\sigma\sigma} = -0.005$. Here, again an equilibration time of 200,000 time steps is prescribed before measurements are taken. In this time the system reaches a completely stationary state.

Figure 4.4 shows the resulting surface tension measurements over initial surfactant concentration. A consistent reduction in surface tension can be observed. Fitted linear functions suggesting a qualitative reduction in surface tension, where zero surface tension can be reached for non-zero coupling strengths. The data exhibit however large variance. This can be attributed to the system resolution and the interplay of the interface regions with the surfactant concentration, introducing another source of finite size effects. A significant increase in size of the simulated domain to mend these issues has been omitted in the scope of this work. Further deviations can be introduced by non-physical over-saturation effects observed for surfactant concentrations larger than $\chi_{\text{init}}^{\sigma} = 0.25$ as illustrated in figure 4.5. Further investigation and possible correction of these effects is possible by exploration of the parameter space of $\mathcal{G}_{\alpha\sigma}$ and $\mathcal{G}_{\sigma\sigma}$. Due to the extensive work required to do so, this can however not be part of this thesis.

The measurements allow to qualitatively approximate the maximum relative reduction of surface tension induced by the parameter set in use to be of the order of 40 per cent. The investigations presented below suggest however, that already this range suffices to significantly change system behaviour of the ternary model.

4.3.2 Wettability

In section 2.5, Eq. (2.48) a pseudo-potential wall interaction is introduced. Here it is employed to vary the static contact angle Θ of a droplet at a wall boundary where in addition simple bounce-back boundary conditions 2.5.2 are applied to model a no-slip surface.

For a constant wall potential $s = 1.0$ the surface tension at the wall is varied by prescribing individual wall coupling strengths $\mathcal{G}_{\omega\alpha}$ and $\mathcal{G}_{\omega\bar{\alpha}}$. The whole range of

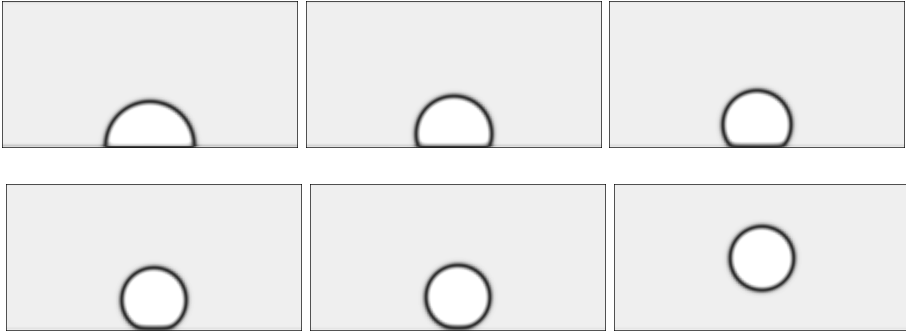


Figure 4.6: *Illustration of contact angle measurements in the dewetting regime. The post-processing defines the mean density of component α as black, emphasising the interface in renditions of the density data. Depicted are system states for droplet initialised with wall interactions of $\mathcal{G}_{\omega\alpha} = -\mathcal{G}_{\omega\bar{\alpha}} = 0.0, 0.005, 0.010, 0.015, 0.017, 0.018$ in a system with no surfactant and a coupling of $\mathcal{G}_{\alpha\bar{\alpha}} = 0.12$ in the steady state after 200,000 time steps. Nonphysical super critical interaction is observed for the strongest coupling strength, effectively repelling the droplet.*

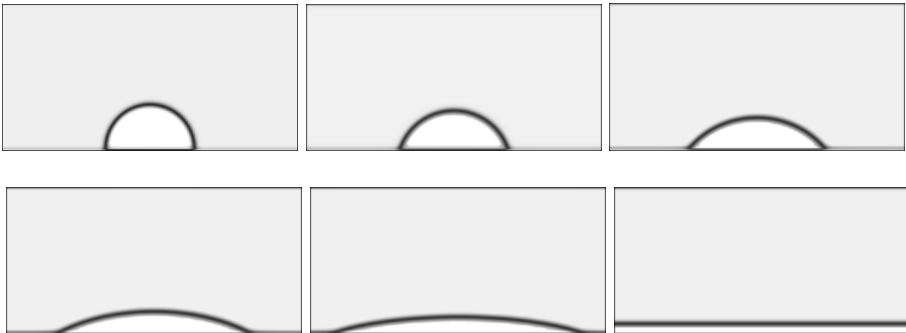


Figure 4.7: *Illustration of contact angle measurements in the wetting regime. The post-processing defines the mean density of component α as black, emphasising the interface in renditions of the density data. Depicted are system states for droplet initialised with wall interactions of $\mathcal{G}_{\omega\alpha} = -\mathcal{G}_{\omega\bar{\alpha}} = 0.0, -0.005, -0.010, -0.015, -0.017, -0.018$ in a system with no surfactant and a coupling of $\mathcal{G}_{\alpha\bar{\alpha}} = 0.12$ in the steady state after 200,000 time steps. Film formation is observed for the strongest coupling strength.*

contact angles is covered by tuning attractive and repulsive interactions between the wall and the respective components. With this, the Young law can be approximated in terms of the coupling parameters as [140]

$$\Theta = \tan^{-1} \left(\frac{\mathcal{G}_{\omega\bar{\alpha}} - \mathcal{G}_{\omega\alpha}}{\mathcal{G}_{\alpha\bar{\alpha}} \frac{\rho_{\bar{\alpha}}^+ - \rho_{\bar{\alpha}}}{2}} \right). \quad (4.16)$$

The approach allows to model different resulting contact angles both by e.g. active dewetting by repulsive interactions as well as by relatively smaller attractive interactions. For our first study we consider exclusively attractive interactions, reaching the neutral wetting case for both wall coupling values vanishing $\mathcal{G}_{\omega\alpha} = \mathcal{G}_{\omega\bar{\alpha}} = 0$.

In the current setup, surfactant wall interactions are neutral, i.e. there is no direct forcing component in place with respect to dipoles and surfactant density. Indirect interactions exist however due to the interaction between wall and fluid components and subsequent change in densities coupled to the surfactant component. The qualitative validity of this approach is documented in the context of Fig. 4.9 where the fluid fluid interaction has been scaled with the effective reduction observed in Laplace measurements involving surfactant, compare Fig. 4.4.

Contact angle

The resulting dependency of the contact angle on the coupling strengths is shown in Figure 4.8. System illustration can be found in Figs. 4.6 and 4.7. Here we have varied the coupling strength in the respective attractive range for either the droplet or ambient component in the range $\mathcal{G}_{\omega\bar{\alpha}} \in \{-0.018...0.018\}$ in steps of 0.001. Simulations have been performed in a pseudo-2d system of 64x2x128 lattice sites size. The droplet is initialised as a circular column of radius 16 lattice sites in contact with a wall in the $z = 0$ plane, centred in x-direction at $x = 64$. Both initial densities are chosen to be $\rho_{\alpha} = \rho_{\bar{\alpha}} = 0.7$.

As in [140], in order to determine the contact angle, a spherical shape of the droplet surface is assumed. The contact angle can then be calculated from the droplet base radius and height

$$\Theta = \pi - \tan^{-1} \left(\frac{B/2}{R - H} \right), \quad R = \frac{4H^2 + B^2}{8H}. \quad (4.17)$$

Here we make use of the measurement technique introduced in 4.3.1 to set the density cut-off at which we define the droplet interface for our calculations to $\rho \approx 1.5\rho_{\bar{\alpha}}$. As attractive interaction in the wall vicinity can lead to a significant increase in local density in the boundary layer, (interpretable as equivalent to precursor formation)

the algorithm is modified for the determination of the base width. Here, instead of the global minimum density, the minimum density in the boundary layer is considered to calculate the threshold.

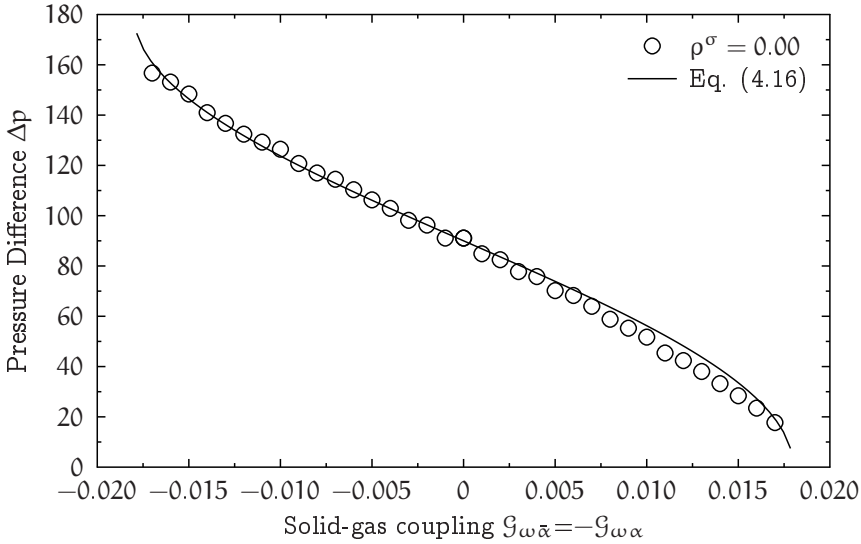


Figure 4.8: *The contact angle measured from the droplet geometry, Eq. (4.17) plotted over the wall coupling of the binary components $G_{\bar{\alpha}\omega} = -G_{\alpha\omega}$, compare section 2.5.2. for a fluid-fluid coupling strength of $G_{\alpha\bar{\alpha}} = 0.12$. The prediction by Eq. (4.16) shows good agreement. For stronger attractive coupling, the local density field in the vicinity of the wall is increasingly distorted by the solid-fluid interactions, introducing a perturbation to the fluid density threshold in the prediction and subsequently a larger error in the geometry measurements.*

Also in this system, the effect of adding a surfactant component is studied. Initial surfactant densities of $\rho_{\sigma}^{\text{init}} \in \{0.05, 0.10, 0.15, 0.20, 0.25\}$ are introduced. Figure 4.9 shows the qualitative change in behaviour of the contact angle of a droplet with the introduction of surfactant. Due to the reduction in fluid-fluid interaction strength, the influence of the solid-fluid interaction strength is emphasised. This results in a stronger reaction of the system to changes in fluid-solid interactions and a narrowed parameter space. Both respective hydrophobicity and hydrophilicity are enhanced by the introduction of soluble surfactants with negligible wall interactions.

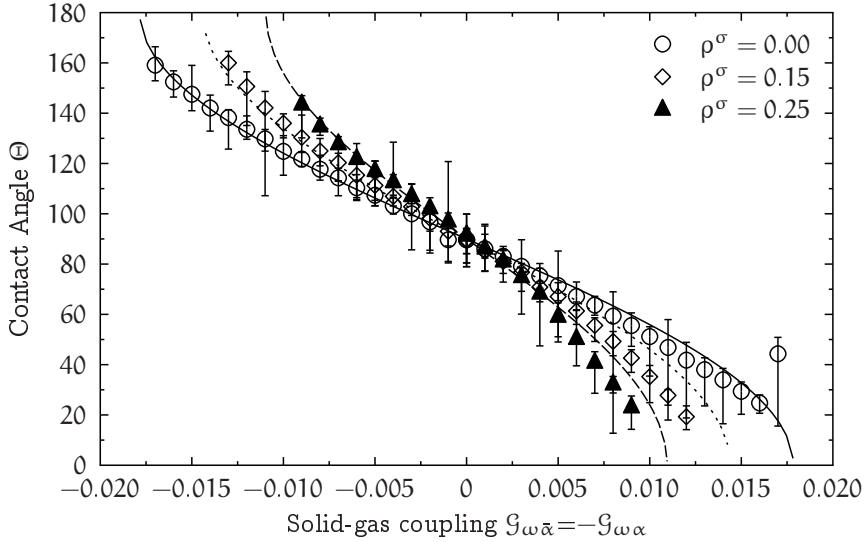


Figure 4.9: Plot of the contact angle Θ over coupling strength $\mathcal{G}_{\alpha\omega}$ for different surfactant concentrations. In the chosen parameterisation as a soluble surfactant with minimal wall interaction, an increase in contact angle is observed following from the reduction in fluid-fluid surface tension. While the dewetting case is matching the model prediction of Eq. (4.17) very well, the local density variations occurring in the boundary layer in the wetting case are leading to lower measured contact angles and larger uncertainty. The outlier in the maximally wetting case for the binary mixture results from interplay of the evaluation algorithm and the diffuse interface for very low contact angles.

4.3.3 Diffusivity

In order to evaluate the diffusivity behaviour in the method, a pseudo-1d system measuring $2 \times 2 \times 64$ lattice sites is initialised with demixed miscible fluid components. Employing periodic boundary conditions this is sufficient to capture the full 3d behaviour. The system contains pure fluid of either component in half the z-direction, starting with component α from $z = 0$ and $\bar{\alpha}$ from $z = 32$. The initial densities are set to equal $\rho_\alpha = \rho_{\bar{\alpha}} = 0.7$, in a second step again, surfactant is added at homogeneous concentration throughout the system. The time to reach equilibrium differs strongly, ranging from a couple of thousand to several ten thousand time steps. For convenience all systems were simulated for 30,000 time steps.

Mutual diffusivity of the components in the miscible regime is measured for coupling parameters of $\mathcal{G}_{\alpha\alpha} \in \{0.01, 0.02, 0.03, 0.04, 0.05, 0.06\}$.

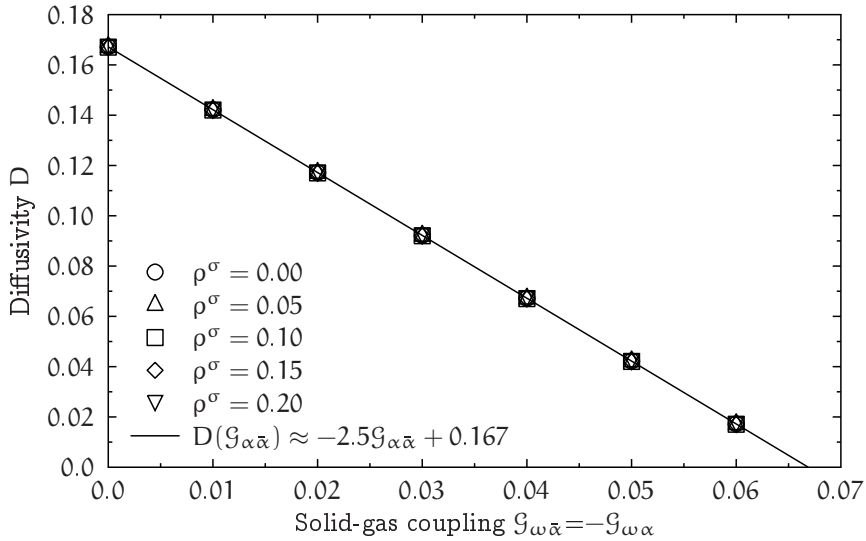


Figure 4.10: Diffusivity D over coupling strength $G_{\alpha\bar{\alpha}}$ in lattice units. A clear linear correlation between the coupling parameter $G_{\alpha\bar{\alpha}}$ and the diffusivity $D_{\alpha\bar{\alpha}}$ is observed. The influence of even high surfactant concentration on the diffusive behaviour of the system is negligible. This is due to the homogeneous distribution of the surfactant component in the system, resulting in symmetrical interactions which cancel out.

Two sources of error are taken into account. The first one is a shock-wave like distortion resulting from the discrete initialisation of the system. The second one is introduced when the system approaches equilibrium, when the time and second spatial derivatives compared both are approaching zero and small deviations introduce a very large error.

The initial distortion is proportional to the coupling strength and is therefore more pronounced at high coupling and low diffusivity. In this case the equilibration is however delayed, so that a longer window of measurement exists. Without any coupling the measurement window chosen is between 1,500 and 2,500 time steps, whereas for the highest tested coupling the measurement window is between 15,000 and 30,000 time steps.

Special attention has to be paid on the data resolution in time and space in order to minimise the error of measurement of both the time derivative as well as second spatial derivative [288]. We find that in order to adequately reproduce Eq. (2.13) data from every single time step has to be taken into account. Figure 4.10 shows the

diffusivity according to Eq. (2.13) over the coupling parameter. Excellent functional agreement is found, where the fitted equation is

$$\mathcal{D} = -\frac{5}{2}\mathcal{G}_{\alpha\bar{\alpha}} + \frac{1}{6}. \quad (4.18)$$

The simulation series was repeated adding surfactant concentrations of $\rho_{\sigma}^{\text{init}} \in \{0.05, 0.10, 0.15, 0.20\}$ to the system. Even for rather high concentrations, no effect on the diffusivity between the fluid components α and $\bar{\alpha}$ is found. This is due to the homogeneous initialisation of the surfactant component, introducing a symmetrical contribution to the interactions. The change in time and space then keeps to be governed by the asymmetrical fluid fluid interaction strengths which thus determines the diffusivity of the ternary system.

4.3.4 Permeability

As outlined in the introduction, one of the central motivations to introduce the overhead of a MRT collision scheme is the resolution of the viscosity dependent error observed in boundary conditions. Not only does this help to increase the overall accuracy, but furthermore allows a trade off between discretisation error and a reduction in the required resolution for systems in which many constrictions govern the flow.

As benchmark to evaluate the reduction in viscosity dependent error, the theoretical accessible permeability of a square duct is evaluated [139, 260, 289]. Here we compare three relaxation approaches, the classic LBGK model, a naive MRT approach where all relaxation parameters not related to the kinematic shear stress are kept equal to one (MRT1) and a two relaxation time approach where two coupled relaxation times are employed to reduce (eliminate) the viscosity dependency of the simulated boundary position.

The permeability κ , together with viscosity, forms the proportionality factor for the flow rate \dot{Q} of fluid through a medium and an applied pressure gradient ∇p . It is a material property of porous media defined based on experiments by Darcy in the 19th century [145] (see also Sec. 2.3.3).

Following similar work on boundary conditions and collision schemes in single phase simulations performed by Narvaez et al. [139], results are compared with a theoretical solution for Poiseuille flow through a square duct of side length B that has been constructed by the series [289]

$$\kappa^{\text{th}} = \lim_{M \rightarrow \infty} \frac{B^2}{4} \left(\frac{1}{3} - \frac{64}{\pi^5} \sum_{n=0}^M \frac{\tanh((2n+1)(\pi/2))}{(2n+1)^5} \right). \quad (4.19)$$

Here the exact solution is obtained in the limit $\lim_{M \rightarrow \infty} \mathbf{u}(x, y, M)$. For practical purposes, a result convergent at machine precision is obtained for $M = 200$, already (compare [139]).

The value determined by the theory is compared against measurements in the lattice Boltzmann system using the transformed Darcy law Eq. (2.23), giving the permeability

$$\kappa^{\text{sim}} = \eta \frac{\langle \mathbf{u} \rangle}{\langle \rho F^z \rangle}, \quad (4.20)$$

where for the flow rate \dot{Q} the mean velocity $\langle \mathbf{u} \rangle$ is substituted and the expression $\langle \rho F^z \rangle$, the mean body force applied in z -direction multiplied by the fluid density, is equivalent to the applied pressure gradient.

To evaluate Poiseuille flow, a pseudo-2d system measuring only 2 lattice sites in y -direction is sufficient. Two series of simulations were conducted to approximate the error in permeability obtained for a variation in system resolution at a fixed kinematic viscosity on the one hand, and for a variation in kinematic viscosity at a fixed resolution on the other hand.

Figure 4.11 shows the relative error of permeability

$$\epsilon_\kappa = \frac{\kappa^{\text{th}} - \kappa^{\text{sim}}}{\kappa^{\text{th}}} \quad (4.21)$$

measured in the numerical systems as compared to the theoretically obtained values. Keeping the relaxation parameter at $\tau = 1.0$, The side-length B of the system in x - and z -direction is varied between 4 lattice sites and 128 lattice sites. For this case, the MRT1 parameterisation considered here coincides with the LBGK case. The flow is driven by a body force / acceleration of $a = 1 \cdot 10^{-6}$ throughout the system. Simple bounce back boundary conditions are employed in the xy -plane at $x = 0$ and yz -plane at $z = 0$, respectively. For both the LBGK as well as the TRT parameterisation an exponential decrease in relative error with an increase of channel resolution is observed. This is the case, because the error in the overall channel geometry description is limited to the boundary sites and reduces with their relative importance. The error introduced by the TRT scheme is smaller than that of the LBGK for all cases considered. Both models exhibit *outliers* of reduced error for certain relaxation parameters. These are reproducible and related to discretisation artefacts in the intentionally poorly resolved channel, where certain staircase effects will have an over proportional effect on the measured mean flow rate.

The figure 4.12 compares different collision parameterisation employing a LBGK scheme, a naive MRT approach where all relaxation parameters not related to the kinematic shear are kept at $\lambda_\chi = 1.0$ and a TRT approach, designed to eliminate the viscosity depended deviation in simulated boundary position. Simulation data were

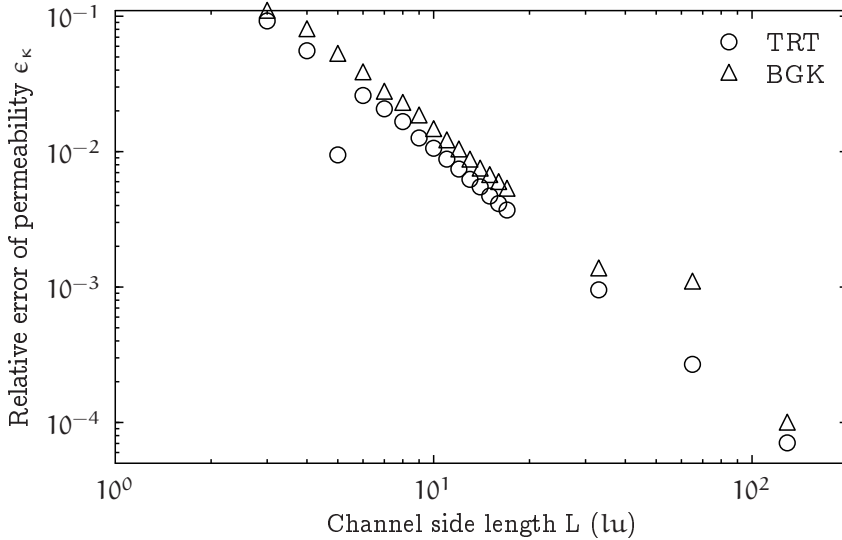


Figure 4.11: *Error in permeability measurement as calculated by Eq. (4.21) over the channel side-length B in lattice units. Depicted are two series for the BGK and TRT model, respectively. While for the TRT approach a small error depending linearly on the viscosity parameter is observed, for the LBGK model the error grows exponentially. For the TRT model the dependence should vanish completely [222], the nature of force implementation in our model reintroduces however a small deviation to be fixed in future work.*

obtained in a channel of lateral length $B = 10$ and permeability values compared calculated from Eqs. 4.19 and 4.20.

The earlier reported functional dependency of error in permeability for the respective LBGK and MRT schemes is recovered, exhibiting non-linear behaviour in the case of LBGK and linear behaviour in the case of MRT implementations. However, in the current form the model cannot recover the theoretically possible elimination of viscosity dependent error. This is true for the non-optimised approach *MRT1* as well as for the TRT parameterisation. The reason for this behaviour is the utilisation of the classic Shan-Chen coupling of the interaction forces via the equilibrium velocity value.

Another side effect of this variant of force integration with the MRT implementation detailed above is the undetermined time scaling when compared with the original LBGK formalism. There the force is scaled with the relaxation time to relate to the resulting pressure gradient. When employing the TRT scheme this scaling changes

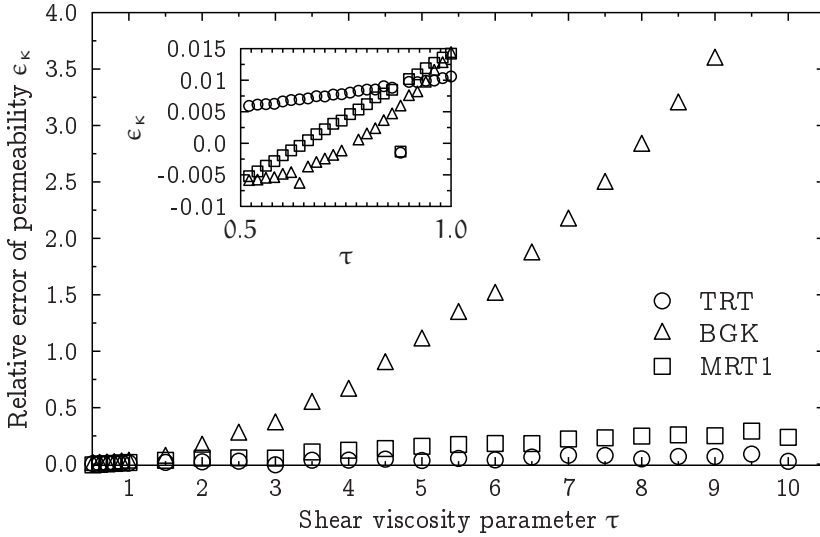


Figure 4.12: *Error in permeability measurement as calculated by Eq. (4.21) over the shear viscosity relaxation parameter λ_ν . Depicted are three series for the BGK, TRT and simple MRT model, respectively. For the TRT approach a small error depending linearly on the viscosity parameter is observed while for the LBGK model the error grows exponentially. For the TRT model the dependence should vanish completely [222], the nature of force implementation in our model reintroduces however a small deviation to be fixed in future work. The simple MRT setup, where only the shear viscosity related relaxation rate is varied from one, exhibits even larger errors while the dependency on the parameter is still linear. See text for further discussion.*

however with respect to the relaxation time-scales. This leads for the employed Shan Chen scheme to increased numerical instability rather than a gain in stability. For this reason in the scope of this thesis, the *MRT1* parameterisation will be employed. While by this the ultimate goal of elimination of the error is not yet reached, the implementation in its current form is sufficient to evaluate the correctness of the algorithm and serve as a milestone on the way to a modified force implementation in the near future. In order to instate second order correctness for of the forcing for multiphase NS equations, the force term has to be introduced as second order truncated expansion in a smallness parameter, analogous to the discretised equilibrium distribution [159]. Working on this thesis, this approach was not taken into account in order to perform the initial implementation work on a system of minimal complexity.

Relative permeability

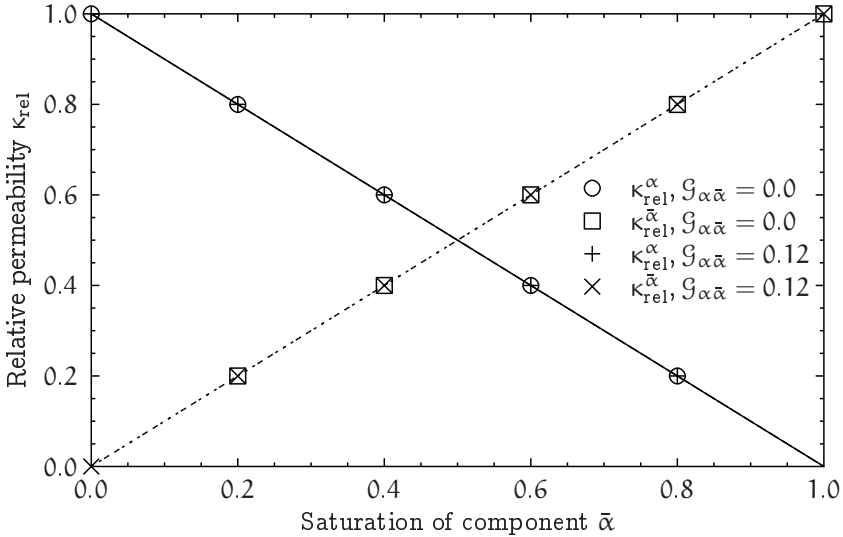


Figure 4.13: *Relative permeability in a square duct for mixed and demixed binary fluid components over their mass fraction in the system. As errors in permeability measurement are of the same order for both the single component and mixture measurements, they cancel each other out in this case. Thus exact agreement between mass fraction and relative permeability is found for this simple model regardless of the presence of an interface in the measurement volume.*

For the case of fluid mixtures, the relative permeability κ_α^r of a component α is given as the ratio of its permeability κ_α in the mixture to the absolute permeability of the medium for a fluid of the same viscosity

$$\kappa_\alpha^r = \frac{\kappa_\alpha}{\kappa}. \quad (4.22)$$

While approximations for the prediction of relative permeabilities have been made, its determination remains one of the most challenging problems in models of multiphase flows in porous media, dependent on a wealth of different factors such as diffusivities, viscosities, wall interactions, concentration fractions and the percolation of phases [73, 75, 290, 291]. In section 4.4 more complex flow examples will be discussed. Figure 4.13 shows that in the case of a simple, neutrally wetting square duct, the relative permeability is solely depending on the mass fraction per component in the system. Varying coupling strengths, the method of measurement was verified to work for both mixed and demixed binary fluids.

4.4 Forced imbibition of a model porous medium

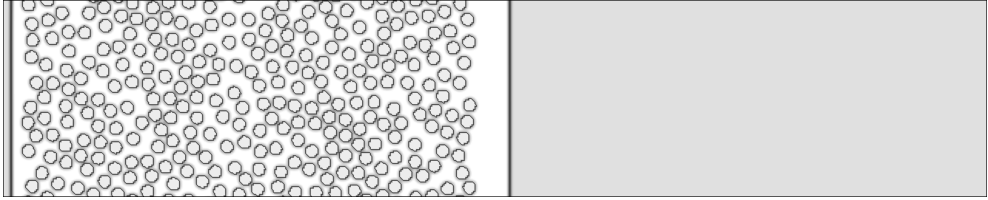


Figure 4.14: *Illustration of the simulation domain, a pseudo-2D system measuring $x = 640, y = 2, z = 128$ lattice sites. In the region between the $x = 20$ and $x = 300$ solid columns of radius $R = 4$ lattice sites have been randomly placed, corresponding to a porosity of 1.68 in this region. In the initial state, the first half between $x = 0$ and $x = 320$ is filled with component α at a density of $\rho_\alpha = 0.7$. The latter half ranging from $x = 320$ to $x = 640$ is filled with component $\bar{\alpha}$ at a density of $\rho_{\bar{\alpha}} = 0.7$. The coupling strength is chosen to be $\mathcal{G}_{\alpha\bar{\alpha}} = 0.12$ throughout the simulations described.*

After evaluation of the model where the principal function is verified, but potential further gains in accuracy by employment of a higher order accurate forcing scheme were identified, here results of simulations of forced imbibition in a pseudo-2d porous medium are presented. This well controlled and comparably computational lightweight model allows for the assessment of the interplay of the parameters and phenomena considered separate from each other in the validation section.

4.4.1 Overview

Figure 4.14 illustrates the simulation domain, a pseudo-2D system measuring $x = 640, y = 2, z = 128$ lattice sites. In the region between $x = 20$ and $x = 300$, solid columns of radius $R = 4$ lattice sites have been randomly placed, respecting periodic boundaries. A porosity of ≈ 0.60 in this region is calculated from the ratio of fluid sites to total sites (26754/44926).

In the initial state, the first half between $x = 0$ and $x = 320$ is filled with component α at a density of $\rho_\alpha = 0.7$, the latter half ranging from $x = 320$ to $x = 640$ is filled with component $\bar{\alpha}$ at a density of $\rho_{\bar{\alpha}} = 0.7$. The coupling strength is chosen to be $\mathcal{G}_{\alpha\bar{\alpha}} = 0.12$ throughout the simulations described. To avoid perturbations due to the initialisation with *sharp* density values, before any imbibition simulation the system is simulated for 1 million time-steps. Subsequent variations in parameters are applied starting from a checkpoint of this system state, where for variations in wettability another relaxation run of 500,000 time steps is performed before starting to drive the

flow. Surfactant is initialised throughout the whole domain at varying concentrations ρ_σ .

4.4.2 Force variation

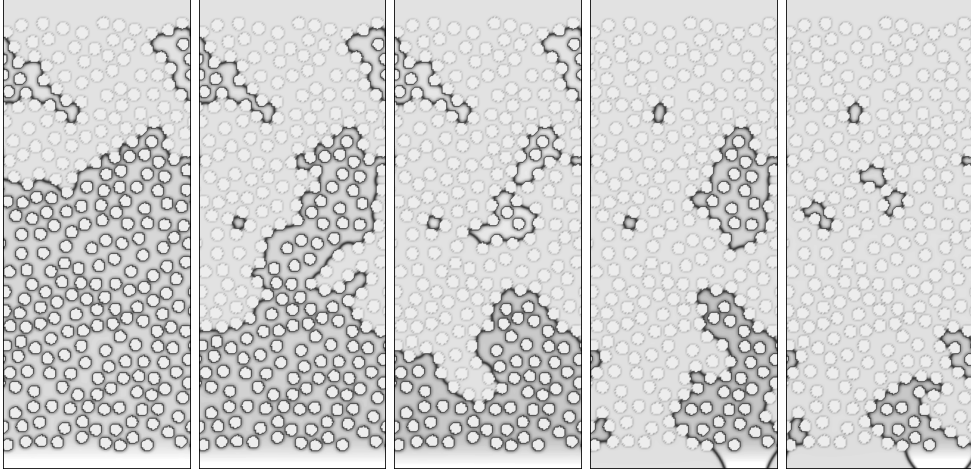


Figure 4.15: *Illustration of final states for different pressure gradients (Body force applied in the range $x = 0$ to $x = 20$). From left to right (in lattice units) $F = \{-1.0 \cdot 10^{-3}, -1.2 \cdot 10^{-3}, -1.4 \cdot 10^{-3}, -1.6 \cdot 10^{-3}, -1.8 \cdot 10^{-3}\}$. Respective time spans to the stationary state are given in Fig. 4.16.*

As central to forced imbibition, this section starts out with variation of the force parameter over the widest possible range in order to assess the different regimes accessible by the model.

All simulations here are executed in a neutrally-wetting system containing no surfactant. Neutral wetting is achieved by deactivating the solid fluid interactions, $\mathcal{G}_{\omega\alpha} = \mathcal{G}_{\omega\bar{\alpha}} = 0.0$. The capillary interaction is then determined by the solid boundaries being force free with respect to the fluid fluid interface, resulting in a contact angle of $\Theta = 90^\circ$. Figure 4.15 illustrates the respective reached stable states of the simulation runs. In figure 4.16, the relative density of the displaced component α in the porous region $x = 20 \dots 300$ over simulation time is depicted.

The body force, directly proportional to the pressure gradient in our model, was varied between $F = 0.8 \cdot 10^{-3}$ and $F = 2.0 \cdot 10^{-3}$. At lower forcing of up to $F = 1.4 \cdot 10^{-3}$, eventual arrest of the flow by capillary forces is observed. Starting from $F = 1.6 \cdot 10^{-3}$, the flow eventually breaks through the porous section, but is leaving a constant residual concentration of the displaced component α behind. With further increasing

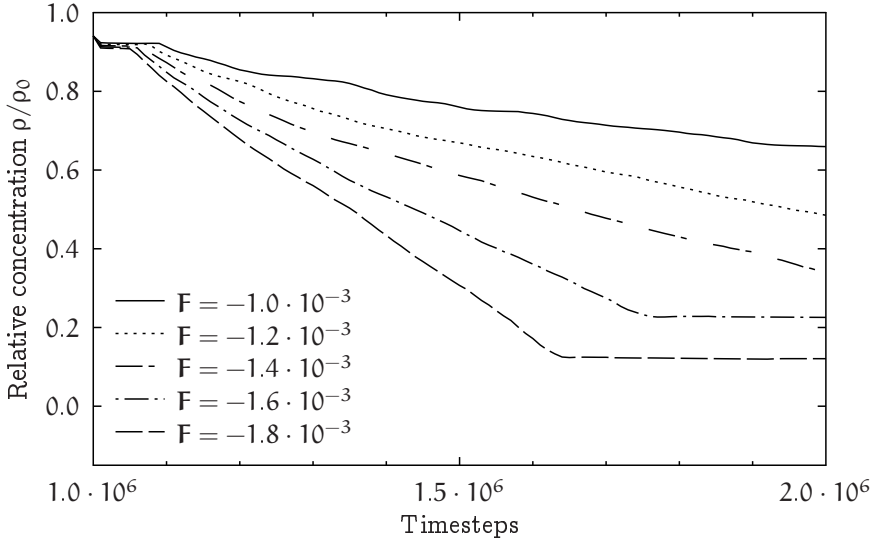


Figure 4.16: Relative density of the displaced component α in the porous region $x = 20 \dots 300$ over simulation time for varied pressure gradients (driving force) in a neutrally-wetting system containing no surfactant. The body force, directly proportional to the pressure gradient in our model, was varied between $F = 1 \cdot 10^{-3}$ and $F = 2 \cdot 10^{-3}$. At lower pressure gradients flow is eventually inhibited by the resistance imposed through capillary forces. At higher pressures, a flow through the medium is established were a stable residual concentration of component α exists. Subsequently raised pressure reduces the residual fluid concentration, compare Fig. 4.15.

pressure the amount of residual fluid is further decreased.

4.4.3 Wettability variation

For a case of an intermediate driving force of $F = 1.0 \cdot 10^{-4}$, where early arrest of the flow was observed, simulations varying the wetting behaviour of the displaced fluid are performed with a focus on the dewetting behaviour. The contact angle is varied in 7 steps ranging from $\Theta \approx 30^\circ$ to $\Theta \approx 150^\circ$, corresponding to strong wetting and strong dewetting behaviour.

This is achieved by variation of the solid liquid interaction parameters $\mathcal{G}_{\omega\alpha}$ and $\mathcal{G}_{\omega\bar{\alpha}}$,

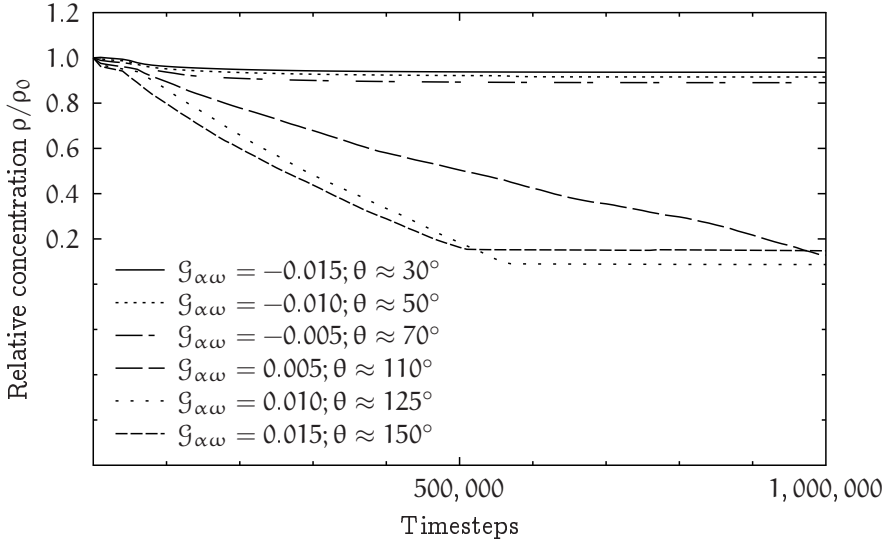


Figure 4.17: *Relative density of the displaced component α in the porous region $x = 20 \dots 300$ over simulation time for wettability variation at a driving force of $F = 1.6 \cdot 10^{-4}$ in a system containing no surfactant. The contact angle of the displaced fluid was varied between $\Theta = 30^\circ$ and $\Theta = 150^\circ$. In the regime considered to drive the flow, even small wetting contact angles induce early arrest of the flow. In case of very high wettability ($\Theta = 30^\circ$), the fluid is stabilised in the medium and no flow is observed at all. At a very high contact angle of $\Theta \approx 150^\circ$, a change in the resulting differences in the stationary fluid distribution is observed. With vanishing friction in the system, the preferred path of flow changes and the structure of the residual fluid volume actually increases.*

where following [140], the parameters were changed as

$$\mathcal{G}_{\omega\alpha} = -\mathcal{G}_{\omega\bar{\alpha}} \in \{-0.015, -0.010, -0.005, 0.0, 0.005, 0.010, 0.015\}.$$

The solid potential was set to be $\psi^\omega = 1$ (compare section 2.5.2).

In figure 4.16, again the relative density of the displaced component α in the porous region $x = 20 \dots 300$ over simulation time is depicted. Wetting interactions move the interface further forward and eventually prohibit intrusion of the displacing fluid into the porous medium altogether. Already very weak dewetting interactions induce a *breakthrough* of the flow. With increasing dewetting interaction strength the flow rate is consistently increased. In case of the superhydrophobic regime, the amount of residual fluid however increases again, suggesting that the absence of friction serves here to change the principal flow through the medium.

4.4.4 Surfactant concentration variation

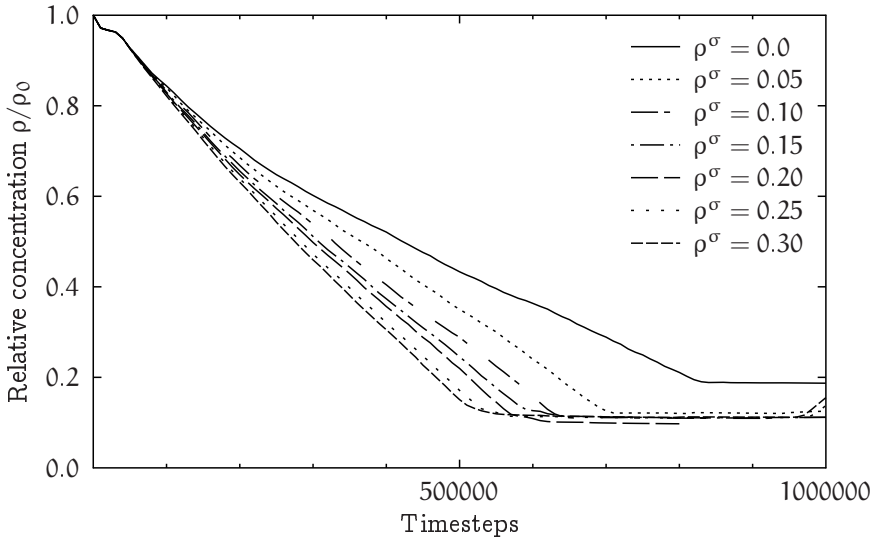


Figure 4.18: *Relative density of the displaced component α in the porous region $x = 20 \dots 300$ over simulation time for varied inflow surfactant concentration at $F = 1.6 \cdot 10^{-4}$ and $\Theta = 90^\circ$. The concentration of surfactant species in the in-flowing fluid was varied between $\rho_\sigma = 0.0$ and $\rho_\sigma = 0.3$*

In a last set of parameter studies, the influence of an added surfactant concentration in the imbibing fluid is investigated. The driving force is kept constant at $F = 1.6 \cdot 10^{-4}$. In addition, neutral wetting behaviour ($\Theta = 90^\circ$) is prescribed again. The concentration of surfactant species in the fluid domain is varied between $\rho_\sigma = 0.0$ and $\rho_\sigma = 0.3$ in steps of $\rho_\sigma = 0.05$.

To limit the parameter space, in these simulations the strength of the surfactant-liquid interaction is limited to a single set of parameters $\mathcal{G}_{\alpha\sigma} = \mathcal{G}_{\sigma\sigma} = -0.005$. The sole attractive interactions of the amphiphilic molecule reflected by the negative sign of the coupling parameters, result in soluble surfactant behaviour. The value has been determined by stability considerations. In the current parameterisation setup, the surfactant has only indirect interaction with solid boundaries by means of altering the interactions of the immiscible components at the wall. The reduction in capillary force induced by the addition of surfactant is expressed as an increase in the flow rate towards the steady state.

Figure 4.18 illustrates the central reduction in fluid-fluid interactions as opposed to fluid-solid interactions. While there exist significant differences in displacement veloc-

ity observed for low and high surfactant concentrations, the final density configuration assumed in these simulations is very similar.

While lower concentrations do not alter the principal density distribution in the system, for higher concentration *dissolving* of fluid-fluid interfaces can be observed. Here, in addition to the advective transport induced by the driving force a diffusive regime can be observed. This effect becomes even more pronounced when the surfactant component is added only to the invading fluid component. In the scope of this work this qualitative observation has however not been investigated more closely for a lack of suitable initialisation conditions. In combination with the current pre-relaxation process aiming to reduce distortions at the solid boundaries, non-homogeneous initialisation of the surfactant component resulted in *leakage* of the invading fluid into the system and prevented comparability of the imbibition results. In the interest of more realistic system modelling, the diffusivity of the surfactant component, both in the respective components as well as in the interfaces and boundary layers remains a matter of strong interest.

4.5 Conclusion and Outlook

This chapter provides results of validation and preliminary parameter studies of a new implementation approach to multi-component lattice Boltzmann simulations. A multi-relaxation time collision scheme has been combined with a surfactant model formulated as an extension to the popular pseudo-potential lattice Boltzmann multi-component model.

This step is motivated by applications in multi-component flows in porous media. Such systems are relevant in biological, geological and technological contexts. The inherent locality of lattice Boltzmann implementations lends itself well to the simulation of complex geometries. The simple and efficient LBGK models introduce however in combination with simple boundary conditions significant errors in the boundary positions in systems where only limited resolution is available.

The work presented here makes use of a massive parallel implementation of a surfactant model introduced by Chen et al. While in its current form the model is limited to soluble surfactants with neutral/indirect solid surface interactions, valid qualitative behaviour in terms of effect on the liquid-liquid interaction is reported.

The quantitative analysis of systems containing surfactant component concentrations

has due to the complexity of interplay between the components to be excluded from the scope of this thesis. In the section 4.3, the validity of the newly implemented algorithm with respect to prior simulations in the LBGK context is tested. Here, not only the surface tension and wettability parameterisation of the model is tested, but multi-component diffusive behaviour and permeability as well.

In the context of the permeability measurement evaluation it becomes clear that the current force integration strategy which is left unchanged from the original formulation of the pseudo-potential model is not suitable to ensure error minimisation when combined with the multi relaxation time scheme as it has been implemented here. Thus, after the instructed initial integration of algorithms of minimal complexity, the immediate next steps necessary to maximise accuracy are including the reintegration of the forcing terms as a separately expanded parameter in order to remove the relaxation parameter dependence of the boundary position entirely as well as to increase the implementation stability. Even with this qualification, the results of the model evaluations document the viability of the approach as well as a for now moderate improvement of permeability measurement.

The chapter closes with preliminary parameter studies for the forced imbibition of a model pseudo-2d porous medium, where the impact of variation in pressure gradient, wettability and surfactant concentration in the system are evaluated.

In all cases the average displaced fluid volume is linear over time, where the speed of displacement is directly proportional to the driving force applied to the system. The residual distribution of displaced and displacing fluid components is depending on the geometrical setup where different forcing strengths may result in very similar final states reached at different points in time.

Different from this observation of similar stable configurations for variation in the driving force, in the case of variation in surface wetting, a qualitative change in the flow behaviour is observed in the case of particularly dewetting surfaces. Here, the removal of friction from the balance of forces leads to new flow paths and less efficient displacement.

The addition of surfactant in the concentrations accessible to the model chiefly reduces the required time to reach a final state while the density distribution configurations remain very similar. This can be attributed to the neutral interaction between surfactant and solid considered in these tests.

The range of body force parameters applicable to the model, resulting in stable states of various levels of fluid displacement is identified. In the range of low driving pressure considered, very sensitive behaviour to changes in wettability is observed. There are indications to changes in preferred flow pattern in highly dewetting systems as well.

The introduction of increasing concentrations of surfactant into the system reduced the capillary forces and increases the flow rates.

Sensible next steps to better understand the capabilities and limitations of the model are parameter evaluations of the surfactant component with a possible integration of surfactant wall interactions. A first step into this direction would be the comparison of the parameterisation to 1d porous media models, as e.g. evaluated recently at the group of mesoscopic transport phenomena [292, 293]. Additional effects that need further investigation, especially in the context of more involved relative permeability estimation for real media, are diffusive regimes and precursor formation on the pore scale.

The extension of the model to increase accuracy and stability of simulations in complex geometries allows further investigation of physics and applications beyond the original formulated problem of enhanced oil recovery. Critical flow phenomena like viscous fingering in porous media and the impact of surfactant are open for investigation. Self-organisation phenomena like amphiphilic meso-phases can be revisited in the context of bounded systems potentially suited to control behaviour by manipulating surface interactions.

Chapter 5

Contaminant transport in dilute gas flows

The content of this chapter is based on

S. SCHMIESCHEK, D. K. N. SINZ, F. KELLER, U. NIEKEN AND J. HARTING.
Mesoscopic simulation of diffusive contaminant spreading in gas flows at low pressure
in preparation, 2015

5.1 Introduction

In this chapter the modelling of contaminant transport in a dilute atmospheric flow is investigated. The problem is amongst other applications motivated by the engineering of suppressive flow, expelling and/or keeping organic contaminant molecules out of optical setups. Plastics components utilised in the construction of e.g. UV-lithography optics emit organic molecules which are responsible for the so-called *hazing* of lenses introducing high replacement or maintenance costs. In order to keep the disturbance of the light paths in the optical systems to a minimum, such systems are operated at very low pressures in the order of single digit Pascals. In some setups, Hydrogen flows are introduced to flush the organic contaminants out of the system. Due to the low pressure, in such systems a non-negligible Knudsen number (compare Sec. 2.3.4) and related rarefaction effects, mainly slip flow, is observed. The method developed here is focusing on the introduction of a thermal diffusivity model into such a system by the addition of stochastic al contaminant representatives. The

nature of these systems, the extraordinarily low concentration of contaminants, limits the interactions relevant to a model to the background-gas-contaminant coupling. Contaminant-contaminant and contaminant-background-gas coupling can be omitted since they do contribute very little if anything to the statistics.

With technological advances in the 20th century, such as miniaturisation of micro electrical and bio-medical devices [294, 295], vacuum technology [87], space exploration [34] and production techniques requiring low pressure environments [88, 295] flow systems have become of interest in which the mean free path λ of individual fluid particles is not negligible in comparison to geometry length-scales l . Therefore hydrodynamic models assuming a fluid continuum lose validity as non-equilibrium, kinetic effects gain importance. This transition is commonly quantified by the Knudsen number $Kn = \lambda/l$. In this chapter, results of the development of a model for two phase flow systems with large concentration imbalances in complex geometries at low pressures are reported. These types of system are of importance e.g. for reduction of disturbances and quality improvement in the operation of advanced optical systems used in microchip production [88, 89] and chemical vapour deposition applications [296].

The most prominent macroscopic effect exhibited by flows at a finite Knudsen number is the breakdown of the hydrodynamic (no-slip) boundary condition at a solid surface. A consequence of this, later dubbed *Knudsen Paradox*, was first systematically described by the Danish physicist Martin Knudsen. He found in 1909 that the flow rate through a thin pipe of radius r , resulting from a fixed pressure gradient ∇p does not linearly decrease with the mean pressure p but rather exhibits a minimum once the λ associated with p becomes of the order of r ($Kn \approx 1$) [10]. In the same year Knudsen described another interesting feature of this unintuitive regime, devising a pump without moving parts as he found a temperature gradient in a thin pipe to induce a pressure gradient [11].

Both phenomena can be explained by the existence of a boundary layer in which discontinuities in velocity- and temperature fields exist. This *Knudsen layer* can extend in the order of several mean free paths from a boundary. In this region, the collision rate between fluid particles is reduced. This is due to the collisions between particles and the surface. As the ratio drops, it reaches a threshold beyond which a local equilibrium description of the flow is void. While this has no implications for the validity of the kinetic picture of the Boltzmann equation, the linear relations for shear stress and heat flux assumed in the formulation of the Navier-Stokes equations are no longer valid. However different strategies can be employed to recover working macroscopic models. For the *slip flow regime* at Kn of the order of 0.1 the integration of slip flow boundary conditions into the Navier-Stokes formalism is possible [148]. Up to the so called *transition regime*, starting at Kn of the order of 1, higher order approximations of the Boltzmann equation or moment equations

of the single particle velocity distribution can constitute analytical solutions to some flow fields and provide valuable information about the transport properties in the system [12, 149–151]. Systems comprising flows at Knudsen numbers of an order of $\text{Kn} \geq \mathcal{O}(10)$ require in general discrete particle models to be correctly resolved. As directly solving the Boltzmann equation due to the high dimensionality and general complexity remains a formidable task, models of the transition regime rely on numerical methods. For *free molecular flow* at even higher Knudsen numbers $\text{Kn} > 100$, collision-less Boltzmann models are employed in which kinetic particle interactions are neglected altogether [152].

While numerous numerical approaches capable of simulating flows at finite Knudsen number, including molecular dynamics [297, 298], direct numerical simulation including slip corrections up to second order [148], discrete velocity methods [299], lattice Boltzmann methods [211, 231] and Direct Simulation Monte Carlo (DSMC) [34] exist, the latter is by far the most common and has been largely used to benchmark other approaches. Despite its success in modelling aerodynamics problems in the upper atmosphere it has however become evident that for the case of flows in the lower transient and slip regime the DSMC approach still requires a very large number of particles to properly resolve a given flow problem [300].

Based on directly solving the Boltzmann formalism as well, lattice Boltzmann methods (LBM) too are in principle capable to describe gas flows in arbitrary flow regimes [47]. The commonly used D3Q19 single relaxation time Lattice Boltzmann or lattice BGK model dealing with a linear approach to a discretised Maxwell-Boltzmann equilibrium distribution is however originally set up to recover the Navier-Stokes equations [43]. To extend its applicability to the simulation of low pressure gas flows in the slip flow regime of small non-negligible Knudsen numbers, boundary conditions can be extended to include slip at solid walls [195, 211, 230, 301]. For simulating flows up to moderate Knudsen numbers, phenomenological higher order lattice Boltzmann models introducing wall function formalisms are used [196, 302]. Due to the existing high density gradients and dominating thermal velocity effects however, the LBM alone is not suited for the simulation of diffusive spreading of low concentrated components in rarefied gases. On the other hand the assumed low concentration of the second phase allows for a greatly simplified simulation approach, fully resolving particles where necessary, while maintaining computational efficiency (detailed in Sec. 5.2.2).

In order to increase the numerical efficiency of simulations at low Mach numbers/in the slip flow and transition regime, several approaches involving the extension of existing models and (spatial) hybrid methods have been published. Fan et al. developed a modified DSMC method, called Information Preservation technique to reduce statistical fluctuations associated with DSMC at low Mach numbers [303]. Chun and Koch reduced these fluctuations by solving the linearized Boltzmann equation together with a correction of the particle velocities after the collision step [304]. Hybrid

approaches combining classical Navier-Stokes solvers and DSMC are developed to reduce numerical costs [305, 306]. In these approaches, the computational domain is divided with respect to the local flow regimes and the DSMC method is only used in regions where non-equilibrium effects are dominant. Since the coupling between the grid-based Navier-Stokes solver and the particle based DSMC method is problematic, Burt et al. replaced the grid-based method with a simplified DSMC approach in the continuum region [307]. Besides these hybrid approaches with increase in efficiency in mind other hybrid models have been developed to achieve a higher precision in approximations to solutions of the Boltzmann equation, such as e.g. MD-DSMC hybrid methods [308].

To extend the applicability of the hybrid approach to length and timescales immediately relevant to engineering problems, in the following a new hybrid approach integrating LBM and DSMC simulation elements in a shared simulation domain is detailed. Here, the lattice Boltzmann method serves as an efficient (slip boundary augmented) Navier-Stokes solver for flows in complex geometries whereas a Monte Carlo particle model is used to study diffusion of the dilute contaminants throughout the system. The focus on contaminant transport in a low pressure environment allows to simplify the model significantly as here the global flow field can be considered without perturbation by the contaminants. Thereby the computational cost as compared to the hybrid models given above is further reduced- the contaminant molecules are assumed to behave at equilibrium with the background-gas where the explicit simulation of particle representatives adds a thermodynamically consistent diffusion model to the athermal LB flow solver.

After further elaborating on aspects of this newly developed approach, contaminant transport aspects in terms of thermal velocity, diffusivity and advection diffusion problems are evaluated. Preliminary results of simulations performed in a model of an experimental setup are reported before the chapter closes with concluding remarks.

5.2 Modelling aspects

The model aims to simulate dilute contaminants in a homogeneous atmosphere. This situation arises when low pressurised gas flows are employed to flush systems of certain contaminants. The dilution is very important for the simplification of the model to hold. In particular for such cases it is possible to neglect the action of the contaminant on the atmospheric gas.

The LBM with intermediate Knudsen regime boundary corrections is employed to simulate the background gas. Single local contaminants are simulated as particles,

where the collision processes with the background gas are solved implicitly by performing a Monte Carlo algorithm where the equilibrium velocity is Galileian shifted to account for advection.

In effect, the simulation of the contaminant component can be understood as completely independent from the background gas model as long as a (quasi-)static velocity field and thermodynamic state are known. In the remainder we briefly revisit the modifications made to the LBM and give an overview of the Monte Carlo algorithm. Finally, the parameterisation is discussed in the context of an example thermodynamic configuration.

5.2.1 Lattice Boltzmann methods for intermediate Knudsen flow

As detailed in the introduction, for flows in systems either at very low pressure or of geometry on the nanometer scale the characteristic dimensionless number, the Knudsen number Kn becomes none negligible. The mean free path for gases under ambient pressure (1.013 bar) is in the order of a few tens of nm, for classical technical flow problems in geometries much larger than this effects associated with higher Knudsen numbers can therefore be neglected.

For $Kn > 0.01$ rarefaction effects gain noticeable influence on the flow characteristics and slip at the walls has to be taken into account [213]. This becomes relevant in the regime of only a few Pascal pressure considered here. Thus, to correct the lattice BGK (LBGK) Navier-Stokes solver for the discontinuous velocity field in the Knudsen layer, a slip boundary condition as proposed by Zhang *et al.* [230] has been implemented. Other suitable slip boundary conditions were proposed by amongst others Tao *et al.* [213], Ansumali and Karlin [231] and an extension of existing boundary conditions by Toschi and Succi introducing updated collision statistics by so-called virtual wall collisions [211].

In the remainder of this work, a two-step extension of the boundary condition by a diffusive reflection regime as well as a wall function modifying the effective mean free path is used as proposed by Zhang *et al.*. Following their formulation, the Knudsen number in a LBGK model is given by

$$Kn = \sqrt{\frac{8}{3\pi}} \frac{\tau - 0.5}{L}, \quad (5.1)$$

where L is the number of lattice sites used to resolve the characteristic length. From this it is immediately clear that the mean free path is here depending on the relaxation

time τ only. It is thereby linked to the fluid viscosity. The boundary conditions were implemented by David Sinz in the scope of his diploma thesis work at the University of Stuttgart [309].

A first employed boundary condition allows to control the reflective behaviour and thereby implicitly the slip by an accommodation parameter α defined between $\alpha = 0$ relating to no-slip or *bounce-back* and $\alpha = 2$ implementing full-slip or *specular reflection*. In the simulations described in the scope of this work, an accommodation parameter of $\alpha = 1$ is chosen. This corresponds to model diffuse deflection at a rough wall [230].

As with higher Kn and/or increase in resolution the Knudsen layer extends to scales resolved by the simulation, simple slip boundary conditions overestimate the velocity at the boundary. The reason for this is a significant reduction in the mean free path of particles in the vicinity of a surface, effectively lowering the local Knudsen number. Recently, several methods have been introduced to reflect this by the introduction of an effective mean free path λ_e . Integrations with the lattice Boltzmann method have been introduced by Tao *et al.*, Hyodo *et al.* and Zhang *et al.* [213–215].

Here the correction proposed by Zhang *et al.* is applied, formulating the effective mean free path

$$\lambda_e = \frac{\lambda}{1 + 0.7e^{-\Delta y/\lambda}}, \quad (5.2)$$

that contains a dependence on the distance from the nearest boundary node Δy . Using Eq. (5.1) and Eq. (5.2) the correction can be shown to correspond to a change in local kinematic viscosity, entering the model via a (now local) relaxation time parameter [215]

$$\tau = \sqrt{\frac{3\pi}{8}} \left[\frac{\lambda}{1 + 0.7e^{-\Delta y/\lambda}} \right] + 0.5. \quad (5.3)$$

5.2.2 A Monte Carlo Model for Contaminants

To describe a second component present in very low concentrations only, a method derived from the DSMC approach is employed. As a solver to the Boltzmann equation, this model relies as well on the principal independence of the free movement and collision processes of particles.

DSMC algorithms solve the Boltzmann equation in terms of free movement and collisions of particles representative of a thermodynamical state. Free movement is calculated straightforward at a given (thermal) velocity assigned to the particles. The distinction of the method lies in its approach to model particle collisions. After free flight for the duration of a given collision interval particles are binned and randomised collision partners in a bin volume are drawn. Each of these pairs is subsequently calculated to perform a momentum conserving collision assigning a new particle velocity. This coarse grained collision model increases simulation efficiency dramatically as integration of the particle movement to predict explicit collisions is not necessary. At the same time the method has been shown to produce thermodynamically accurate results, especially in the context of dilute systems with finite Knudsen numbers.

In the approach presented here, the observation of collision time intervals is replaced by collision time calculation from the mean free path travelled in the system. Taking into account only atmosphere-contaminant interactions, atmospheric collision partners are not drawn from representative particles in a volume but rather created as pseudo-particles parameterised by properties of the LB field in the vicinity of a contaminant particle.

An event driven algorithm focusing on collision events is implemented. Assuming local equilibrium, according to the mass m_ζ of contaminant species ζ and temperature T the individual particle velocity is drawn from a Maxwell distribution. From the mean particle velocity u_ζ , the time span δt to the next collision event is calculated as $\delta t = \lambda_\zeta / u_\zeta$, implicitly assuring the mean free path to be

$$\lambda_\zeta = \frac{1}{\pi\sigma_{\alpha\zeta}^2 n_\alpha} \sqrt{\frac{m_{\alpha\zeta}^*}{m_\zeta}}. \quad (5.4)$$

In this derivation, properties of atmospheric species α were used. The particle density per unit volume n_α is calculated for an ideal gas. The symbols $m_{\alpha\zeta}^* = (m_\alpha m_\zeta) / (m_\alpha + m_\zeta)$ designate the reduced mass and $\sigma_{\alpha\zeta}$ the effective collision radius, calculated as the arithmetic average of atomic radii approximated by Lennard-Jones potential parameters given by Karniadakis *et al.* [295].

At collision time the LBM lattice is used as binning grid. All contaminant particles present at a given lattice site undergo a collision with an ad hoc created *pseudo particle*, generated as a representative of the local atmospheric gas flow. In particular, the atmosphere gas particles are assigned a velocity u_α according to a Maxwell distribution whose mean value \bar{u} is shifted to reflect the velocity u_{LBM} of the lattice Boltzmann field. Per direction i this reads

$$u_{\alpha,i} = \sqrt{\frac{m_\alpha}{2\pi k_B T}} \exp \left\{ \frac{-m_\alpha (\bar{u}_i - u_{\text{LBM},i})^2}{2k_B T} \right\}. \quad (5.5)$$

Subsequent binary collisions between hard spheres are implemented classically, assum-

ing conserved velocity of the centre of mass and thus global momentum conservation, while updating the relative velocity of the collision partners [34]. The centre of mass velocity \mathbf{u}_m and the relative velocity \mathbf{u}_r of a contaminant particle ζ and a pseudo particle α are given by

$$\mathbf{u}_m = (\mathbf{u}_\zeta m_\zeta + \mathbf{u}_\alpha m_\alpha)(m_\zeta + m_\alpha)^{-1}, \quad (5.6)$$

and

$$\mathbf{u}_r = \mathbf{u}_\zeta - \mathbf{u}_\alpha, \quad (5.7)$$

respectively. With \mathbf{u}_m^* and \mathbf{u}_r^* denoting the post collision centre of mass and relative velocity respectively, kinetic energy and momentum is conserved in the collision by imposing $\mathbf{u}_m^* = \mathbf{u}_m$ and $|\mathbf{u}_r^*| = |\mathbf{u}_r|$. Since particles are assumed to be hard spheres all directions for \mathbf{u}_r^* are equally likely as scattering of hard spheres is isotropic. The post collision velocities of the particles can then be determined using a randomly chosen direction for the relative velocity considering $|\mathbf{u}_r^*| = |\mathbf{u}_r|$ and the post collision equivalents of Eq. (5.6) and (5.7). The updated contaminant velocity is employed for the calculation of the time interval δt elapsed until the next collision event. The information of the pseudo particle is discarded. This collision process serves both to couple the contaminant particles to the atmospheric flow and as a thermostat (see section 5.3.2).

In the scope of this work the respective lattice Boltzmann velocity field is pre-simulated until an equilibrium state is reached. There exists however no principle limitation on the synchronisation of the relaxation processes. Rather the quality of the modelling of dynamics in the style of DSMC is improved by taking into account the local time-dependent equilibrium determined by the LBGK algorithm. Analytical approximations of transport coefficients in this regime suggest e.g. that the mutual diffusivity can under these assumptions be expressed as a Lorentz-approximation (mass-ratio) corrected self-diffusivity coefficient of the atmosphere gas (see section 5.3.3).

Rarefaction effects are prominent in the Knudsen layer only. Thus special attention has to be paid to the boundary condition in the particle perspective as well. Since the main focus of the algorithm lies on true reproduction of the subscribed mean free path by timing collision events, the implementation of an accurate boundary condition is however straightforward. For the sake of simplicity again the lattice Boltzmann site decomposition is used to define the boundary geometry, introducing discretisation errors in systems with curved boundaries. For these cases the method may be improved by another choice of surface definition, e.g. using interpolation techniques [207, 310]. However, it has been shown that by resolving the Knudsen layer by as little as four lattice sites the error observed in the flow field can be limited to the order of 5 per cent. For a resolution of 8 lattice sites the deviation reduces to some per cent. As discussed above for a working model of flow in the intermediate Kn regime surface slip has to be taken into account as well as the reduction in phase space volume in

the vicinity of a boundary. Both requirements are met by a boundary condition reducing a particle's travelled distance if encountering a wall. The algorithm evaluates, whether during free movement a particle is travelling into a different LB node and subsequently whether it is a boundary node. If the particle would enter a boundary node, its position is reset to the point of contact, effectively reducing its travelled path. The subsequent collision event is modelled as diffusive reflection inverting the velocity component normal to the boundary surface. The thermal velocity is drawn from the half set with an inverted velocity component normal to the wall. This treatment is implicitly reducing the mean free path proportional to the surface to volume ratio in the system as well as reducing the phase space volume. The boundary condition is evaluated for a simple advection diffusion problem for which an analytical solution is available (see section 5.3.4).

In the first part of this section the proposed model is validated by comparison of simulation results with selected benchmark problems for which analytical solutions are available. The second part comprises application of the model to investigate contaminant transport in varying complex geometries for different flow situations.

5.2.3 Parameterisation

The validity of the LBM is chiefly limited by the underlying (thermo-) statistical principles and approximations in expansions. It is possible to define a LB specific Knudsen limit based on the idea that the local equilibrium approximation on a lattice site does not hold anymore. Another way of putting this is given with the low Mach number limit which requires the *transported* momentum density on the lattice to be low. This clarifies that all modifications made to capture the intermediate Knudsen regime can only be phenomenological. As the evaluation of channel flow in the low Knudsen regime illustrates, modified continuum models can be suited to simulate flows in this regime. Nonetheless, when working with the modification of choice, leaving the core algorithm unmodified, the original restrictions have of course still to be observed.

In order to be able to understand the units captured by the model, a conversion of the core units is instructive. The scaling units of length, time and mass are typically calculated by use of the constant speed of sound on the lattice as well as the kinematic shear viscosity imposed by the collision scheme. When aiming to model real systems, the usual choice of unit mass might be dismissed to calibrate the system in order to preserve numerical stability in cases where realistic pressures otherwise lead to very high densities or in cases where the relaxation rates are getting very low.

In the cases employed here, starting out from length-scaling the lattice to match a

physical system, length and time scales are fixed by comparing the speed of sound in the desired physical system with the one on the lattice. Keeping the lattice mass at unity, the overall mass scaling is then determined by comparison of the resulting dynamic shear viscosity with the one of the desired physical system.

A typical approach to the parameterisation of a simulation system is made by deciding on the spatial resolution of a system, determining the lattice spacing Δx . Together with the lattice discretisation and the thereby determined speed of sound c_s , this immediately fixes the time step $\Delta t = \Delta x/c_s$ and the conversion units for the kinematic viscosity ν . For the case of a single fluid adhering to the ideal gas law Eq. (2.38) for the relation of pressure and fluid density, the consideration of the thermodynamic state and modelled substance, i.e. temperature, mass and pressure fixes a mass scale Δm . Conversion of the dynamic viscosity η then allows to determine the relaxation time or shear viscosity relaxation parameter τ or λ_ν via Eq. (2.37). Here, some tuning flexibility is given by the mass scaling, allowing to adjust the simulated mean fluid density against the relaxation time parameter. Table 5.1 gives some example numbers for arbitrary length scaling and Hydrogen at room temperature and 4 Pascal pressure obtained from the NIST chemistry webbook [311].

Property	Formulation	Physical example
Length scale Δx	$\Delta x = \chi^{\text{phys}}/\chi^{\text{LB}}$	1 m/1000 l.u. = $1.0 \cdot 10^{-3}$ m
Time scale Δt	$\Delta t = c_s^{\text{LB}}/c_s^{\text{phys}} \cdot \Delta x$	$\Delta x/\sqrt{3}/1280 \frac{\text{m}}{\text{s}} = 4.5105 \cdot 10^{-7}$ s
Mass scale Δm	$\Delta m = (\Delta x^3 \cdot \rho^{\text{phys}})/\rho^{\text{LB}}$	$(\Delta x^3 \cdot 2.445 \cdot 10^{-6} \frac{\text{kg}}{\text{m}^3})/0.1 \text{ l.u.} = 2.445 \cdot 10^{-14}$ kg
Kinem. viscosity ν	$\nu^{\text{LB}} = \nu^{\text{phys}}/\frac{\Delta x}{\Delta t^2}$	$3.581 \frac{\text{m}}{\text{s}^2}/\frac{\Delta x}{\Delta t^2} = 1.6152$

Table 5.1: *Example numbers for arbitrary length scaling and Hydrogen at room temperature and 4 Pascal pressure obtained from the NIST chemistry webbook [311].*

5.3 Validation

This section starts out with the re-evaluation of the implementation of the intermediate Kn corrected LBM boundary conditions as described by Zhang *et al.* [215,230]. Comparison is made to results of the linearized Boltzmann equations in a narrow channel published by Ohwada *et al.* [312,313]. Non-dimensionalised values are compared. In a second part the thermal properties of the particle model as well as the coupling algorithm are tested. Throughout evaluations of the hybrid model SI units are used as they have been employed explicitly in the implementation of the particle model. Here, we compare the simulation velocity distribution to the respective

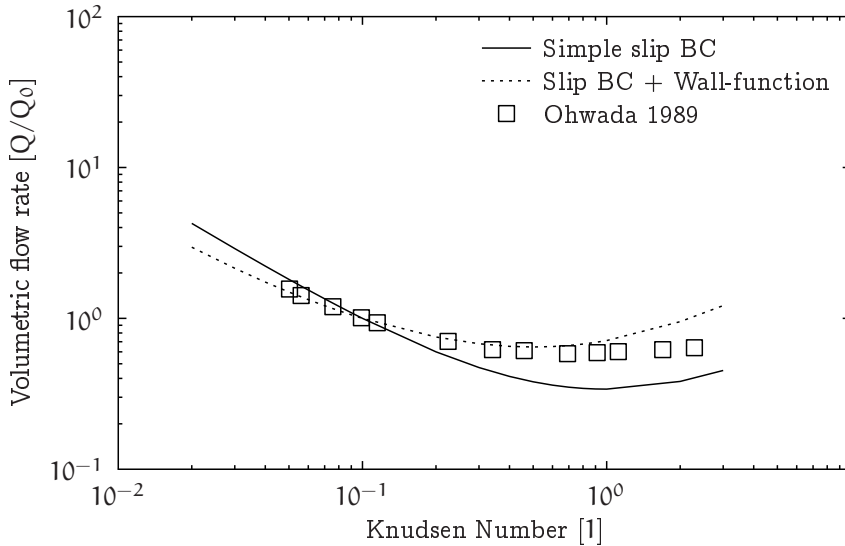


Figure 5.1: Volumetric flow rate through a simple channel as a function of the Knudsen number, normalised by the flow rate measured at $Kn=0.1$. Reproduction of a validation published by Zhang et al. [215]. The simulation results are obtained in a channel of 32 lattice units width. A finite slip boundary condition was employed both alone and with a viscosity correction accounting for a varying mean free path in the vicinity of a boundary [215, 230]. The reference values (symbols) are results of an exact solution to the linearized Boltzmann equation for hard spheres by Ohwada et al. [312, 313]. Using the combined boundary conditions good agreement can be obtained for the lower intermediate regime of $Kn \approx 0.05..0.5$.

Maxwell distribution both for the pseudo- and contaminant-particles over a range of temperatures. Third, the diffusive behaviour of the model is checked. By focusing on a simple quasi-1D diffusion problem we ensure the validity of our choice of both mean free path λ and diffusivity D . Finally the lattice Boltzmann velocity field, the coupling and the diffusivity model are integrated with our contaminant boundary condition. Our results are compared to a solution of the transport equation in one dimension.

5.3.1 Intermediate Knudsen numbers - The LBM implementation

In order to assure the accuracy of the implementation of the boundary corrections by Zhang *et al.*, flow at prescribed Knudsen numbers in a simple channel is simulated. Evaluations are made both for slip boundary conditions only, as introduced in [230], and for combinations of a slip boundary condition and a viscosity correction to account for a locally varying Knudsen number at the boundary [215, 309]. Simulations are executed in a pseudo-1d channel of a size of $1 \times 1 \times 32$ lattice units allowing for good numerical efficiency. The flow is driven by a body force of $F = 1 \cdot 10^{-7}$ in lattice units. To assure to reach a steady state simulations are in all cases run for 100,000 time steps.

The flow profiles of the original publication are reproduced, reaching satisfactory agreement of simulated flow profiles and analytical solution to the linearized Boltzmann equation for hard spheres by Ohwada *et al.* [312, 313]. As depicted in figure 5.1 the combined boundary corrections allow to recover the theoretical flow rates within a few percent even up to low single digit Kn. The shown flow rate has been normalised by the respective flow rate assumed at $\text{Kn}=0.1$. Furthermore the Knudsen-Paradox is captured by the model. The minimum flow rate measured in the simulations is reached around $\text{Kn} \approx 0.5$ in good agreement with the results of the analytical calculations as well as other numerical results reported by Toschi [211] and Cercignani [314]. These measurements allow for confidence in the capability of the extended lattice Boltzmann model to capture fluid behaviour in the intermediate regime.

5.3.2 The Maxwell speed distribution - The coupling algorithm

To evaluate the coupling approach described in section 5.2.2 and ensure sound thermostatic behaviour of the contaminant particles, the particle velocity statistics per collision event for a range of temperatures are measured. Parameters kept fixed are the ambient pressure $p = 3 \text{ Pa}$, a contaminant mass of $m_\zeta = 100 \text{ au}$ and an atmosphere particle mass of $m_\alpha = 2 \text{ au}$. Figure 5.2 documents the exact agreement between the simulation velocity field and the theoretical solution

$$f(\mathbf{u}) = 4\pi u^2 \left(\frac{m}{2\pi k_B T} \right)^{3/2} \exp \left\{ -\frac{m u^2}{2k_B T} \right\}. \quad (5.8)$$

This result suggests correct thermalization of the *pseudo-particle's* velocity components as well as functionality of the collision algorithm, serving in addition to the coupling as a thermostat to the contaminants.

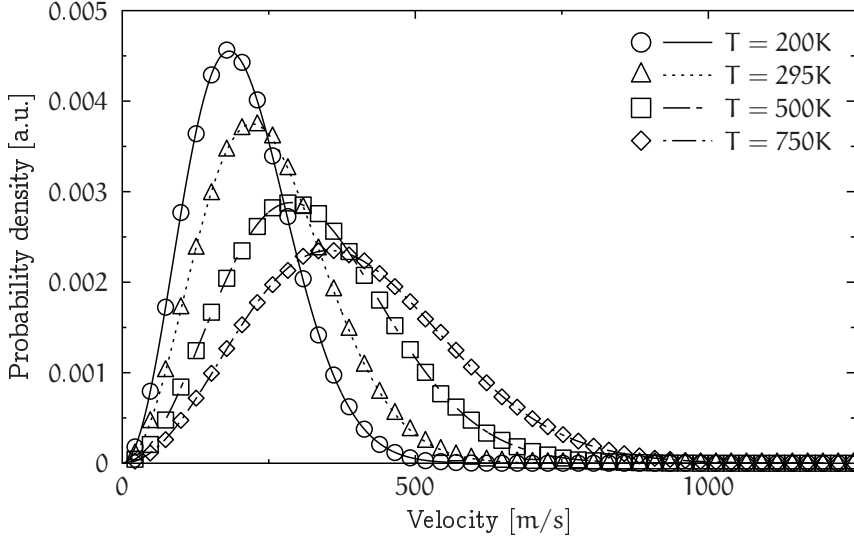


Figure 5.2: Probability density of contaminant particle velocity for different system temperatures. Theoretical values are given by the Maxwell speed distribution for particles of a mass of 100 au at the respective temperature (Eq. 5.8). We find exact agreement with the theory, verifying the correct operation of the coupling algorithm (Sec. 5.2.2).

5.3.3 The second law of Fick - Diffusion in a binary mixture with large density contrast

As detailed above, a main focus of application of the proposed model is the efficient simulation of diffusive transport in low pressure environments. The validity of the event driven algorithm, parameterised by the mean free path λ is tested by comparison of the measured resulting diffusivity. The second law of Fick

$$\frac{\partial}{\partial t} n_{\zeta}(x) = D_{\alpha\zeta} \nabla^2 n_{\zeta} \quad (5.9)$$

defines the contaminant-atmosphere diffusivity $D_{\alpha\zeta}$ in term of the second spatial and first time derivative of a concentration or density field. A solution in one dimension gives the particle density $n_{\zeta}(x, t)$ at a locus x different from the initial position x_0 and time t in terms of the absolute particle number N_{ζ} and $D_{\alpha\zeta}$ as

$$n_{\zeta}(x, t) = \frac{N_{\zeta}}{\sqrt{4\pi D_{\alpha\zeta} t}} \exp \left\{ -\frac{(x - x_0)^2}{4D_{\alpha\zeta} t} \right\}. \quad (5.10)$$

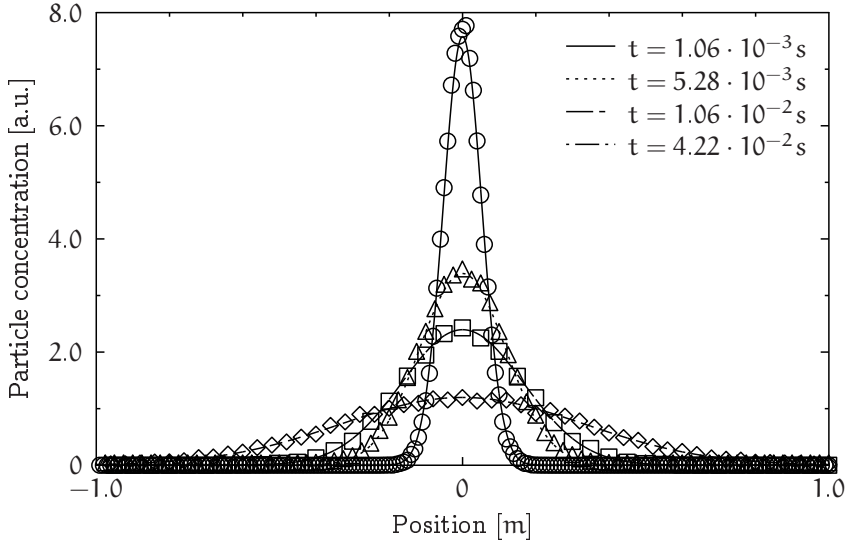


Figure 5.3: *Particle density distribution at different times. All particles have been initialised in the point of origin. We find quantitative agreement with the theory (Fick's second law, Eq. 5.10) over a wide range of parameters. Here depicted is an example configuration; a system comprised of a Hydrogen atmosphere at $p = 3 \text{ Pa}$ and $T = 295 \text{ K}$ containing contaminants of mass $m_\zeta = 100 \text{ au}$. The diffusivity is calculated according to Eqs. 5.11, 5.12 to $D_{\alpha\zeta} \approx 1.31 \cdot 10^{-2} \text{ m}^2/\text{s}$.*

Figure 5.3 illustrates the dynamics of the particle density field of a system comprised of a Hydrogen atmosphere at $p = 3 \text{ Pa}$ and $T = 295 \text{ K}$ containing contaminants of mass $m_\zeta = 100 \text{ au}$. For the presented results, 1 million particles are initially placed at the origin. Using a mass corrected diffusivity

$$D_{\alpha\zeta} = c_m \frac{3}{8\sigma_{\alpha\zeta}^2 n_\alpha} \sqrt{\frac{k_B T}{2\pi m_{\alpha\zeta}^*}}, \quad (5.11)$$

with a mass correction factor

$$c_m = \frac{2m_\alpha + 4m_\zeta}{3(m_\alpha + m_\zeta)}, \quad (5.12)$$

excellent quantitative agreement of simulation and theoretical predictions is found. The correction factor given by Eq. 5.12 has allowed quantitative predictions for the diffusivity over a wide range of atmosphere/contaminant mass contrasts. It can be motivated by the non-trivial expectation values of momentum transfer at large mass contrasts. Even for simplified models of hard spheres, the asymmetry in momentum carried by species of different mass, travelling at different respective thermal speeds,

requires higher order mass corrections. For a more in-depth discussion and example calculations see the book of Chapman and Cowling [9]. The form of mass correction reported here is again depending on the simplifying assumptions limiting interaction to atmosphere-contaminant collisions. For a mass contrast of one \mathcal{C}_m reduces to unity.

5.3.4 The transport equation - The particle boundary condition

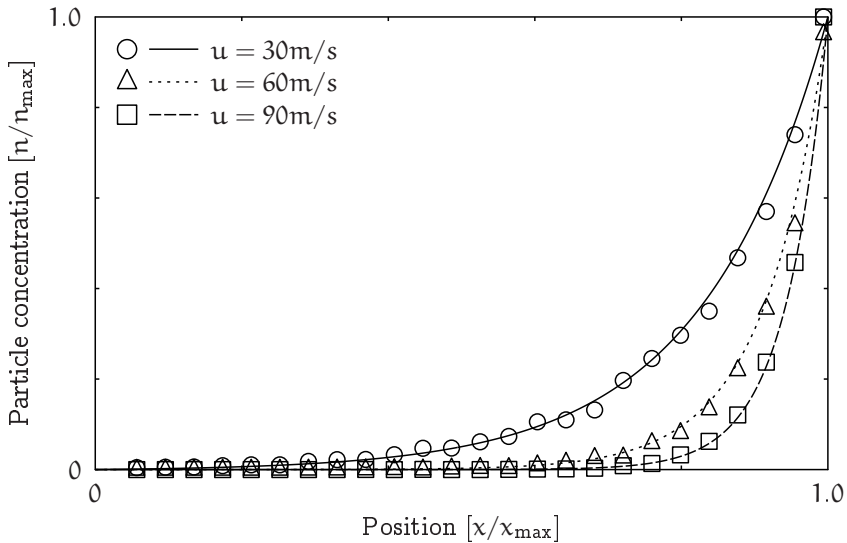


Figure 5.4: *Equilibrium particle density distribution in systems combining constant flow in positive x -direction and a diffusivity of $D_{\alpha\zeta} \approx 1.31 \cdot 10^{-2} \text{m}^2/\text{s}$. At $x/x_{\text{max}} = 1$ the system is delimited by a boundary acting on the contaminants (see section 5.2.2). The curves are given by the solution Eq. 5.15 to the transport equation assuming an infinite particle reservoir at $x > 1$ and an open boundary at $x < 0$. The simulation particle densities are re-normalised to the density measured 5 lattice sites in front of the wall. Outside of the boundary layer we find the differential equation 5.13 excellently approximated. The fluctuating densities due to thermalised reflection at the wall do however not justify the infinite reservoir assumption of the theory. This results in strong variation of the obtained result.*

In this final evaluation of the model, the stationary state of a system described by the transport equation

$$\frac{\partial}{\partial t} n_{\zeta}(\mathbf{x}) = -D_{\alpha\zeta} \nabla^2 n_{\zeta} + \mathbf{u}_{\alpha}(\mathbf{x}) \nabla n_{\zeta} = 0 \quad (5.13)$$

is considered. Assuming the boundary conditions

$$n_{\zeta}(0) = 0 ; \quad n_{\zeta}(x/x_{\max} = 1) = 1, \quad (5.14)$$

the particle number density is normalised by a maximum value assumed at $x = 1$. This situation is describing a system with a constant flow velocity in positive x -direction and an infinite particle reservoir at $x > 1$ as well as an open boundary at $x < 0$. The infinite particle reservoir is here modelled by a boundary visible for the contaminant particles only. As before for the example system parameterisation a Hydrogen atmosphere at $p = 3$ Pa and $T = 295$ K containing contaminants of mass $m_{\zeta} = 100$ au is selected. This corresponds to a diffusivity of $D_{\alpha\zeta} \approx 1.31 \cdot 10^{-2} \text{m}^2/\text{s}$. Figure 5.4 depicts the normalised particle density over the normalised x -coordinate. Solid lines represent solutions to equation 5.13, given by

$$n_{\zeta}(x) = \left(\exp \left\{ x \frac{u}{D_{\alpha\zeta}} \right\} - 1 \right) \left(\exp \left\{ \frac{u}{D_{\alpha\zeta}} \right\} - 1 \right)^{-1}. \quad (5.15)$$

It is found that in order to agree with the theory an area of five lattice sites in front of the wall has to be neglected. In the immediate vicinity of the wall the local density is fluctuating strongly, introducing large deviations to the normalisation and thus the measurements. Omitting 5 lattice sites however, the model is quantitatively reproducing the theoretically expected behaviour, verifying the correct interplay of now coupled advection and diffusion. This correction is necessary as the system and theoretical model deviate - a thermal wall is not an infinite reservoir.

5.4 Simulation of contaminant suppression by bezels

The model is applied to a setup where contaminant suppression by low speed flows through different openings at low pressure is measured. The simulations have been performed in a two-step process. First, a solution to the flow of the background gas was obtained by means of an adjusted LBM. Contaminants were subsequently simulated coupled to the quasi-static solution. In this part the LB parameterisation outlined in the preceding section 5.2.3 is employed.

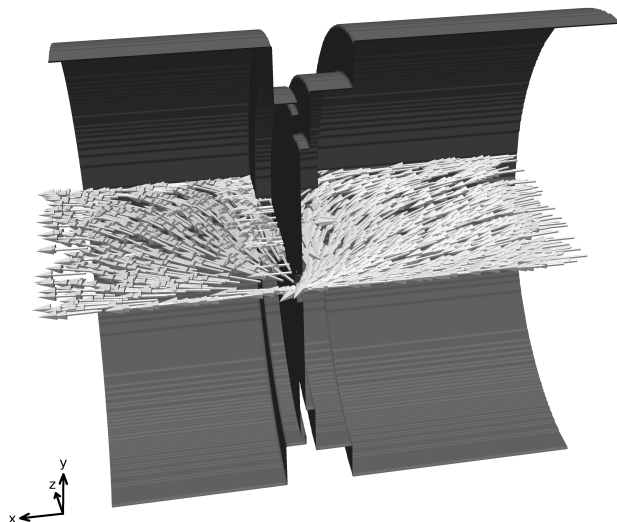


Figure 5.5: *Illustration of the flow path through the system. The velocities are not to scale. In the centre opening, the velocity is up to three orders of magnitude larger than in the remainder of the system.*

5.4.1 System setup

Figure 5.5 shows a ray-traced image of the simulation geometry used. The cylindrical shape of the chamber is reflecting an experimental setup. The system is resolved by $256 \times 256 \times 256 \text{ mm}^3$, where in the centre-plate a round opening with a diameter of 14 mm is placed.

The system geometry has been adapted from a typical experimental measurement setup. Here variable openings are introduced into the centre of a system with adjustable absolute pressure as well as relative pressure gradient. Flow rates controlled by the pressure gradient are verified by additional flow measurement in the in- and outlets. Contaminants are injected on one side, whereas their partial pressure is measured on both chambers. The simulation parameterisation is operating in a regime close to experimental description, where exactly comparable results of experiment and simulation have yet to be obtained.

Single component fluid flow is parameterised by choice of mean lattice density $\rho = 0.1$ l.u. and a relaxation time of $\tau = 5.3457$. At the given discretisation the viscosity wall-function (5.3) is found to have a non-zero value over 5 lattice sites. Full refractive boundary conditions are employed in the immediate vicinity of the bezel opening

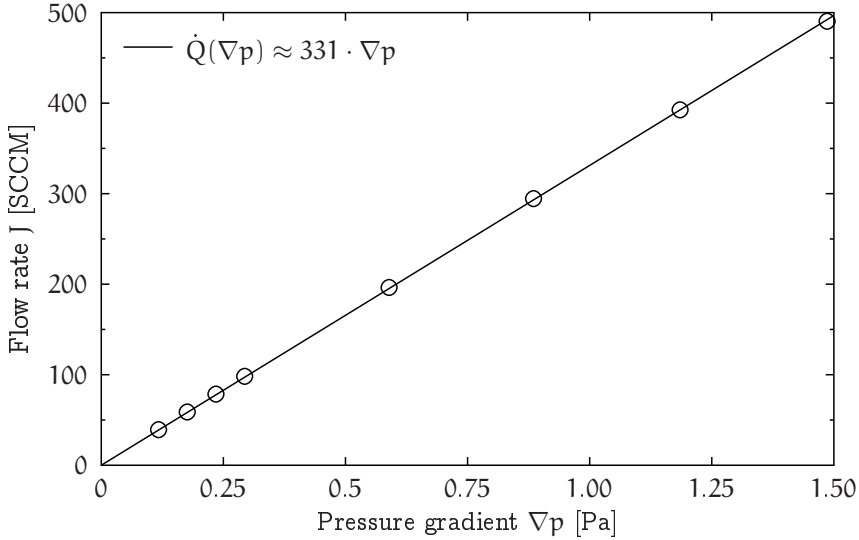


Figure 5.6: Gas flow rate as a function of the pressure gradient. The LB simulation has been parameterised to the kinematic viscosity $\nu = 3.581 \frac{m^2}{s}$ and speed of sound $c_s = 1280 \frac{m}{s}$ of Hydrogen gas at a mean pressure of $p = 4$ Pa and temperature $T = 295$ K. A clear linear dependence of the flow rate \dot{Q} on the pressure gradient is found even at very high flow speeds violating the low Mach number assumption ($Ma \approx 0.27$).

only. This has been established to enhance the stability of the LB in regimes of higher pressure gradients. This is justified as, while introducing an error in the exact form of the flow field throughout the system, flow rates in the central opening are not affected by this measure.

The flow is driven by Zou-He type boundary conditions, establishing a flow rate by a Neumann condition on the influx at $x = 0$ against a fixed pressure Dirichlet condition at $x = n_x = 256$. A snapshot illustration of the resulting flow field is depicted in figure 5.5. It is noteworthy that the flow rate in the region of the opening is up to three orders of magnitude higher than in the rest of the system, where vectors have been scaled equally to illustrate the flow path rather than the scales.

In figure 5.6 atmosphere gas flow rates are plotted over the applied pressure gradients. The LB simulation has been parameterised to the kinematic viscosity $\nu = 3.581 \frac{m^2}{s}$ and speed of sound $c_s = 1280 \frac{m}{s}$ of Hydrogen gas at a mean pressure of $p = 4$ Pa and temperature $T = 295$ K [311]. The mean free path of hydrogen in this setup

is calculated from tabulated data of the collisional cross section and mass to be $\lambda_{\alpha}^0 \approx 2.70 \cdot 10^{-3} \text{ m}$, implying a Knudsen number of $\text{Kn} \approx 0.2$ using the opening diameter as limiting length scale.

A clear linear dependence of the flow rate \dot{Q} as measured in the volume of the opening on the pressure gradient is found. Even though in the simulations exceeding a pressure gradient of 1 Pa, the low Mach number limitation is clear violated (at the highest value the Mach number in the peak flow is $\text{Ma} \approx 0.27$), the functional dependence holds surprisingly well. The LB simulations are run for 300,000 time steps after which the change in the field per time step is in the order of 10^{-7} and below.

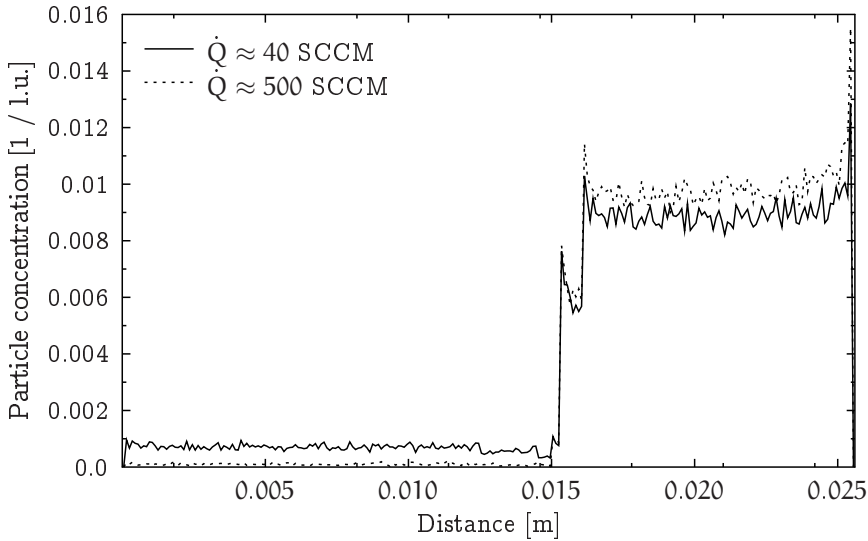


Figure 5.7: *Snapshot of simulation data at the lowest and highest flow rates, respectively 100,000 collision events into the simulation where a total of 10,000,000 collision events was simulated. The data is a histogram of the amount of particles present in the respective lattice layer volume. The total number of particles was 100,000. The suppression coefficient is calculated from fitting a constant function to these data in the ranges $x \in \{0.0050..0.0100\} \text{ m}$ and $x \in \{0.0175..0.0225\} \text{ m}$. The step deviations in the central region reflect that the data is not normalised for the variation in local volume in the geometry. In particular, the opening in the region $x \in \{0.015..0.0152\} \text{ m}$ is clearly visible as minimum. For the calculation of the suppression coefficient by Eq. (5.16) particle numbers left and right of the opening are simply summed.*

5.4.2 Contaminant suppression

The contaminant particles are initialised in the upstream chamber in the range of $x = 0.0153$ m to $x = 0.0256$ m. Each particle receives random spatial coordinates outside of the obstacle volume, as well as Maxwell-Boltzmann distributed random velocity components for a temperature of $T = 295$ K and particle mass of 100au. The effective cross section is estimated from tabular values for Hydrogen and Heptane (as an example of a heavy organic molecule of a weight of 100 a.u.) to be [295]

$$\sigma_{\alpha\zeta} \approx \frac{1}{2} (2.915 \cdot 10^{-10} + 6.663 \cdot 10^{-10}) \text{ m} = 4.789 \cdot 10^{-10} \text{ m},$$

suggesting with equation (5.4) a mean free path of the contaminant of approximately $\lambda_{\zeta}^0 \approx 1.98 \cdot 10^{-4}$ m. Using the bezel opening diameter as typical scale, the obtained Knudsen number is $\text{Kn} \approx 0.014$.

The contaminant dynamics are evaluated from concentration histograms of the system in the Cartesian coordinates. Figure 5.7 illustrates these data in the main flow direction for the minimum and maximum flow rates employed ($\dot{Q} \approx 40$ SCCM and $\dot{Q} \approx 500$ SCCM, respectively) after 100,000 of 10,000,000 collision events. The difference in the system dynamics is already at this early stage distinctly visible. The concentrations χ^+ and χ^- used to determine the suppression coefficient as

$$s = \frac{\chi^+}{\chi^-} \quad (5.16)$$

are measured by fitting a constant in regions of undisturbed concentrations in the ranges $x \in \{0.0050..0.0100\}$ m for the downstream and $x \in \{0.0175..0.0225\}$ m for the upstream chamber. The deviations in the concentrations in the central region reflect that the data is not normalised for the variation in local volume in the geometry. In particular, the opening in the region $x \in \{0.0150..0.0152\}$ m is clearly visible as minimum.

The suppression coefficients obtained for the various flow rates are presented in figure 5.7. In agreement with findings involving an earlier model, an exponential dependence of the suppression on the flow rate is found [309].

This test case illustrates qualitative agreement of the hybrid model with preliminary reports on experiments, where the initial validations are able to document quantitative reproduction of thermostatic predictions. Quantitative comparison with experimental data is a natural next step.

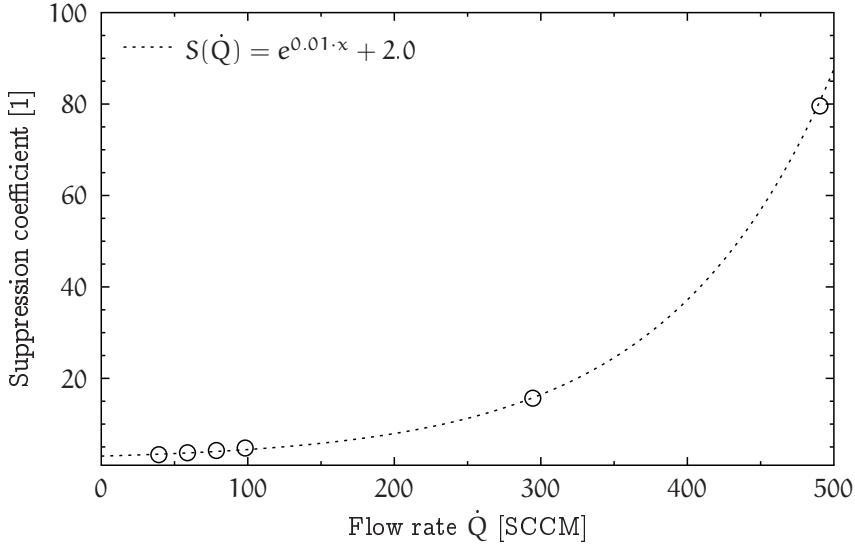


Figure 5.8: Measured suppression coefficients over varying flow rate through the opening. The suppression behaviour of the system can be approximated by an exponential relation to the flow rate observed in the system.

5.5 Conclusion and Outlook

Motivated by industrial applications requiring contaminant suppression in low vacuum environments, a hybrid simulation model has been refined and validated. Starting from original work performed by David Sinz on a phenomenological model, a Monte Carlo algorithm to introduce a diffusivity model to a LBM setup has been redeveloped and improved in thermostatic context.

The original problem concerned an ideal gas flushing a system pressurised in the single digit Pascal range, where medium sized aromatic contaminants are present in the system. The sparsity of the contaminant molecules allows complete neglect of their impact on the gas flow. As a result it is necessary to couple the solution of the gas flow into the simulation of the contaminants only.

This important simplification allows efficient calculation of the diffusive transport (The contaminant simulations are executed as a single process and finish in a matter of hours). By only requiring a quasi static solution to the flow field, the Monte Carlo

portion of the model is furthermore independent of the choice of flow solver used to obtain said solutions.

With the intermediate goal of simulating and predicting flow on scales relevant to engineering, the LBM has been selected due to its adaptability to complex geometries. While the method is not readily applicable to intermediate Knudsen flow regimes, phenomenological corrections can be introduced to recover the flow behaviour observed in rarefied systems with sufficient accuracy.

The Monte Carlo model is distinguished by combination of two central ideas. First, the coupling of a local advective velocity by shift of the expectation values of the Gaussian thermal velocity distributions constituting the local Maxwellian. Second the parameterisation of a collision event-driven algorithm determining time scales by the mean free path and equilibrium velocities.

The resulting algorithm has been validated to recover correct thermal velocity distributions as well as superposed advective velocities. Since the coupling algorithm implicitly acts as a thermostat, the Maxwell-Boltzmann distribution of particle velocities is assured at all times.

Using collision properties of hard spheres with an additional mass contrast correction, quantitative prediction of the diffusivity of the contaminants for a given thermodynamical state and particle mass has been successful. The mass correction term found here may be of practical relevance to more than this application as it illustrates and quantifies the relevance of mass contrasts in momentum transfer and resulting diffusivity.

A more complex test case combines an effective advection-diffusion, or transport model with a test of the boundary conditions. It has to be refrained from developing a quantitative solution to the particle distribution in the boundary layer. Quantitative agreement with the approximation of an infinite fixed concentration source could however be obtained when a density integrated over the boundary layer was used.

In a final step the developed combined method has been applied to suppression of contaminant diffusive transport by gas flows through an opening in the low intermediate Knudsen regime. Qualitative evaluation of gas flow rate and resulting suppression has yielded promising results. As expected exists a well defined linear dependence of the flow rate on the applied pressure gradient. Furthermore is the resulting suppression an exponential function of the flow rate.

Further development and application of the model can be envisioned in both experimental as well as theoretical context. True to the original motivation of the work a

natural next step is the comparison with experimental results. To this end, this work provides a parameterisation framework both of the LBM and the Monte Carlo algorithm where input can be provided in SI units. While some limitations such as the low Mach number limit and the principal continuity assumption apply, the method is able to cover a wide range of technically relevant scales.

Theoretical extensions of the model can be made by means of refining the algorithm to increase its overall accuracy. A very obvious flaw of the current model living on the LBM lattice is the very limited resolution of boundary shapes. Also the coupling to models capable of providing exact solutions to the Knudsen layer flow to some problems could be very interesting. Also extension of the collision model to include soft potentials, etc. is of interest.

Chapter 6

Summary and outlook

This thesis reports work conducted on different aspects of multiphase flow simulation methods on the mesoscopic scale. The focus is here on optimisations and simplification of the principal problems in order to be able to apply the methods to address engineering applications. The volume of problems and methods even in this rather special field must prevent any contribution from being comprehensive. The reported results have rather to be understood as reporting different aspects of ongoing work on development and application of simulation in the field.

Starting out from a historical view of fluid dynamics research, the different aspects of classical fluid dynamics and kinetic theory are discussed. In addition to the central equations of motion, dimensionless numbers are defined and discussed as essential tools to classify fluid system properties. Central are here the dominantly low Reynolds number, the low Mach number requirement of the LBM and finite Knudsen numbers in the transition from continuum to particle approximations.

Motivated by developments in fabrication technology and engineering applications on the micro- and nano-scale, theoretical models to capture complex boundary conditions for functional surfaces are being developed. Chapter 3 reports the results of simulations conducted to verify the predictions of a simplified theory for patterned surfaces. The model in question is concerned with the description of anisotropically patterned surfaces by means of a variable slip length condition. Starting from the most simple anisotropic case of stripes, with cosine varying slip and aspects of the model extension to the description of AFM measurements, development of the method towards application in engineering production are laid out.

Understanding the theoretical model as involving a phenomenological boundary con-

dition, the comparison of the simulation data obtained in the context of a model of an AFM as an actual measurement device will allow to determine the scope of applicability of the model. While earlier research has already found that deformations of the interface cannot be neglected in general, it may well be possible to identify rules formulate effective boundary parameters nonetheless.

Different from the implicit description of multiple system components and aggregate phases by adjustment of the boundary condition of a single phase, chapter 4 is involved with explicit modelling of multiple fluid components. Motivated by application in enhanced oil recovery, but applicable to a much wider range of problems, a pseudo-potential multi-component LB model including a surfactant species is integrated with a multi relaxation time collision scheme. The resulting new algorithm is evaluated to preserve properties that have been used in a LBGK context. Surface tension, wettability and diffusivity have been considered. In addition a significant reduction in error of permeability calculations of fluids of higher viscosity in low resolved channels has been verified. Necessary re-implementation of the interaction algorithm has been identified as a means to further optimise the method. In a basic parameter study the new implementation has been employed with the simulation of forced imbibition in a random 2d porous medium, building confidence for research of diffusivity effects and relative permeability in more demanding 3d systems.

Here, the investigation and further optimisation of different model aspects can be taken into account. Revisiting the parameter space of the surfactant model more in depth, e.g. by comparing to experimental results, may enable quantitative comparison of system behaviour. This extends to the integration of specific coupling between the surfactant species and the solid boundaries as well. Besides further aiding precision and stability of the model, adjustment of the forcing strategy may also be used to develop a better understanding of precursor formation and diffusive effects on the pore- and network scale. By this, effective explicit simulation of the parameter space determining relative permeability in ternary mixtures could be enabled.

Considering a different type of multi component system, chapter 5 lays focus on flow on the fringes of validity of fluid continuum descriptions. Contaminant transport in low vacuum systems is of interest e.g. when dealing with so-called hazing of lenses in lithographic optics systems. The presence of a very sparse contaminant component allows for significant simplification of the model. The large contrast in masses between the flushing gas and contaminants required however intensive work in order to identify a valid mass correction in the diffusivity terms. An event driven Monte Carlo algorithm is coupled to an advective field by means of a shift in the expectation value of the local Maxwellian components. The mean free path is a central parameter in this model. Great attention has been paid on the development of a parameter framework allowing to adjust the model in terms of physical units. After verifying quantitative agreement with thermostatic predictions of particle

velocities and diffusivity, first qualitative tests of modelling suppression in a complex geometry at technical relevant scales are reported.

In addition to comparison with experiments on the technological relevant scales, theoretical extension of the model promises to be interesting. The integration of more precise boundary conditions as well as a straightforward change in the coupled advection model could allow for comparison with exact predictions at even higher Knudsen numbers. Alteration of the collision algorithm can allow to account for particle deformability and even reactivity. Verification of the applicability of the model can enable simulations to aid future system design.

In particular on the mesoscopic scale, coarse grained computer simulation models are developing quickly towards tools capable of aiding design and understanding of real fluid systems. Besides the ever growing computational power available, a key ingredient to this development is a deeper understanding of fluid dynamics, as it allows to manage complexity and enable more efficient use of calculations. While dealing with a subset, this work has touched all aspects of optimisation, increasing complexity to gain accuracy and stability at points, while radically simplifying system aspects not relevant to the parameters of interest in others. While work in this scope is unlikely to reach an *end*, it is hoped that the presented results tell somewhat enough to begin with.

Bibliography

- [1] R. W. Johnson. *Handbook of Fluid Dynamics*. CRC Press, 1998.
- [2] M. Born and H. S. Green. A General Kinetic Theory of Liquids. I. The Molecular Distribution Functions. *Proceedings of the Royal Society of London A*, 188(1012):10–18, 1946.
- [3] N. N. Bogoliubov. Kinetic Equations. *Journal of Physics*, 10(3):265–274, 1946.
- [4] J. Yvon. *La théorie statistique des fluides et l'équation d'état*. Hermann & Cie, Paris, 1935.
- [5] J. G. Kirkwood. The Statistical Mechanical Theory of Transport Processes I. General Theory. *The Journal of Chemical Physics*, 14(3):180–201, 1946.
- [6] W. R. Hamilton. On a General Method in Dynamics; By Which the Study of the Motions of All Free Systems of Attracting or Repelling Points is Reduced to the Search and Differentiation of One Central Relation, or Characteristic Function. *Philosophical Transactions of the Royal Society of London*, 124:247–308, 1834.
- [7] C. L. M. H. Navier. *Résumé des leçons données sur l'application de la mécanique*. Carilian, 1838.
- [8] G. G. Stokes. On the theories of the internal friction of fluids in motion, and of the equilibrium and motion of elastic solids. *Math. Phys. Papers. by G. G. Stokes Transactions of Cambridge University Press, Cambridge Phil. (reprint)*, 3:287, 1845.
- [9] S. Chapman and T. G. Cowling. *The Mathematical Theory of Non-uniform Gases: An Account of the Kinetic Theory of Viscosity, Thermal Conduction and Diffusion in Gases*. Cambridge University Press, 1970.
- [10] M. Knudsen. Die Gesetze der Molekularströmung und der inneren Reibungsströmung der Gase durch Röhren. *Annalen der Physik*, 333(1):75–130, 1909.

- [11] M. Knudsen. Eine Revision der Gleichgewichtsbedingung der Gase. Thermische Molekularströmung. *Annalen der Physik*, 336(1):205–229, 1909.
- [12] H. Grad. On the kinetic theory of rarefied gases. *Communications on Pure and Applied Mathematics*, 2(4):331–407, 1949.
- [13] G. Karniadakis, A. Beskok, and N. Aluru. *Microflows and Nanoflows: Fundamentals and Simulation*. Springer Science & Business Media, 2006.
- [14] J. T. Davies. *Turbulence Phenomena: An Introduction to the Eddy Transfer of Momentum, Mass, and Heat, Particularly at Interfaces*. Elsevier, 2012.
- [15] C. E. Brennen. *Fundamentals of Multiphase Flow*. Cambridge University Press, 2005.
- [16] C. L. Fefferman. The Millenium Challenge - The Navier-Stokes Equation, 2000. <http://www.claymath.org/sites/default/files/NavierStokes.pdf>.
- [17] D. Burnett. The Distribution of Velocities in a Slightly Non-Uniform Gas. *Proceedings of the London Mathematical Society*, 39(1):385–430, 1935.
- [18] D. Burnett. The Distribution of Molecular Velocities and the Mean Motion in a Non-Uniform Gas. *Proceedings of the London Mathematical Society*, s2-40(1):382–435, 1936.
- [19] O. I. Vinogradova. Slippage of water over hydrophobic surfaces. *International Journal of Mineral Processing*, 56:31–60, 1999.
- [20] E. Lauga, M. P. Brenner, and H. A. Stone. *Handbook of Experimental Fluid Dynamics*. Springer, NY, 2007.
- [21] P. Lallemand, L.-S. Luo, and Y. Peng. A lattice Boltzmann front-tracking method for interface dynamics with surface tension in two dimensions. *Journal of Computational Physics*, 226(2):1367–1384, 2007.
- [22] G. Thömmes, J. Becker, M. Junk, A. K. Vaikuntam, D. Kehrwald, A. Klar, K. Steiner, and A. Wiegmann. A lattice Boltzmann method for immiscible multiphase flow simulations using the level set method. *Journal of Computational Physics*, 228(4):1139–1156, 2009.
- [23] D. R. Noble and J. R. Torczynski. A Lattice-Boltzmann Method for Partially Saturated Computational Cells. *International Journal of Modern Physics C*, 09(08):1189–1201, 1998.
- [24] T. Krüger, S. Frijters, F. Günther, B. Kaoui, and J. Harting. Numerical simulations of complex fluid-fluid interface dynamics. *European Physics Journal: Special Topics*, 222:177, 2013.
- [25] R. S. Macomber. *Complete introduction to modern NMR spectroscopy*. Wiley, New York, 1998.

- [26] A. F. Craievich. Synchrotron SAXS Studies of Nanostructured Materials and Colloidal Solutions: A Review. *Materials Research*, 5(1):1–11, 2002.
- [27] G. Binnig, C. F. Quate, and C. Gerber. Atomic Force Microscope. *Physical Review Letters*, 56(9):930–933, 1986.
- [28] B.-H. Jo, L. Van Lerberghe, K. Motsegood, and D. Beebe. Three-dimensional micro-channel fabrication in polydimethylsiloxane (PDMS) elastomer. *Journal of Microelectromechanical Systems*, 9(1):76–81, 2000.
- [29] J. J. Allen. *Micro Electro Mechanical System Design*. CRC Press, 2005.
- [30] S. E. Lyshevski. *MEMS and NEMS: Systems, Devices, and Structures*. CRC Press, 2013.
- [31] J. Anderson. *Computational Fluid Dynamics*. McGraw-Hill Education, 1995.
- [32] T. J. Chung. *Computational Fluid Dynamics*. Cambridge University Press, 2010.
- [33] G. A. Bird. Direct Simulation and the Boltzmann Equation. *Physics of Fluids*, 13(11):2676–2681, 1970.
- [34] G. Bird. *Molecular Gas Dynamics and the Direct Simulation of Gas Flows*. Clarendon, 1994.
- [35] R. Y. Rubinstein and D. P. Kroese. *Simulation and the Monte Carlo Method*. John Wiley & Sons, 2011.
- [36] S. Wolfram. *Cellular Automata and Complexity*. Perseus Books Group, 1994.
- [37] B. Chopard and M. Droz. *Cellular Automata Modeling of Physical Systems*. Cambridge University Press, Cambridge, UK, 2005.
- [38] D. A. Wolf-Gladrow. *Lattice-Gas Cellular Automata and lattice Boltzmann models*. Springer, 2000.
- [39] U. Frisch, B. Hasslacher, and Y. Pomeau. Lattice-gas automata for the Navier-Stokes equation. *Physical Review Letters*, 56(14):1505, 1986.
- [40] U. Frisch, D. d’Humières, B. Hasslacher, P. Lallemand, Y. Pomeau, and J. Rivet. Lattice gas hydrodynamics in two and three dimensions. *Complex Systems*, 1:649, 1987.
- [41] G. R. McNamara and G. Zanetti. Use of the Boltzmann Equation to Simulate Lattice-Gas Automata. *Physical Review Letters*, 61(20):2332–2335, 1988.
- [42] F. J. Higuera and J. Jiménez. Boltzmann Approach to Lattice Gas Simulations. *Europhysics Letters*, 9(7):663, 1989.

- [43] Y. H. Qian, D. D’Humières, and P. Lallemand. Lattice BGK Models for Navier-Stokes Equation. *Europhysics Letters*, 17(6):479, 1992.
- [44] D. d’Humières. Generalized lattice Boltzmann equations. Rarefied gas dynamics: theory and simulations. *Progress in Astronautics and Aeronautics*, 159, 1992.
- [45] H. Chen, S. Chen, and W. H. Matthaeus. Recovery of the Navier-Stokes equations using a lattice-gas Boltzmann method. *Physical Review A*, 45(8):R5339–R5342, 1992.
- [46] S. Chen and G. D. Doolen. Lattice Boltzmann Method for Fluid Flows. *Annual Review of Fluid Mechanics*, 30(1):329–364, 1998.
- [47] S. Succi. *The Lattice Boltzmann Equation: For Fluid Dynamics and Beyond*. Oxford University Press, 2001.
- [48] C. K. Aidun and J. R. Clausen. Lattice-Boltzmann Method for Complex Flows. *Annual Review of Fluid Mechanics*, 42(1):439–472, 2010.
- [49] X. He and L.-S. Luo. A priori derivation of the lattice Boltzmann equation. *Physical Review E*, 55(6):R6333–R6336, 1997.
- [50] H. Liu, Q. Kang, C. R. Leonardi, B. D. Jones, S. Schmieschek, A. Narváez, J. R. Williams, A. J. Valocchi, and J. Harting. Multiphase lattice Boltzmann simulations for porous media applications – a review. *Computational Geoscience*, in press, 2015. arXiv: 1404.7523.
- [51] H. Chen, S. Succi, and S. Orszag. Analysis of subgrid turbulence using the lattice Boltzmann BGK kinetic equation. *Physical Review E*, 59:R2529, 1999.
- [52] C. M. Teixeira. Incorporating turbulence models into the Lattice-Boltzmann method. *International Journal of Modern Physics C*, 9(8):1159, 1998.
- [53] H. Yu, S. S. Girimaji, and L.-S. Luo. DNS and LES of decaying isotropic turbulence with and without frame rotation using lattice Boltzmann method. *Journal of Computational Physics*, 209(2):599–616, 2005.
- [54] J. Lätt, B. Chopard, S. Succi, and F. Toschi. Numerical analysis of the averaged flow field in a turbulent lattice Boltzmann simulation. *Physica A*, 362(1):6–10, 2006.
- [55] L. Biferale, F. Mantovani, M. Sbragaglia, A. Scagliarini, F. Toschi, and R. Tripiccone. High resolution numerical study of Rayleigh-Taylor turbulence using a thermal lattice Boltzmann scheme. *Physics of Fluids*, 22(11):115112, 2010.
- [56] H. Stone, A. Stroock, and A. Ajdari. Engineering flows in small devices - Microfluidics Toward a Lab-on-a-Chip. *Annual Review of Fluid Mechanics*, 36:381–411, 2004.

- [57] T. M. Squires and S. R. Quake. Microfluidics: Fluid physics at the nanoliter scale. *Reviews of Modern Physics*, 77(3):977–1026, 2005.
- [58] M. Ma and R. M. Hill. Superhydrophobic surfaces. *Current Opinion in Colloid & Interface Science*, 11(4):193–202, 2006.
- [59] P. Roach, N. J. Shirtcliffe, and M. I. Newton. Progress in superhydrophobic surface development. *Soft Matter*, 4(2):224, 2008.
- [60] B. Bhushan, M. Nosonovsky, and Y. C. Jung. Lotus Effect: Roughness-Induced Superhydrophobic Surfaces. In *Nanotribology and Nanomechanics*, pages 995–1072. Springer Berlin Heidelberg, 2008.
- [61] C. Kunert and J. Harting. Roughness induced apparent boundary slip in microchannel flows. *Physical Review Letters*, 99:176001, 2007.
- [62] D. Mark, S. Haeberle, G. Roth, F. von Stetten, and R. Zengerle. Microfluidic lab-on-a-chip platforms: requirements, characteristics and applications. *Chemical Society Reviews*, 39(3):1153, 2010.
- [63] K. Gupta, D.-H. Kim, D. Ellison, C. Smith, A. Kundu, J. Tuan, K.-Y. Suh, and A. Levchenko. Lab-on-a-chip devices as an emerging platform for stem cell biology. *Lab on a Chip*, 10(16):2019, 2010.
- [64] Y. Sun, R. Dhumpa, D. D. Bang, J. Hogberg, K. Handberg, and A. Wolff. A lab-on-a-chip device for rapid identification of avian influenza viral RNA by solid-phase PCR. *Lab on a Chip*, 11(8):1457, 2011.
- [65] E. J. Smith, W. Xi, D. Makarov, I. Mönch, S. Harazim, V. A. Bolaños Quiñones, C. K. Schmidt, Y. Mei, S. Sanchez, and O. G. Schmidt. Lab-in-a-tube: ultra-compact components for on-chip capture and detection of individual micro-/nanoorganisms. *Lab on a Chip*, 12(11):1917, 2012.
- [66] K. Maenaka. MEMS inertial sensors and their applications. In *5th International Conference on Networked Sensing Systems, 2008. INSS 2008*, pages 71–73, June 2008.
- [67] D. Qin, Y. Xia, J. A. Rogers, R. J. Jackman, X.-M. Zhao, and G. M. Whitesides. Microfabrication, Microstructures and Microsystems. In P. A. Manz and D. H. Becker, editors, *Microsystem Technology in Chemistry and Life Science*, number 194 in Topics in Current Chemistry, pages 1–20. Springer Berlin Heidelberg, 1998.
- [68] T. Zech, G. Bohner, O. Laus, J. Klein, and M. Fischer. Design, fabrication, and application of a massively parallel single-bead microreactor system for high-throughput experimentation in heterogeneous catalysis. *Review of Scientific Instruments*, 76(6):062215, 2005.

- [69] C. Neto, D. R. Evans, E. Bonaccorso, H. J. Butt, and V. S. J. Craig. Boundary slip in Newtonian liquids: a review of experimental studies. *Reports on Progress in Physics*, 68:2859, 2005.
- [70] A. M. Afonso, L. L. Ferrás, J. M. Nóbrega, M. A. Alves, and F. T. Pinho. Pressure-driven electrokinetic slip flows of viscoelastic fluids in hydrophobic microchannels. *Microfluidics and Nanofluidics*, 16(6):1131–1142, 2014.
- [71] P. Dutta, A. Beskok, and T. Warburton. Electroosmotic flow control in complex microgeometries. *Journal of Microelectromechanical Systems*, 11(1):36–44, 2002.
- [72] T. Vestad, D. W. M. Marr, and J. Oakey. Flow control for capillary-pumped microfluidic systems. *Journal of Micromechanics and Microengineering*, 14(11):1503, 2004.
- [73] J. Bear. *Dynamics of fluids in porous media*. Elsevier (New York), 1972.
- [74] M. Sahimi. *Flow and Transport in Porous Media and Fractured Rock: From Classical Methods to Modern Approaches*. VCH, Weinheim, Germany, 1995.
- [75] A. Hunt and R. Ewing. *Percolation Theory for Flow in Porous Media*. Springer, 2009.
- [76] L. Lake. *Enhanced Oil Recovery*. Prentice Hall, Englewood Cliffs, 1989.
- [77] F. Alonso-Marroquin, H. J. Herrmann, and I. Vardoulakis. Micromechanical Investigation of soil plasticity: An investigation using a discrete model of polygonal particles. In *Proceeding of II international symposium of continuous and discontinuous modeling of cohesive-frictional materials*, Stuttgart, Germany, 2004.
- [78] M. H. Al-Dahhan, F. Larachi, M. P. Dudukovic, and A. Laurent. High-pressure trickle-bed reactors : A review. *Industrial & engineering chemistry research*, 36(8):3292–3314, 1997.
- [79] J. Zaman and A. Chakma. Inorganic membrane reactors. *Journal of Membrane Science*, 92(1):1–28, 1994.
- [80] J. Coronas and J. Santamaría. Catalytic reactors based on porous ceramic membranes. *Catalysis Today*, 51(3-4):377–389, 1999.
- [81] M. A. Mujeebu, M. Z. Abdullah, M. Z. A. Bakar, A. A. Mohamad, and M. K. Abdullah. Applications of porous media combustion technology - A review. *Applied Energy*, 86(9):1365–1375, 2009.
- [82] J. C. Slattery. Flow of viscoelastic fluids through porous media. *AIChE Journal*, 13(6):1066–1071, 1967.

- [83] J. Herzig, D. Leclerc, and P. Legoff. Flow of Suspensions Through Porous Media - Application to Deep Filtration. *Industrial and Engineering Chemistry*, 62(5):8, 1970.
- [84] E. Carrilho, A. W. Martinez, and G. M. Whitesides. Understanding Wax Printing: A Simple Micropatterning Process for Paper-Based Microfluidics. *Analytical chemistry*, 81(16):7091–7095, 2009.
- [85] A. K. Datta. Porous media approaches to studying simultaneous heat and mass transfer in food processes. I: Problem formulations. *Journal of Food Engineering*, 80(1):80–95, 2007.
- [86] M. J. Rosen and J. T. Kunjappu. *Surfactants and Interfacial Phenomena*. John Wiley & Sons, 2012.
- [87] K. Jousten. *Handbook of Vacuum Technology*. John Wiley & Sons, 2008.
- [88] B. Mertens, M. Weiss, H. Meiling, R. Klein, E. Louis, R. Kurt, M. Wedowski, H. Trenkler, B. Wolschrijn, R. Jansen, A. van de Runstraat, R. Moors, K. Spee, S. Ploger, and R. van de Kruijs. Progress in EUV optics lifetime expectations. *Microelectronic Engineering*, 73-4(Sp. Iss. SI):16–22, 2004.
- [89] M. A. Gallis, J. R. Torczynski, and D. J. Rader. An approach for simulating the transport of spherical particles in a rarefied gas flow via the direct simulation Monte Carlo method. *Physics of Fluids*, 13(11):3482–3492, 2001.
- [90] D. A. Kinkead, A. Grayfer, and O. P. Kishkovich. Prevention of optics and resist contamination in 300-mm lithography: improvements in chemical air filtration. In *SPIE Proceedings*, volume 4344, pages 739–752, 2001.
- [91] A. J. Dallas, K. M. Graham, M. Clarysse, and V. Fonderle. Characterization and control of organic airborne contamination in lithographic processing. In *SPIE Proceedings*, volume 4689, pages 1085–1109, 2002.
- [92] F. Feuillebois, M. Bazant, and O. Vinogradova. Effective Slip over Superhydrophobic Surfaces in Thin Channels. *Physical Review Letters*, 102(2), 2009.
- [93] E. Lauga and H. A. Stone. Effective slip in pressure-driven Stokes flow. *Journal of Fluid Mechanics*, 489:55–77, 2003.
- [94] N. V. Priezjev, A. A. Darhuber, and S. M. Troian. Slip behavior in liquid films on surfaces of patterned wettability. *Physical Review E*, 71:041608, 2005.
- [95] A. V. Belyaev and O. I. Vinogradova. Effective slip in pressure-driven flow past super-hydrophobic stripes. *Journal of Fluid Mechanics*, 652:489–499, 2010.
- [96] A. V. Belyaev and O. I. Vinogradova. Hydrodynamic interaction with superhydrophobic surfaces. *1004.0794*, 2010.

- [97] O. I. Vinogradova and A. V. Belyaev. Wetting, roughness and flow boundary conditions. *Journal of Physics: Condensed Matter*, 23(18):184104, 2011.
- [98] S. Schmieschek, A. V. Belyaev, J. Harting, and O. I. Vinogradova. Tensorial slip of superhydrophobic channels. *Physical Review E*, 85:016324, 2012.
- [99] L. Euler. *Die Gesetze des Gleichgewichts und der Bewegung flüssiger Körper*. S.L. Crusius, 1806.
- [100] O. Reynolds. An Experimental Investigation of the Circumstances Which Determine Whether the Motion of Water Shall Be Direct or Sinuous, and of the Law of Resistance in Parallel Channels. *Philosophical Transactions of the Royal Society of London*, 174:935–982, 1883.
- [101] Y. Sone. *Kinetic Theory and Fluid Dynamics*. Springer Science & Business Media, 2002.
- [102] D. Bernoulli. *Hydrodynamica*. Johannis Reinholdi Dulseckeri, 1738.
- [103] R. Clausius. Über die bewegende Kraft der Wärme und die Gesetze, welche sich daraus für die Wärmelehre selbst ableiten lassen. *Annalen der Physik*, 155(3):368–397, 1850.
- [104] R. Clausius. Über verschiedene für die Anwendung bequeme Formen der Hauptgleichungen der mechanischen Wärmetheorie. *Annalen der Physik*, 201(7):353–400, 1865.
- [105] J. Maxwell. On stresses in rarified gases arising from inequalities of temperature. *Philosophical Transactions of the Royal Society of London*, 70:287, 1879.
- [106] J. W. Gibbs. *Elementary Principles in Statistical Mechanics*. C. Scribner's sons, 1902.
- [107] J. W. Gibbs. *Scientific papers*. Longmans, Green, London, 1906.
- [108] L. Boltzmann. Weitere Studien über das Wärmegleichgewicht unter Gasmolekülen. In *Kinetische Theorie II*, number 67 in WTB Wissenschaftliche Taschenbücher, pages 115–225. Vieweg+Teubner Verlag, 1970.
- [109] A. Einstein. *Investigations on the Theory of the Brownian Movement*. Courier Dover Publications, 1956.
- [110] M. von Smoluchowski. Zur kinetischen Theorie der Brownschen Molekularbewegung und der Suspensionen. *Annalen der Physik*, 326(14):756–780, 1906.
- [111] S. Chapman. On the Law of Distribution of Molecular Velocities, and on the Theory of Viscosity and Thermal Conduction, in a Non-Uniform Simple Monatomic Gas. *Philosophical Transactions of the Royal Society of London A*, 216(538-548):279–348, 1916.

- [112] S. Chapman. On the Kinetic Theory of a Gas. Part II: A Composite Monatomic Gas: Diffusion, Viscosity, and Thermal Conduction. *Philosophical Transactions of the Royal Society of London A*, 217:115–197, 1918.
- [113] D. Enskog. *Kinetische Theorie der Vorgänge in mässig verdünnten Gasen*. Dissertation, Uppsala Universitet, 1917.
- [114] P. L. Bhatnagar, E. P. Gross, and M. Krook. A Model for Collision Processes in Gases. I. Small Amplitude Processes in Charged and Neutral One-Component Systems. *Physical Review*, 94(3):511–525, 1954.
- [115] H. Struchtrup. Macroscopic transport equations for rarefied gas flows. In *Macroscopic Transport Equations for Rarefied Gas Flows*, Interaction of Mechanics and Mathematics, pages 145–160. Springer Berlin Heidelberg, 2005.
- [116] S. Jin and M. Slemrod. Regularization of the Burnett Equations via Relaxation. *Journal of Statistical Physics*, 103(5-6):1009–1033, 2001.
- [117] B. J. Alder and T. E. Wainwright. Studies in Molecular Dynamics. I. General Method. *The Journal of Chemical Physics*, 31(2):459–466, 1959.
- [118] S. Pronk, S. Páll, R. Schulz, P. Larsson, P. Bjelkmar, R. Apostolov, M. R. Shirts, J. C. Smith, P. M. Kasson, D. v. d. Spoel, B. Hess, and E. Lindahl. GROMACS 4.5: A high-throughput and highly parallel open source molecular simulation toolkit. *Bioinformatics*, page 845, 2013.
- [119] M. T. Nelson, W. Humphrey, A. Gursoy, A. Dalke, L. V. Kalé, R. D. Skeel, and K. Schulten. NAMD: a Parallel, Object-Oriented Molecular Dynamics Program. *International Journal of High Performance Computing Applications*, 10(4):251–268, 1996.
- [120] S. Plimpton, P. Crozier, and A. Thompson. LAMMPS-large-scale atomic/molecular massively parallel simulator. *Sandia National Laboratories*, 2007.
- [121] L. Rekvig and D. Frenkel. Molecular simulations of droplet coalescence in oil/water/surfactant systems. *The Journal of Chemical Physics*, 127(13):134701, 2007.
- [122] D. C. Wilcox. *Turbulence Modeling for CFD*. DCW industries, La Canada, CA, 1998.
- [123] C. Hirsch. *Numerical Computation of Internal and External Flows: The Fundamentals of Computational Fluid Dynamics: The Fundamentals of Computational Fluid Dynamics*. Butterworth-Heinemann, 2007.
- [124] ANSYS 16.0 Capabilities - Brochure, 2015. <http://www.ansys.com/Products/ANSYS+16.0+Release+Highlights>.

- [125] H. Jasak, A. Jemcov, and Z. Tukovic. OpenFOAM: A C++ library for complex physics simulations. In *International workshop on coupled methods in numerical dynamics*, volume 1000, pages 1–20, 2007.
- [126] A. Comsol. COMSOL multiphysics user’s guide. *Version: September*, 2005.
- [127] P. J. Hoogerbrugge and J. M. V. A. Koelman. Simulating Microscopic Hydrodynamic Phenomena with Dissipative Particle Dynamics. *Europhysics Letters*, 19(3):155, 1992.
- [128] A. Malevanets and R. Kapral. Mesoscopic model for solvent dynamics. *The Journal of Chemical Physics*, 110(17):8605, 1999.
- [129] R. A. Gingold and J. J. Monaghan. Smoothed particle hydrodynamics: theory and application to non-spherical stars. *Monthly Notices of the Royal Astronomical Society*, 181(3):375–389, 1977.
- [130] L. Landau and E. Lifshitz. *Fluid mechanics*. Pergamon Press, 1959.
- [131] J.-L. Barrat and J.-P. Hansen. *Basic Concepts for Simple and Complex Liquids*. Cambridge University Press, 2003.
- [132] C. Cercignani. *The Boltzmann equation and its applications*, volume 67 of *Applied Mathematical Sciences*. Springer, New York, NY, 1988.
- [133] L. Landau and E. Lifshitz. *Statistical Physics Part 1*, volume 5 of *Course of Theoretical Physics*. Pergamon Press, 1980.
- [134] J. Maxwell. *Theory of Heat*. Courier Dover Publications, 2012.
- [135] R. K. Agarwal, K.-Y. Yun, and R. Balakrishnan. Beyond Navier-Stokes: Burnett equations for flows in the continuum-transition regime. *Physics of Fluids*, 13(10):3061–3085, 2001.
- [136] Self-diffusion coefficient. In M. Nič, J. Jiráť, B. Košata, A. Jenkins, and A. McNaught, editors, *IUPAC Compendium of Chemical Terminology*. IUPAC, Research Triangle Park, NC, 2.1.0 edition, June 2009.
- [137] Z. Guo, C. Zheng, and B. Shi. Discrete lattice effects on the forcing term in the lattice Boltzmann method. *Physical Review E*, 65(4):046308, 2002.
- [138] R. Mei, D. Yu, W. Shyy, and L.-S. Luo. Force evaluation in the lattice Boltzmann method involving curved geometry. *Physical Review E*, 65(4):041203, 2002.
- [139] A. Narváez, T. Zauner, F. Raischel, R. Hilfer, and J. Harting. Quantitative analysis of numerical estimates for the permeability of porous media from lattice-Boltzmann simulations. *Journal of Statistical Mechanics: Theory and Experiment*, 2010(11):P11026, 2010.

- [140] H. Huang, D. T. Thorne, M. G. Schaap, and M. C. Sukop. Proposed approximation for contact angles in Shan-and-Chen-type multicomponent multiphase lattice Boltzmann models. *Physical Review E*, 76(6):066701, 2007.
- [141] S. Schmieschek and J. Harting. Contact angle determination in multicomponent lattice Boltzmann simulations. *Communications in computational physics*, 9:1165–1178, 2011.
- [142] J. S. Rowlinson and B. Widom. *Molecular Theory of Capillarity*. Dover Publications, 2002.
- [143] P.-G. de Gennes, F. Brochard-Wyart, and D. Quere. *Capillarity and Wetting Phenomena: Drops, Bubbles, Pearls, Waves*. Springer Science & Business Media, 2004.
- [144] C. L. M. H. Navier. Mémoire sur les lois du mouvement des fluides. *Mémoires de l'Académie Royale des Sciences de l'Institut de France*, 6:389–440, 1823.
- [145] H. Darcy. *Les fontaines publiques de la ville de Dijon*. Dalmont, Paris, 1856.
- [146] P. Toledo. *Fluids in Porous Media: Porosimetry, Pore Structure, Flow and Transport*. PhD thesis, Chemical Engineering, University of Minnesota, 1990.
- [147] F. Dullien. *Porous Media: Fluid Transport and Pore Structure*. Academic Press, San Diego, 2 edition, 1992.
- [148] N. G. Hadjiconstantinou. The limits of Navier-Stokes theory and kinetic extensions for describing small-scale gaseous hydrodynamics. *Physics of Fluids*, 18(11):111301, 2006.
- [149] S. Chapman and T. G. Cowling. *The mathematical theory of non-uniform gases: an account of the kinetic theory of viscosity, thermal conduction and diffusion in gases*. Cambridge university press, 1991.
- [150] E. A. Mason, A. P. Malinauskas, and R. B. Evans. Flow and Diffusion of Gases in Porous Media. *The Journal of Chemical Physics*, 46(8):3199–3216, 1967.
- [151] H. Struchtrup and P. Taheri. Macroscopic transport models for rarefied gas flows: a brief review. *IMA Journal of Applied Mathematics*, 76(5):672–697, 2011.
- [152] J. Gibbons. Collisionless Boltzmann equations and integrable moment equations. *Physica D*, 3(3):503 – 511, 1981.
- [153] R. Benzi, S. Succi, and M. Vergassola. The lattice Boltzmann equation: theory and applications. *Physics Reports*, 222(3):145–197, 1992.
- [154] X. He and L.-S. Luo. Theory of the lattice Boltzmann method: from the Boltzmann equation to the lattice Boltzmann equation. *Physical Review E*, 56, 1997.

- [155] K. K. Mattila, D. N. Siebert, L. A. Hegele, and P. C. Philippi. High-order lattice-Boltzmann equations and stencils for multiphase models. *International Journal of Modern Physics C*, 24(12):1340006, 2013.
- [156] M. Hecht and J. Harting. Implementation of on-site velocity boundary conditions for D3q19 lattice Boltzmann simulations. *Journal of Statistical Mechanics: Theory and Experiment*, 2010(01):P01018, 2010.
- [157] M. Sbragaglia and X. Shan. Consistent pseudopotential interactions in lattice Boltzmann models. *Physical Review E*, 84(3):036703, 2011.
- [158] D. d’Humières. Multiple-relaxation-time lattice Boltzmann models in three dimensions. *Philosophical Transactions of the Royal Society of London A*, 360(1792):437–451, 2002.
- [159] K. N. Premnath and J. Abraham. Three-dimensional multi-relaxation time (MRT) lattice-Boltzmann models for multiphase flow. *Journal of Computational Physics*, 224(2):539–559, 2007.
- [160] C. Pan, L.-S. Luo, and C. T. Miller. An evaluation of lattice Boltzmann schemes for porous medium flow simulation. *Computers & Fluids*, 35(8-9):898–909, 2006.
- [161] A. K. Gunstensen, D. H. Rothman, S. Zaleski, and G. Zanetti. Lattice Boltzmann model of immiscible fluids. *Physical Review A*, 43(8):4320–4327, 1991.
- [162] D. Rothman and J. Keller. Immiscible cellular-automaton fluids. *Journal of Statistical Physics*, 52(3-4):1119, 1988.
- [163] X. Shan and H. Chen. Lattice Boltzmann model for simulating flows with multiple phases and components. *Physical Review E*, 47(3):1815–1819, 1993.
- [164] X. Shan and H. Chen. Simulation of nonideal gases and liquid-gas phase transitions by the lattice Boltzmann equation. *Physical Review E*, 49(4):2941–2948, 1994.
- [165] M. R. Swift, W. R. Osborn, and J. M. Yeomans. Lattice Boltzmann simulation of nonideal fluids. *Physical Review E*, 75(5):830, 1995.
- [166] E. Orlandini, M. R. Swift, and J. M. Yeomans. A lattice Boltzmann model of binary-fluid mixtures. *Europhysics Letters*, 32(6):463, 1995.
- [167] X. He, X. Shan, and G. D. Doolen. Discrete Boltzmann equation model for nonideal gases. *Physical Review E*, 57(1):R13–R16, 1998.
- [168] X. He, S. Chen, and R. Zhang. A Lattice Boltzmann Scheme for Incompressible Multiphase Flow and Its Application in Simulation of Rayleigh-Taylor Instability. *Journal of Computational Physics*, 152(2):642–663, 1999.

- [169] D. Grunau, S. Chen, and K. Eggert. A Lattice Boltzmann model for multiphase fluid flows. *Physics of Fluids A*, 5(10):2557–2562, 1993.
- [170] S. V. Lishchuk, C. M. Care, and I. Halliday. Lattice Boltzmann algorithm for surface tension with greatly reduced microcurrents. *Physical Review E*, 67:036701, 2003.
- [171] M. Latva-Kokko and D. H. Rothman. Diffusion properties of gradient-based lattice Boltzmann models of immiscible fluids. *Physical Review E*, 71:056702, 2005.
- [172] T. Reis and T. N. Phillips. Lattice Boltzmann model for simulating immiscible two-phase flows. *Journal of Physics A*, 40(14):4033, 2007.
- [173] J. Chin, E. S. Boek, and P. V. Coveney. Lattice-Boltzmann simulation of the flow of binary immiscible fluids with different viscosities using the Shan-Chen microscopic interaction model. *Proceedings of the Royal Society of London A*, 360:547, 2002.
- [174] Q. Kang, D. Zhang, S. Chen, and X. He. Lattice Boltzmann simulation of chemical dissolution in porous media. *Physical Review E*, 65(3):036318, 2002.
- [175] P. Yuan and L. Schaefer. Equations of state in a lattice Boltzmann model. *Physics of Fluids*, 18(4):042101, 2006.
- [176] R. S. Qin. Mesoscopic interparticle potentials in the lattice Boltzmann equation for multiphase fluids. *Physical Review E*, 73(6):066703, 2006.
- [177] G. Falcucci, G. Bella, G. Shiatti, S. Chibbaro, M. Sbragaglia, and S. Succi. Lattice Boltzmann Models with Mid-Range Interactions. *Communications in computational physics*, 2:1071–1084, 2007.
- [178] M. Sbragaglia, R. Benzi, L. Biferale, S. Succi, K. Sugiyama, and F. Toschi. Generalized lattice Boltzmann method with multirange pseudopotential. *Physical Review E*, 75(2):026702, 2007.
- [179] T. Inamuro, N. Konishi, and F. Ogino. A Galilean invariant model of the lattice Boltzmann method for multiphase fluid flows using free-energy approach. *Computer Physics Communications*, 129(1-3):32–45, 2000.
- [180] A. N. Kalarakis, V. N. Burganos, and A. C. Payatakes. Galilean-invariant lattice-Boltzmann simulation of liquid-vapor interface dynamics. *Physical Review E*, 65(5):056702, 2002.
- [181] H. W. Zheng, C. Shu, and Y. T. Chew. A lattice Boltzmann model for multiphase flows with large density ratio. *Journal of Computational Physics*, 218(1):353–371, 2006.

- [182] T. Inamuro, T. Ogata, S. Tajima, and N. Konishi. A lattice Boltzmann method for incompressible two-phase flows with large density differences. *Journal of Computational Physics*, 198(2):628–644, 2004.
- [183] T. Lee and C.-L. Lin. A stable discretization of the lattice Boltzmann equation for simulation of incompressible two-phase flows at high density ratio. *Journal of Computational Physics*, 206(1):16–47, 2005.
- [184] S. Mukherjee and J. Abraham. Lattice Boltzmann simulations of two-phase flow with high density ratio in axially symmetric geometry. *Physical Review E*, 75(2):026701, 2007.
- [185] T. Krüger, F. Varnik, and D. Raabe. Efficient and accurate simulations of deformable particles immersed in a fluid using a combined immersed boundary lattice Boltzmann finite element method. *Computers & Mathematics with Applications*, 61(12):3485–3505, 2011.
- [186] H. Liu, A. J. Valocchi, and Q. Kang. Three-dimensional lattice Boltzmann model for immiscible two-phase flow simulations. *Physical Review E*, 85(4):046309, 2012.
- [187] M. R. Swift, E. Orlandini, W. R. Osborn, and J. M. Yeomans. Lattice-Boltzmann simulations of liquid-gas and binary fluid mixtures. *Physical Review E*, 54(5):5041, 1996.
- [188] M. Sbragaglia, H. Chen, X. Shan, and S. Succi. Continuum free-energy formulation for a class of lattice Boltzmann multiphase models. *Europhysics Letters*, 86(2):24005, 2009.
- [189] S. Chibbaro, G. Falcucci, G. Chiatti, H. Chen, X. Shan, and S. Succi. Lattice Boltzmann models for nonideal fluids with arrested phase-separation. *Physical Review E*, 77(3):036705, 2008.
- [190] X. Shan. Pressure tensor calculation in a class of nonideal gas lattice Boltzmann models. *Physical Review E*, 77(6):066702, 2008.
- [191] R. Benzi, L. Biferale, M. Sbragaglia, S. Succi, and F. Toschi. Mesoscopic modeling of a two-phase flow in the presence of boundaries: The contact angle. *Physical Review E*, 74:021509, 2006.
- [192] C. Y. Lim, C. Shu, X. D. Niu, and Y. T. Chew. Application of lattice Boltzmann method to simulate microchannel flows. *Physics of Fluids*, 14(7):2299–2308, 2002.
- [193] X. Nie, G. D. Doolen, and S. Chen. Lattice-Boltzmann Simulations of fluid flows in MEMS. *Journal of Statistical Physics*, 107(112):279, 2002.

- [194] M. Sbragaglia and S. Succi. Analytical calculation of slip flow in lattice Boltzmann models with kinetic boundary conditions. *Physics of Fluids*, 17(9):093602, 2005.
- [195] S. Succi. Mesoscopic modeling of slip motion at fluid-solid interfaces with heterogeneous catalysis. *Physical Review Letters*, 89(6):064502, 2002.
- [196] S. Ansumali and I. V. Karlin. Kinetic boundary conditions in the lattice Boltzmann method. *Physical Review E*, 66(2):026311, 2002.
- [197] V. Sofonea and R. F. Sekerka. Diffuse-reflection boundary conditions for a thermal lattice Boltzmann model in two dimensions: Evidence of temperature jump and slip velocity in microchannels. *Physical Review E*, 71(6):066709, 2005.
- [198] M. Sbragaglia, R. Benzi, L. Biferale, S. Succi, and F. Toschi. Surface roughness-hydrophobicity coupling in microchannel and nanochannel flows. *Physical Review Letters*, 97:204503, 2006.
- [199] J. Harting, C. Kunert, and H. J. Herrmann. Lattice Boltzmann simulations of apparent slip in hydrophobic microchannels. *Europhysics Letters*, 75:328–334, 2006.
- [200] M. Bouzidi, M. Firdaouss, and P. Lallemand. Momentum transfer of a Boltzmann-lattice fluid with boundaries. *Physics of Fluids*, 13(11):3452–3459, 2001.
- [201] R. Verberg and A. Ladd. Accuracy and stability of a lattice-Boltzmann model with subgrid scale boundary conditions. *Physical Review E*, 65:016701, 2001.
- [202] A. J. C. Ladd. Numerical simulations of particulate suspensions via a discretized Boltzmann equation. Part 1. Theoretical foundation. *Journal of Fluid Mechanics*, 271:285–309, 1994.
- [203] A. J. C. Ladd. Numerical simulations of particulate suspensions via a discretized Boltzmann equation. Part 2. Numerical results. *Journal of Fluid Mechanics*, 271:311–339, 1994.
- [204] P. Lallemand and L. S. Luo. Lattice Boltzmann method for moving boundaries. *Journal of Computational Physics*, 184(2):406–421, 2003.
- [205] R. Mei, L.-S. Luo, and W. Shyy. An Accurate Curved Boundary Treatment in the Lattice Boltzmann Method. *Journal of Computational Physics*, 155(2):307–330, 1999.
- [206] R. Verberg and A. J. C. Ladd. Lattice-Boltzmann Model with Sub-Grid-Scale Boundary Conditions. *Physical Review Letters*, 84(10):2148–2151, 2000.

- [207] I. Ginzburg and D. D’Humières. Multireflection boundary conditions for lattice Boltzmann models. *Physical Review E*, 68(6):066614, 2003.
- [208] Z. Guo, T. S. Zhao, and Y. Shi. Physical symmetry, spatial accuracy, and relaxation time of the lattice Boltzmann equation for microgas flows. *Journal of Applied Physics*, 99(7):074903, 2006.
- [209] Z. Guo and C. Zheng. Analysis of lattice Boltzmann equation for microscale gas flows: Relaxation times, boundary conditions and the Knudsen layer. *International Journal of Computational Fluid Dynamics*, 22(7):465–473, 2008.
- [210] T. Lee and C.-L. Lin. Rarefaction and compressibility effects of the lattice-Boltzmann-equation method in a gas microchannel. *Physical Review E*, 71(4):046706, 2005.
- [211] F. Toschi and S. Succi. Lattice Boltzmann method at finite Knudsen numbers. *Europhysics Letters*, 69(4):549, 2005.
- [212] S. H. Kim, H. Pitsch, and I. D. Boyd. Slip velocity and Knudsen layer in the lattice Boltzmann method for microscale flows. *Physical Review E*, 77(2):026704, 2008.
- [213] G. H. Tang, W. Q. Tao, and Y. L. He. Lattice Boltzmann method for gaseous microflows using kinetic theory boundary conditions. *Physics of Fluids*, 17(5):058101, 2005.
- [214] X.-D. Niu, S.-A. Hyodo, T. Munekata, and K. Suga. Kinetic lattice Boltzmann method for microscale gas flows: Issues on boundary condition, relaxation time, and regularization. *Physical Review E*, 76(3):036711, 2007.
- [215] Y.-H. Zhang, X.-J. Gu, R. Barber, and D. Emerson. Capturing Knudsen layer phenomena using a lattice Boltzmann model. *Physical Review E*, 74(4):046704, 2006.
- [216] R. Cornubert, D. d’Humières, and D. Levermore. A Knudsen layer theory for lattice gases. *Physica D*, 47(1-2):241–259, 1991.
- [217] P. Lavallée, J. P. Boon, and A. Noullez. Boundaries in lattice gas flows. *Physica D*, 47(1-2):233–240, 1991.
- [218] D. P. Ziegler. Boundary conditions for lattice Boltzmann simulations. *Journal of Statistical Physics*, 71(5-6):1171–1177, 1993.
- [219] I. Ginzburg and P. Adler. Boundary flow condition analysis for the three dimensional lattice Boltzmann model. *Journal Physique II*, 4, 1994.
- [220] M. A. Gallivan, D. R. Noble, J. G. Georgiadis, and R. O. Buckius. An evaluation of the bounce-back boundary condition for lattice Boltzmann simulations. *International Journal for Numerical Methods in Fluids*, 25(3):249–263, 1997.

- [221] X. He, Q. Zou, L.-S. Luo, and M. Dembo. Analytic solutions and analysis on non-slip boundary conditions for the lattice Boltzmann BGK model. *Journal of Statistical Physics*, 87(1/2):115–136, 1997.
- [222] D. D’Humières and I. Ginzburg. Viscosity independent numerical errors for Lattice Boltzmann models: From recurrence equations to "magic" collision numbers. *Computers & Mathematics with Applications*, 58(5):823–840, 2009.
- [223] I. Ginzburg. Generic boundary conditions for lattice Boltzmann models and their application to advection and anisotropic dispersion equations. *Advances in Water Resources*, 28(11):1196–1216, 2005.
- [224] N. S. Martys and H. Chen. Simulation of multicomponent fluids in complex three-dimensional geometries by the Lattice Boltzmann method. *Physical Review E*, 53(1):743, 1996.
- [225] J. Harting, C. Kunert, and J. Hyväluoma. Lattice Boltzmann simulations in microfluidics: probing the no-slip boundary condition in hydrophobic, rough, and surface nanobubble laden microchannels. *Microfluidics and Nanofluidics*, 8(1):1–10, 2010.
- [226] Q. Zou and X. He. On pressure and velocity boundary conditions for the lattice Boltzmann BGK model. *Physics of Fluids*, 9(6):1591–1598, 1997.
- [227] M. E. Kutay, A. H. Aydilek, and E. Masad. Laboratory validation of lattice Boltzmann method for modeling pore-scale flow in granular materials. *Computers and Geotechnics*, 33(8):381–395, 2006.
- [228] K. Mattila, J. Hyväluoma, and T. Rossi. Mass-flux-based outlet boundary conditions for the lattice Boltzmann method. *Journal of Statistical Mechanics: Theory and Experiment*, 2009(06):P06015, 2009.
- [229] N. K. Ahmed and M. Hecht. A boundary condition with adjustable slip length for lattice Boltzmann simulations. *Journal of Statistical Mechanics: Theory and Experiment*, 2009(09):P09017, 2009.
- [230] Y. Zhang, R. Qin, and D. R. Emerson. Lattice Boltzmann simulation of rarefied gas flows in microchannels. *Physical Review E*, 71(4):047702, 2005.
- [231] S. Ansumali, I. Karlin, C. Frouzakis, and K. Boulouchos. Entropic lattice Boltzmann method for microflows. *Physica A*, 359:289–305, 2006.
- [232] E. S. Asmolov, S. Schmieschek, J. Harting, and O. I. Vinogradova. Flow past superhydrophobic surfaces with cosine variation in local slip length. *Physical Review E*, 87(2):023005, 2013.
- [233] A. L. Dubov, S. Schmieschek, E. S. Asmolov, J. Harting, and O. I. Vinogradova. Lattice-Boltzmann simulations of the drag force on a sphere approaching a superhydrophobic striped plane. *The Journal of Chemical Physics*, 140(3):034707, 2014.

- [234] E. Lauga, M. Brenner, and H. Stone. Microfluidics: The No-Slip Boundary Condition. In P. C. T. Dr, P. A. L. Y. Dr, and P. J. F. F. Dr, editors, *Springer Handbook of Experimental Fluid Mechanics*, pages 1219–1240. Springer Berlin Heidelberg, 2007.
- [235] A. Lafuma and D. Quéré. Superhydrophobic states. *Nature Materials*, 2:457, 2003.
- [236] M. Z. Bazant and O. I. Vinogradova. Tensorial hydrodynamic slip. *Journal of Fluid Mechanics*, 613:125–134, 2008.
- [237] L. Bocquet and J. L. Barrat. Flow boundary conditions from nano- to microscales. *Soft Matter*, 3:685–693, 2007.
- [238] A. B. D. Cassie and S. Baxter. Wettability of porous surfaces. *Transactions of the Faraday Society*, 40(0):546–551, 1944.
- [239] A. B. D. Cassie. Contact angles. *Discussions of the Faraday Society*, 3(0):11–16, 1948.
- [240] P. Joseph, C. Cottin-Bizonne, J. M. Benoit, C. Ybert, C. Journet, P. Tabeling, and L. Bocquet. Slippage of water past superhydrophobic carbon nanotube forests in microchannels. *Physical Review Letters*, 97:156104, 2006.
- [241] E. S. Asmolov, A. V. Belyaev, and O. I. Vinogradova. Drag force on a sphere moving toward an anisotropic superhydrophobic plane. *Physical Review E*, 84:026330, 2011.
- [242] F. Feuillebois, M. Z. Bazant, and O. I. Vinogradova. Transverse flow in thin superhydrophobic channels. *Physical Review E*, 82:055301(R), 2010.
- [243] C. Ybert, C. Barentin, C. Cottin-Bizonne, P. M. Joseph, and L. Bocquet. Achieving large slip with superhydrophobic surfaces: Scaling laws for generic geometries. *Physics of Fluids*, 19:123601, 2007.
- [244] K. Kamrin, M. Z. Bazant, and H. A. Stone. Effective slip boundary conditions for arbitrary periodic surfaces: the surface mobility tensor. *Journal of Fluid Mechanics*, 658:409–437, 2010.
- [245] E. S. Asmolov, J. Zhou, F. Schmid, and O. I. Vinogradova. Effective slip-length tensor for a flow over weakly slipping stripes. *Physical Review E*, 88(2):023004, 2013.
- [246] D. Andrienko, P. Patricio, and O. I. Vinogradova. Capillary bridging and long-range attractive forces in a mean-field approach. *The Journal of Chemical Physics*, 121:4414–4423, 2004.

- [247] G. E. Yakubov, H. J. Butt, and O. I. Vinogradova. Interaction Forces between Hydrophobic Surfaces. Attractive Jump as an Indication of Formation of "Stable" Submicrocavities. *The Journal of Physical Chemistry B*, 104(15):3407 – 3410, 2000.
- [248] J. W. G. Tyrrell and P. Attard. Images of Nanobubbles on Hydrophobic Surfaces and Their Interactions. *Physical Review Letters*, 87(17):176104, 2001.
- [249] J. Hyväluoma and J. Harting. Slip flow over structured surfaces with entrapped microbubbles. *Submitted to Phys. Rev. Lett.*, arXiv:0801.1448, 2008.
- [250] A. M. J. Davis and E. Lauga. Geometric transition in friction for flow over a bubble mattress. *Physics of Fluids*, 21:011701, 2009.
- [251] M. Sbragaglia and A. Prosperetti. A note on the effective slip properties for microchannel flows with ultrahydrophobic surfaces. *Physics of Fluids*, 19:043603, 2007.
- [252] S. S. Bahga, O. I. Vinogradova, and M. Z. Bazant. Anisotropic electro-osmotic flow over super-hydrophobic surfaces. *Journal of Fluid Mechanics*, 614, 2009. in press.
- [253] A. V. Belyaev and O. I. Vinogradova. Electro-osmosis on anisotropic super-hydrophobic surfaces. *Physical Review Letters*, 107:098301, 2011.
- [254] E. S. Asmolov and O. I. Vinogradova. Effective slip boundary conditions for arbitrary one-dimensional surfaces. *Journal of Fluid Mechanics*, 706:108–117, 2012.
- [255] L. Zhu, D. Tretheway, L. Petzold, and C. Meinhardt. Simulation of fluid slip at 3d hydrophobic microchannel walls by the lattice Boltzmann method. *Journal of Computational Physics*, 202:181, 2005.
- [256] J. Zhang and D. Y. Kwok. Apparent slip over a solid-liquid interface with a no-slip boundary condition. *Physical Review E*, 70:056701, 2004.
- [257] R. Benzi, L. Biferale, M. Sbragaglia, S. Succi, and F. Toschi. Mesoscopic two-phase model for describing apparent slip in micro-channel flows. *Europhysics Letters*, 74(4):651, 2006.
- [258] X. D. Niu, C. Shu, and Y. T. Chew. A lattice Boltzmann BGK model for simulation of micro flows. *Europhysics Letters*, 67:600, 2004.
- [259] A. A. Alexeyev and O. I. Vinogradova. Flow of a Liquid in a Nonuniformly Hydrophobized Capillary. *Colloids and Surfaces A: Physicochemical and Engineering Aspects*, 108:173 – 179, 1996.
- [260] S. Frijters. Liquid-liquid and liquid-solid interactions on the mesoscale. 2015.

- [261] S. Schmieschek, A. Narváez Salazar, and J. Harting. Multi relaxation time lattice Boltzmann simulations of multiple component fluid flows in porous media. In M. R. W. Nagel, D. Kröner, editor, *High Performance Computing in Science and Engineering '12*, page 39. Springer, 2013.
- [262] A. Fasano. *Complex Flows in Industrial Processes*. Springer Science & Business Media, 2000.
- [263] W. Shyy and R. Narayanan. *Fluid Dynamics at Interfaces*. Cambridge University Press, 1999.
- [264] H.-J. Butt, K. Graf, and M. Kappl. *Physics and Chemistry of Interfaces*. Wiley-VCH, 2003.
- [265] D. Myers. *Surfactant Science and Technology*. John Wiley & Sons, 2005.
- [266] S. Frijters, F. Günther, and J. Harting. Effects of nanoparticles and surfactant on droplets in shear flow. *Soft Matter*, 8(24):6542, 2012.
- [267] F. Günther, F. Janoschek, S. Frijters, and J. Harting. Lattice Boltzmann simulations of anisotropic particles at liquid interfaces. *Computers & Fluids*, 80:184–189, 2013.
- [268] G. B. Davies, T. Krüger, P. V. Coveney, J. Harting, and F. Bresme. Assembling Ellipsoidal Particles at Fluid Interfaces Using Switchable Dipolar Capillary Interactions. *Advanced Materials*, 26(39):6715–6719, 2014.
- [269] R. Adhikari, K. Stratford, M. E. Cates, and A. J. Wagner. Fluctuating lattice Boltzmann. *Europhysics Letters*, 71:473, 2005.
- [270] B. Dünweg, U. D. Schiller, and A. J. C. Ladd. Statistical mechanics of the fluctuating lattice Boltzmann equation. *Physical Review E*, 76(3):036704, 2007.
- [271] M. Gross, R. Adhikari, M. E. Cates, and F. Varnik. Thermal fluctuations in the lattice Boltzmann method for nonideal fluids. *Physical Review E*, 82(5):056714, 2010.
- [272] M. Nekovee, P. V. Coveney, H. Chen, and B. M. Boghosian. Lattice-Boltzmann model for interacting amphiphilic fluids. *Physical Review E*, 62(6):8282–8294, 2000.
- [273] H. Chen, B. Boghosian, P. Coveney, and M. Nekovee. A ternary lattice-Boltzmann model for amphiphilic fluids. *Proceedings of the Royal Society of London A*, 456:2043, 2000.
- [274] J. B. Grotberg and D. P. G. III. A synopsis of surfactant spreading research. *Journal of Colloid and Interface Science*, 178:377, 1996.

- [275] C. Pozrikidis. A finite-element method for interfacial surfactant transport, with application to the flow-induced deformation of a viscous drop. *J. Eng. Math.*, 49(2):163–180, 2004.
- [276] A. J. James and J. Lowengrub. A surfactant-conserving volume-of-fluid method for interfacial flows with insoluble surfactant. *Journal of Computational Physics*, 201(2):685 – 722, 2004.
- [277] R. van der Sman and S. van der Graaf. Diffuse interface model of surfactant adsorption onto flat and droplet interfaces. *Rheologica Acta*, 46:3–11, 2006.
- [278] H. Liu and Y. Zhang. Phase-field modeling droplet dynamics with soluble surfactants. *Journal of Computational Physics*, 229(4):9166–9187, 2010.
- [279] O. Theissen, G. Gompper, and D. M. Kroll. Lattice-Boltzmann Model of amphiphilic systems. *Europhysics Letters*, 42:419, 1998.
- [280] P. J. Love, M. Nekovee, P. V. Coveney, J. Chin, N. González-Segredo, and J. M. R. Martin. Simulations of amphiphilic fluids using mesoscale lattice-Boltzmann and lattice-gas methods. *Computer Physics Communications*, 153(3):340, 2003.
- [281] J. Harting, J. Chin, M. Venturoli, and P. V. Coveney. Large-scale lattice Boltzmann simulations of complex fluids: advances through the advent of computational grids. *Philosophical Transactions of the Royal Society of London A*, 363:1895, 2005.
- [282] S. Khirevich, I. Ginzburg, and U. Tallarek. Coarse- and fine-grid numerical behavior of MRT/TRT lattice-Boltzmann schemes in regular and random sphere packings. *Journal of Computational Physics*, 281:708–742, 2015.
- [283] X. Shan and G. Doolen. Multicomponent lattice-Boltzmann model with interparticle interaction. *Journal of Statistical Physics*, 81(112):379, 1995.
- [284] I. Ginzburg. Equilibrium-type and link-type lattice Boltzmann models for generic advection and anisotropic-dispersion equation. *Advances in Water Resources*, 28(11):1171–1195, 2005.
- [285] L.-S. Luo, W. Liao, X. Chen, Y. Peng, and W. Zhang. Numerics of the lattice Boltzmann method: Effects of collision models on the lattice Boltzmann simulations. *Physical Review E*, 83(5):056710, 2011.
- [286] F. J. Higuera, S. Succi, and R. Benzi. Lattice gas dynamics with enhanced collisions. *Europhysics Letters*, 9(4):345, 1989.
- [287] P. Lallemand and F. Dubois. Some results on energy-conserving lattice Boltzmann models. *Computers & Mathematics with Applications*, 65(6):831–844, 2013.

- [288] A. Sarkar, A. Narváez, and J. Harting. Advection versus diffusion: A multicomponent lattice Boltzmann study of enhanced fluid mixing in passive micromixers. *In preparation*, 2015.
- [289] K. Wieghardt. *Theoretische Strömungslehre*. Göttinger Klassik, 1957.
- [290] K. Vafai. *Handbook of Porous Media, Second Edition*. CRC Press, 2005.
- [291] F. Dullien. *Porous Media Fluid Transport and Pore Structure*. Elsevier, 2012.
- [292] D. K. N. Sinz, M. Hanyak, J. C. H. Zeegers, and A. A. Darhuber. Insoluble surfactant spreading along thin liquid films confined by chemical surface patterns. *Physical Chemistry Chemical Physics*, 13(20):9768, 2011.
- [293] M. Hanyak, D. K. N. Sinz, and A. A. Darhuber. Soluble surfactant spreading on spatially confined thin liquid films. *Soft Matter*, 8(29):7660, 2012.
- [294] W. H. Fissell, A. T. Conlisk, S. Datta, J. M. Magistrelli, J. T. Glass, A. J. Fleischman, and S. Roy. High Knudsen number fluid flow at near-standard temperature and pressure conditions using precision nanochannels. *Microfluidics and Nanofluidics*, 10(2):425–433, 2011.
- [295] G. Karniadakis, A. Beskok, and N. Aluru. *Microflows and Nanoflows*. Springer Science+Business Media Inc., 2000.
- [296] T. J. Burns, R. W. Davis, and E. F. Moore. Dynamical Systems Approach to Particle Transport Modeling in Dilute Gas-Particle Flows with Application to a Chemical Vapor Deposition Reactor. *Aerosol Science and Technology*, 26(3):193–211, 1997.
- [297] C. Liu and Z. Li. Molecular Dynamics Simulation of Composite Nanochannels as Nanopumps Driven by Symmetric Temperature Gradients. *Physical Review Letters*, 105(17):174501, 2010.
- [298] Y. Li, J. Xu, and D. Li. Molecular dynamics simulation of nanoscale liquid flows. *Microfluidics and Nanofluidics*, 9(6):1011–1031, 2010.
- [299] J. E. Broadwell. Study of rarefied shear flow by the discrete velocity method. *Journal of Fluid Mechanics*, 19(03):401–414, 1964.
- [300] E. Oran. DIRECT SIMULATION MONTE CARLO: Recent Advances and Applications. *Annu. Rev. Fluid Mech.*, 30(1):403, 1998.
- [301] G. Tang, W. Tao, and Y. He. Lattice Boltzmann method for simulating gas flow in microchannels. *International Journal of Modern Physics B*, 15(2):335–347, 2004.

- [302] X. Shan, X.-F. Yuan, and H. Chen. Kinetic theory representation of hydrodynamics: a way beyond the Navier–Stokes equation. *Journal of Fluid Mechanics*, 550:413–441, 2006.
- [303] J. Fan and C. Shen. Statistical simulation of low-speed rarefied gas flows. *Journal of Computational Physics*, 167(2):393–412, 2001.
- [304] J. Chun and D. Koch. A direct simulation Monte Carlo method for rarefied gas flows in the limit of small Mach number. *Physics of Fluids*, 17(10), 2005.
- [305] R. Roveda, D. Goldstein, and P. Varghese. Hybrid Euler/particle approach for continuum/rarefied flows. *Journal of Spacecraft and Rockets*, 35(3):258–265, 1998.
- [306] H. Wijesinghe, R. Hornung, A. Garcia, and N. Hadjiconstantinou. Three-dimensional hybrid continuum-atomistic simulations for multiscale hydrodynamics. *Journal of Fluids Engineering - Transactions of the ASME*, 126(5):768–777, 2004.
- [307] J. M. Burt and I. D. Boyd. A hybrid particle approach for continuum and rarefied flow simulation. *Journal of Computational Physics*, 228(2):460–475, 2009.
- [308] S. V. Nedeia, A. J. H. Frijns, A. A. van Steenhoven, A. J. Markvoort, and P. A. J. Hilbers. Hybrid method coupling molecular dynamics and Monte Carlo simulations to study the properties of gases in microchannels and nanochannels. *Physical Review E*, 72(1):016705, 2005.
- [309] D. K. N. Sinz. *Simulation of Rarefied Gasflows using the Lattice Boltzmann Method and Molecular Dynamics*. Diplom-Ingenieur, University of Stuttgart, Stuttgart, Germany, October 2008.
- [310] B. Chun and A. J. C. Ladd. Interpolated boundary condition for lattice Boltzmann simulations of flows in narrow gaps. *Physical Review E*, 75(6):066705–12, 2007.
- [311] National Institute of Standards and Technology. *Thermophysical Properties of Fluid Systems*, 2011.
- [312] T. Ohwada, Y. Sone, and K. Aoki. Numerical analysis of the Poiseuille and thermal transpiration flows between two parallel plates on the basis of the Boltzmann equation for hard-sphere molecules. *Physics of Fluids A*, 1(12):2042–2049, 1989.
- [313] T. Ohwada, Y. Sone, and K. Aoki. Numerical analysis of the shear and thermal creep flows of a rarefied gas over a plane wall on the basis of the linearized Boltzmann equation for hard-sphere molecules. *Physics of Fluids A*, 1(9):1588–1599, 1989.

-
- [314] C. Cercignani, M. Lampis, and S. Lorenzani. Variational approach to gas flows in microchannels. *Physics of Fluids*, 16(9):3426–3437, 2004.

List of publications

Journal articles

S. SCHMIESCHEK, A. V. BELYAEV, J. HARTING AND O. I. VINOGRADOVA.
Tensorial slip of superhydrophobic channels.
Physical Review E, 85:016324, 2012.

E. S. ASMOLOV, S. SCHMIESCHEK, J. HARTING AND O. I. VINOGRADOVA.
Flow past superhydrophobic surfaces with cosine variation in local slip length.
Physical Review E, 87:023005, 2013.

A. L. DUBOV, S. SCHMIESCHEK, E. S. ASMOLOV, J. HARTING AND O. I. VINOGRADOVA.
Lattice-Boltzmann simulations of the drag force on a sphere approaching a superhydrophobic striped plane.
The Journal of Chemical Physics 140:034707, 2014.

H. LIU, Q. KANG, C. R. LEONARDI, B. D. JONES, S. SCHMIESCHEK, A. NARVÁEZ, J. R. WILLIAMS, A. J. VALOCCHI AND J. HARTING.
Multiphase lattice boltzmann simulations for porous media applications - a review.
In press, 2015. pre-print available from arXiv:1404.7523 [physics].

S. SCHMIESCHEK, P. V. COVENEY AND J. HARTING.

Evaluation of a MRT lattice Boltzmann model for the simulation of surfactant-containing multiphase flows in porous media

in preparation, 2015.

S. SCHMIESCHEK, D. K. N. SINZ, F. KELLER, U. NIEKEN AND J. HARTING.

Mesoscopic simulation of diffusive contaminant spreading in gas flows at low pressure

in preparation, 2015.

Proceedings

S. SCHMIESCHEK, A. NARVÁEZ, J. HARTING.

Multi relaxation time lattice Boltzmann simulations of multiple component fluid flows in porous media.

High Performance Computing in Science and Engineering '12, 39-49, 2013.

List of figures

2.1	Illustration of the static contact angle and Young's law, Eq. (2.19). The contact angle is measured as the <i>inner</i> angle the droplet fluid component encloses with the surface. It can be related to the surface tensions $\gamma_{\alpha\bar{\alpha}}$ acting between the respective phases, solid <i>s</i> , liquid <i>l</i> and gas <i>g</i> . With zero gravity or for sufficiently small droplets, a spherical shape can be assumed. In this case the droplet Radius <i>R</i> and contact angle Θ can be calculated from the droplet base <i>B</i> and droplet height <i>H</i> via Eq. (2.20).	18
2.2	Illustration of the slip boundary condition with the slip length <i>b</i> as introduced by Navier. The slip length is the depth in which linear extrapolation of the surface velocity in relation to the shear stress at the surface hypothetically reaches zero.	19
2.3	The so-called D3Q19 lattice, comprising 19 velocities in 3 dimensions. Illustration adapted from [156].	24
3.1	Sketch of a slip stripe surface (a): $\Theta = \pi/2$ corresponds to transverse stripes, whereas $\Theta = 0$ to longitudinal stripes; (b) situation in (a) is approximated by a periodic cell of size <i>L</i> , with equivalent flow boundary conditions on the gas-liquid and solid-liquid interfaces. Illustration as published in [98], courtesy of A.V. Belyaev.	39
3.2	Sketch of a surface with a cosine relief and its equivalent representation in terms of flow boundary conditions. Illustration as published in [232], courtesy of E.S. Asmolov.	40
3.3	Illustration of the measurement of effective slip eigenvalues from lattice Boltzmann simulations. The velocity information of the whole domain is projected onto a single plane. To this cloud of data, Eq. (3.43) is fitted, effectively averaging the flow field over the whole channel. . . .	50
3.4	Eigenvalues of the effective slip length tensors simulated in the limit of a thin channel (symbols). The lines represent results of theoretical calculations by Eqs. (3.12) and (3.15). The data show that at small <i>b</i> the eigenvalues of \mathbf{b}_{eff} decrease as compared to a large local slip at the gas sector, and that the slip-length tensor becomes isotropic resulting in $\mathbf{b}_{\text{eff}}^{\perp,\parallel}$ to become hardly distinguishable in the $b = 10^{-3}H$ case. . . .	52

- 3.5 Downstream effective slip lengths of the thin channel simulated at $\phi_2 = 0.5$ for stripes inclined at different angle Θ (symbols). Lines are theoretically predicted downstream slip lengths calculated by using Eq. (3.1) [or Eq. (3.11)] with eigenvalues of \mathbf{b}_{eff} determined from numerical solutions of (3.28),(3.29) and (3.30),(3.31) 53
- 3.6 Downstream effective slip lengths of the thin channel simulated at $\phi_2 = 0.5$ in the limiting case the value of $b_{\text{eff}}^{(x)}$, for stripes inclined at different angle Θ (symbols). Lines are theoretically predicted downstream slip lengths calculated with Eq. (3.18). 54
- 3.7 Simulation results of eigenvalues of \mathbf{b}_{eff} as a function of fraction of gas sectors, ϕ_2 , in the limit of thick channel (symbols). Lines represent corresponding theoretical values obtained by a numerical solution of (3.28), (3.29) and (3.30), (3.31). Dash-dotted is the theoretical weakly slipping stripe solution, Eqs. (3.20),(3.23) as reported by Asmolov et al. in [245]. The inset shows the full curve including the full slip surface data point. 55
- 3.8 Effective downstream slip lengths for tilted stripes (in the thick channel limit) simulated at $\phi_2 = 0.5$ (symbols). All the lines are predicted theoretically downstream slip lengths. Calculated by using Eq. (3.1) [or Eq. (3.11)] with eigenvalues of \mathbf{b}_{eff} determined from numerical solutions of (3.28), (3.29) and (3.30), (3.31). 56
- 3.9 Effective downstream slip lengths for tilted stripes (in the thick channel limit) simulated at $\phi_2 = 0.5$ (symbols). Lines are theoretically predicted downstream slip lengths calculated with Eq. (3.25) with eigenvalues evaluated with Eqs. (3.21) and (3.24). 57
- 3.10 Effective downstream slip lengths at different channel thickness ($\phi_2 = 0.75$, $b/L = 5.0$). Symbols illustrate the simulation data, and curves show theoretical predictions. Deviations stem from varying discretisation artefacts for the relative slip lengths and channel heights and stripe periodicity. 58
- 3.11 Eigenvalues of the effective slip-length tensor as a function of b_1 simulated at fixed $b_0 = 1$ (symbols). The longitudinal effective slip length, $b_{\text{eff}}^{\parallel}$, is shown by circles, and the transverse effective slip b_{eff}^{\perp} is presented by diamonds. Solid and dashed curves denote the corresponding theoretical values obtained by numerical Fourier-series solutions. The asymptotic (isotropic) solution, Eq. (3.38), expected in the limit $b_0 \gg L$ is shown by the dash-dotted line. 59
- 3.12 Effective slip lengths computed for $b_1/b_0 = 0.5$, which correspond to a texture with no-slip lines, vs. average slip. The notations are the same as in Fig. 3.11. Dash-dotted and dotted lines show the effective lengths for longitudinal and transverse stripes as a function of $1/(3\phi)$ calculated with Eqs. (3.21),(3.24). 60

- 3.13 The cosine profile of the local slip length with $b_0/L = 5$, $b_1/b_0 = 0.5$ (solid curve) and the stripe profile with $\phi = 0.06$ (dashed line) with the same longitudinal effective slip lengths. 61
- 3.14 The velocities right along the wall for the textures with $b_1/b_0 = 1/3$, $b_0/L = 0.2$ (solid curve, diamonds), $b_0/L = 1$ (dashed curve, circles), $b_0/L = 5$ (dash-dotted line, crosses). Dotted curves show predictions of asymptotic formulae, Eqs. (3.36) and (3.35). 62
- 3.15 The normal velocity gradients along the wall for the textures with $b_1/b_0 = 1/3$, $b_0/L = 0.2$ (solid curve, diamonds), $b_0/L = 1$ (dashed curve, circles), $b_0/L = 5$ (dash-dotted line, crosses). Dotted curves show predictions of asymptotic formulae, Eqs. (3.36) and (3.35). . . . 62
- 3.16 The velocities along the wall for the no-slip textures $b_1/b_0 = 1/2$, $b_0/L = 0.2$ (solid curve, diamonds), $b_0/L = 1$ (dashed curve, circles), $b_0/L = 5$ (dash-dotted line, crosses). Dotted curves show predictions of asymptotic formulae, Eqs. (3.36) and (3.35). 63
- 3.17 The normal velocity gradients along the wall for the no-slip textures $b_1/b_0 = 1/2$, $b_0/L = 0.2$ (solid curve, diamonds), $b_0/L = 1$ (dashed curve, circles), $b_0/L = 5$ (dash-dotted line, crosses). Dotted curves show predictions of asymptotic formulae, Eqs. (3.36) and (3.35). . . . 64
- 3.18 Sketch of the simulated system. A sphere is approached towards a striped slip wall. Illustration as published in [233], courtesy of A.L. Dubov. 65
- 3.19 Vector field of horizontal velocity for $z = L/8$, $h = 3L/4$, grey and white regions correspond to no-slip and slip stripes, respectively. Courtesy of A.L. Dubov. 66
- 4.1 Illustration of the dipole model introducing a directional interaction component between fluids α and $\bar{\alpha}$ 72
- 4.2 Illustration of simulated systems used to measure the surface tension via the Laplace pressure in a pseudo-2d system. The post-processing defines the mean density of the droplet component α as black. This is emphasising the interface in renditions of the density data as the mean value is assumed only there. Depicted are system states for droplets initialised with discrete radii of 15, 20, 25, 30 and 35 lattice sites in a system with no surfactant and a coupling of $\mathcal{G}_{\alpha\bar{\alpha}} = 0.12$ in the steady state after 200,000 time steps. 77

4.3 Reproduction of the Young-Laplace law in a pseudo-2d system of size $128 \times 128 \times 2$. Plotted is the pressure difference across the surface of a droplet as determined by measurement of the lattice Boltzmann lattice density in the system centre and a corner point. The surface tension observed in the system increases with the coupling parameter $\mathcal{G}_{\alpha\bar{\alpha}}$ (see inset). Deviations in linearity can be attributed to slight differences in system initialisation pressures for different droplet sizes (As the droplet mass doubles as parameter for the pressure as well - compare Eq. (4.12)). Error bars of the curvature values are given by the deviations in droplet radius measurement due to the diffuse interface. The error is in particular pronounced for droplets with high curvature, i.e. small radii. 78

4.4 Surface tension as a function of the coupling parameter $\mathcal{G}_{\alpha\bar{\alpha}}$ for different initial surfactant densities $\rho_{\sigma}^{\text{init}}$, measured in a pseudo-2d droplet system. A consistent reduction in surface tension can be observed. The derivation of these values from perturbed surface tension data points increases the error observed to the order of 6 per cent. Nonetheless, the qualitative reduction of surface tension by added surfactant in the order of 40 to 50 per cent can be seen. 79

4.5 Illustration of over-saturation effects for initial surfactant densities larger than $\rho_{\sigma}^{\text{init}} = 0.25$ (Depicted is a snapshot for $\rho_{\sigma}^{\text{init}} = 0.30, \mathcal{G}_{\alpha\bar{\alpha}} = 0.12$). The interaction of the dipole field modelling the surfactant orientation introduces a dominant interaction alongside the lattice edges rendering the model nonphysical. The droplet radius in comparison to the simulation domain ($R = 35$ l.u. vs $X = 128$ l.u.) is contributing to the error as well. 80

4.6 Illustration of contact angle measurements in the dewetting regime. The post-processing defines the mean density of component α as black, emphasising the interface in renditions of the density data. Depicted are system states for droplet initialised with wall interactions of $\mathcal{G}_{\omega\alpha} = -\mathcal{G}_{\omega\bar{\alpha}} = 0.0, 0.005, 0.010, 0.015, 0.017, 0.018$ in a system with no surfactant and a coupling of $\mathcal{G}_{\alpha\bar{\alpha}} = 0.12$ in the steady state after 200,000 time steps. Nonphysical super critical interaction is observed for the strongest coupling strength, effectively repelling the droplet. 82

4.7 Illustration of contact angle measurements in the wetting regime. The post-processing defines the mean density of component α as black, emphasising the interface in renditions of the density data. Depicted are system states for droplet initialised with wall interactions of $\mathcal{G}_{\omega\alpha} = -\mathcal{G}_{\omega\bar{\alpha}} = 0.0, -0.005, -0.010, -0.015, -0.017, -0.018$ in a system with no surfactant and a coupling of $\mathcal{G}_{\alpha\bar{\alpha}} = 0.12$ in the steady state after 200,000 time steps. Film formation is observed for the strongest coupling strength. 82

- 4.8 The contact angle measured from the droplet geometry, Eq. (4.17) plotted over the wall coupling of the binary components $\mathcal{G}_{\bar{\alpha}\omega} = -\mathcal{G}_{\alpha\omega}$, compare section 2.5.2. for a fluid-fluid coupling strength of $\mathcal{G}_{\alpha\bar{\alpha}} = 0.12$. The prediction by Eq. (4.16) shows good agreement. For stronger attractive coupling, the local density field in the vicinity of the wall is increasingly distorted by the solid-fluid interactions, introducing a perturbation to the fluid density threshold in the prediction and subsequently a larger error in the geometry measurements. 84
- 4.9 Plot of the contact angle Θ over coupling strength $\mathcal{G}_{\alpha\omega}$ for different Surfactant concentrations. In the chosen parameterisation as a soluble surfactant with minimal wall interaction, an increase in contact angle is observed following from the reduction in fluid-fluid surface tension. While the dewetting case is matching the model prediction of Eq. (4.17) very well, the local density variations occurring in the boundary layer in the wetting case are leading to lower measured contact angles and larger uncertainty. The outlier In the maximally wetting case for the binary mixture results from interplay of the evaluation algorithm and the diffuse interface for very low contact angles. 85
- 4.10 Diffusivity \mathcal{D} over coupling strength $\mathcal{G}_{\alpha\bar{\alpha}}$ in lattice units. A clear linear correlation between the coupling parameter $\mathcal{G}_{\alpha\bar{\alpha}}$ and the diffusivity $\mathcal{D}_{\alpha\bar{\alpha}}$ is observed. The influence of even high surfactant concentration on the diffusive behaviour of the system is negligible. This is due to the homogeneous distribution of the surfactant component in the system, resulting in symmetrical interactions which cancel out. 86
- 4.11 Error in permeability measurement as calculated by Eq. (4.21) over the channel side-length B in lattice units. Depicted are two series for the BGK and TRT model, respectively. While for the TRT approach a small error depending linearly on the viscosity parameter is observed, for the LBGK model the error grows exponentially. For the TRT model the dependence should vanish completely [222], the nature of force implementation in our model reintroduces however a small deviation to be fixed in future work. 89
- 4.12 Error in permeability measurement as calculated by Eq. (4.21) over the shear viscosity relaxation parameter λ_ν . Depicted are three series for the BGK, TRT and simple MRT model, respectively. For the TRT approach a small error depending linearly on the viscosity parameter is observed while for the LBGK model the error grows exponentially. For the TRT model the dependence should vanish completely [222], the nature of force implementation in our model reintroduces however a small deviation to be fixed in future work. The simple MRT setup, where only the shear viscosity related relaxation rate is varied from one, exhibits even larger errors while the dependency on the parameter is still linear. See text for further discussion. 90

- 4.13 Relative permeability in a square duct for mixed and demixed binary fluid components over their mass fraction in the system. As errors in permeability measurement are of the same order for both the single component and mixture measurements, they cancel each other out in this case. Thus exact agreement between mass fraction and relative permeability is found for this simple model regardless of the presence of an interface in the measurement volume. 91
- 4.14 Illustration of the simulation domain, a pseudo-2D system measuring $x = 640, y = 2, z = 128$ lattice sites. In the region between the $x = 20$ and $x = 300$ solid columns of radius $R = 4$ lattice sites have been randomly placed, corresponding to a porosity of 1.68 in this region. In the initial state, the first half between $x = 0$ and $x = 320$ is filled with component α at a density of $\rho_\alpha = 0.7$. The latter half ranging from $x = 320$ to $x = 640$ is filled with component $\bar{\alpha}$ at a density of $\rho_{\bar{\alpha}} = 0.7$. The coupling strength is chosen to be $\mathcal{G}_{\alpha\bar{\alpha}} = 0.12$ throughout the simulations described. 92
- 4.15 Illustration of final states for different pressure gradients (Body force applied in the range $x = 0$ to $x = 20$). From left to right (in lattice units) $F = \{-1.0 \cdot 10^{-3}, -1.2 \cdot 10^{-3}, -1.4 \cdot 10^{-3}, -1.6 \cdot 10^{-3}, -1.8 \cdot 10^{-3}\}$. Respective time spans to the stationary state are given in Fig. 4.16. 93
- 4.16 Relative density of the displaced component α in the porous region $x = 20 \dots 300$ over simulation time for varied pressure gradients (driving force) in a neutrally-wetting system containing no surfactant. The body force, directly proportional to the pressure gradient in our model, was varied between $F = 1 \cdot 10^{-3}$ and $F = 2 \cdot 10^{-3}$. At lower pressure gradients flow is eventually inhibited by the resistance imposed through capillary forces. At higher pressures, a flow through the medium is established were a stable residual concentration of component α exists. Subsequently raised pressure reduces the residual fluid concentration, compare Fig. 4.15. 94
- 4.17 Relative density of the displaced component α in the porous region $x = 20 \dots 300$ over simulation time for wettability variation at a driving force of $F = 1.6 \cdot 10^{-4}$ in a system containing no surfactant. The contact angle of the displaced fluid was varied between $\Theta = 30^\circ$ and $\Theta = 150^\circ$ In the regime considered to drive the flow, even small wetting contact angles induce early arrest of the flow. In case of very high wettability ($\Theta = 30^\circ$), the fluid is stabilised in the medium and no flow is observed at all. At a very high contact angle of $\Theta \approx 150^\circ$, a change in the resulting differences in the stationary fluid distribution is observed. With vanishing friction in the system, the preferred path of flow changes and the structure of the residual fluid volume actually increases. 95

- 4.18 Relative density of the displaced component α in the porous region $x = 20 \dots 300$ over simulation time for varied inflow surfactant concentration at $F = 1.6 \cdot 10^{-4}$ and $\Theta = 90^\circ$. The concentration of surfactant species in the in-flowing fluid was varied between $\rho_\sigma = 0.0$ and $\rho_\sigma = 0.3$ 96
- 5.1 Volumetric flow rate through a simple channel as a function of the Knudsen number, normalised by the flow rate measured at $\text{Kn}=0.1$. Reproduction of a validation published by Zhang *et al.* [215]. The simulation results are obtained in a channel of 32 lattice units width. A finite slip boundary condition was employed both alone and with a viscosity correction accounting for a varying mean free path in the vicinity of a boundary [215, 230]. The reference values (symbols) are results of an exact solution to the linearized Boltzmann equation for hard spheres by Ohwada *et al.* [312, 313]. Using the combined boundary conditions good agreement can be obtained for the lower intermediate regime of $\text{Kn} \approx 0.05 \dots 0.5$ 111
- 5.2 Probability density of contaminant particle velocity for different system temperatures. Theoretical values are given by the Maxwell speed distribution for particles of a mass of 100 au at the respective temperature (Eq. 5.8). We find exact agreement with the theory, verifying the correct operation of the coupling algorithm (Sec. 5.2.2). 113
- 5.3 Particle density distribution at different times. All particles have been initialised in the point of origin. We find quantitative agreement with the theory (Fick's second law, Eq. 5.10) over a wide range of parameters. Here depicted is an example configuration; a system comprised of a Hydrogen atmosphere at $p = 3$ Pa and $T = 295$ K containing contaminants of mass $m_\zeta = 100$ au. The diffusivity is calculated according to Eqs. 5.11, 5.12 to $D_{\alpha\zeta} \approx 1.31 \cdot 10^{-2} \text{m}^2/\text{s}$ 114
- 5.4 Equilibrium particle density distribution in systems combining constant flow in positive x -direction and a diffusivity of $D_{\alpha\zeta} \approx 1.31 \cdot 10^{-2} \text{m}^2/\text{s}$. At $x/x_{\text{max}} = 1$ the system is delimited by a boundary acting on the contaminants (see section 5.2.2). The curves are given by the solution Eq. 5.15 to the transport equation assuming an infinite particle reservoir at $x > 1$ and an open boundary at $x < 0$. The simulation particle densities are re-normalised to the density measured 5 lattice sites in front of the wall. Outside of the boundary layer we find the differential equation 5.13 excellently approximated. The fluctuating densities due to thermalised reflection at the wall do however not justify the infinite reservoir assumption of the theory. This results in strong variation of the obtained result. 115
- 5.5 Illustration of the flow path through the system. The velocities are not to scale. In the centre opening, the velocity is up to three orders of magnitude larger than in the remainder of the system. 117

- 5.6 Gas flow rate as a function of the pressure gradient. The LB simulation has been parameterised to the kinematic viscosity $\nu = 3.581 \frac{\text{m}^2}{\text{s}}$ and speed of sound $c_s = 1280 \frac{\text{m}}{\text{s}}$ of Hydrogen gas at a mean pressure of $p = 4 \text{ Pa}$ and temperature $T = 295 \text{ K}$. A clear linear dependence of the flow rate \dot{Q} on the pressure gradient is found even at very high flow speeds violating the low Mach number assumption ($\text{Ma} \approx 0.27$). 118
- 5.7 Snapshot of simulation data at the lowest and highest flow rates, respectively 100,000 collision events into the simulation where a total of 10,000,000 collision events was simulated. The data is a histogram of the amount of particles present in the respective lattice layer volume. The total number of particles was 100,000. The suppression coefficient is calculated from fitting a constant function to these data in the ranges $x \in \{0.0050..0.0100\} \text{ m}$ and $x \in \{0.0175..0.0225\} \text{ m}$. The step deviations in the central region reflect that the data is not normalised for the variation in local volume in the geometry. In particular, the opening in the region $x \in \{0.015..0.0152\} \text{ m}$ is clearly visible as minimum. For the calculation of the suppression coefficient by Eq. (5.16) particle numbers left and right of the opening are simply summed. . 119
- 5.8 Measured suppression coefficients over varying flow rate through the opening. The suppression behaviour of the system can be approximated by an exponential relation to the flow rate observed in the system. 121

List of tables

2.1	Overview of some dimensionless numbers and their regimes.	21
3.1	Thin channel limit solutions of dual series (3.28),(3.29) and (3.30),(3.31) for the effective slip length tensor $b_{\text{eff}}^{(x)}$ and its maximum $b_{\text{eff}}^{\parallel}$ and minimum b_{eff}^{\perp} eigenvalues for channels with stripe slip pattern [98]. Considered are the limits of the channel height H and additional relations of local partial slip b and periodicity length L . The tensorial slip is governed by the respective smallest parameter. Additional parameters are the no-slip surface ratio ϕ_1 and partial slip surface ratio ϕ_2 as well as the inflow inclination Θ with respect to the pattern orientation.	42
3.2	Thick channel limit solutions of dual series (3.28),(3.29) and (3.30),(3.31) for the effective slip length tensor $b_{\text{eff}}^{(x)}$ and its maximum $b_{\text{eff}}^{\parallel}$ and minimum b_{eff}^{\perp} eigenvalues for channels with stripe slip pattern [98,245]. In addition, relations of local partial slip b and periodicity length L are considered. The tensorial slip is governed by the respective smallest parameter out of b , H and L	43
3.3	Domain size parameters according to Eq. 3.40, employed for the simulation of striped surfaces presented in section 3.4. The relative error introduced by the discretisation can be kept in the order of 10^{-3}	48
4.1	Overview of the moments, equilibria and relaxation parameters employed by different models. Different to models prominently reported on, the third order expansion equilibrium distribution, Eq. (2.4) yields additional terms $\propto \frac{j_i}{\rho^2} (j_j^2 \pm j_k^2)$ in the odd ordered energy flux related moments q and m . Weights are kept at the BGK parameterisation $w_\epsilon = 3, w_{\epsilon j} = -11/2$ and $w_{ww} = -1/2$ for all collision schemes.	76
5.1	Example numbers for arbitrary length scaling and Hydrogen at room temperature and 4 Pascal pressure obtained from the NIST chemistry webbook [311].	110

Summary

The dissertation is concerned with computer simulations of systems of fluid mixtures in interaction with solid boundaries. Three distinct groups of problems motivated by different technical applications are treated. These are the flow over patterned, superhydrophobic surfaces, the behavior of fluid mixtures in porous media and the behaviour of contaminant molecules in dilute gas flows. Inherently governed by microscopic effects, the systems share accessibility to modelling on the so-called mesoscopic scale. In the context of fluid dynamics the term designates the description of a fluid using (thermo-) statistics of microscopic systems to model emergent macroscopic effects while maintaining access to local properties.

Superhydrophobic surfaces are comprised of rough dewetting structures which enable the entrapment of gas between the surface and a fluid. This setup leads to remarkable properties, such as a high contact angle which allows droplets to roll over a surface as well as reduced friction of a fluid in contact with the surface where so-called slip, a non-zero velocity in the boundary layer is observed. The work on tensorial slip of channels with anisotropic patterns is focusing on the latter situation. Modeling entrapped gas by an effective slip, i.e. a finite velocity boundary condition fluid flow over anisotropic patterns (stripes) is simulated by the lattice Boltzmann method (LBM). This particular situation has been predicted to exhibit anisotropic tensorial slip not only resulting in an overall effective slip and reduced drag of the surface but capable of directing the flow as well. Furthermore this regime is not depending on the surface alone, but also on the height of a channel making it a channel property. In the scope of this work these predictions, relevant to the construction of microfluidic devices, are verified. The parameterisation and resolution requirements devised are applied to cosine varying anisotropic slip patterns and have informed simulations relevant to atomic force apparatus setups. This enables future comparison to experiments.

Enhanced oil recovery, soil process investigations, fuel cell construction and freeze dried food processing share the interest in multiphase flow of different fluid components such as water, oil and surfactants, in porous media. The discrete nature of the LBM and its extensibility to account for multiple fluid components makes it an ideal

candidate for modelling such systems. The popular lattice Bhatnagar Gross Krook (LBGK) formulation of the method allows the recovery of the Navier-Stokes equations (NSE) of fluid motion with a single relaxation time parameter. It has however been shown to have shortcomings with respect to the accuracy of boundary conditions. The single relaxation time introduces a dependency between the simulated fluid viscosity and the effective boundary position. This leads in particular for highly viscous fluids to large errors in the observed flow. The high surface to volume ratio in porous media is increasing the impact of this effect further. Multi relaxation time (MRT) collision schemes allow mending this problem. The work on a ternary multicomponent model for flows in porous media is concerned with the integration of a MRT scheme and a pseudopotential multicomponent LBM capable of simulating two immiscible fluid components (e.g. water and oil) as well as an amphiphilic (surfactant) fluid component. The implementation is verified to maintain valid physical modelling of surface tension and diffusivity effects while dramatically improving permeability measurements in highly viscous flows. It is found that future improvements to the force-integration can eliminate the error in certain systems altogether. The model is applied to basic parameter studies in a model pseudo-2d porous medium where forced imbibition in binary and ternary fluid systems is considered.

In most conditions encountered by humans, the individual movement of molecules can be neglected in favour of sole statistical treatment. Modern developments, such as space exploration and vacuum technology used in research and manufacturing systems, are including the so-called Knudsen regime where the mean free path of individual particles becomes of the order of system scales and continuum approximations are no longer valid. This is true in chip fabrication lithography where the complex optical systems required for resolving structures on the nanometer scale are flushed with hydrogen gas at low pressures of some Pascal to minimize disturbance of the light paths. Unfortunately plastic parts used in the setups emit under these conditions single organic molecules which over time agglomerate on the lens surfaces and cause so-called hazing. The desire to control and ideally avoid hazing motivates the investigation of contaminant transport processes in low pressure environments. In order to account for non-continuum effects a hybrid method has been set up by integrating a particle model based on the direct simulation Monte Carlo (DSMC) approach with a LBM modified to include the phenomenology of Knudsen effects for the atmospheric flow. Here most interaction can be neglected and only collisions of contaminants and background gas are relevant. This dramatically increases the efficiency of the method. The implementation is tested for consistency by quantitative evaluation of the Maxwell Boltzmann distribution and advection diffusion accessible to theory. The model is applied to the simulation of contaminant suppression by low pressure flows in example geometries relevant to technical applications. The results obtained here will allow for future comparison to experimental results.

In particular on the mesoscopic scale, coarse grained computer simulation models

are developing quickly towards tools capable of aiding design and understanding of real fluid systems. Besides the ever growing available computational power, a key ingredient to this development is a deeper understanding of fluid dynamics, as it allows to manage complexity and to enable more efficient use of calculations. While dealing with a subset, this work has touched all aspects of optimisation, increasing complexity to gain accuracy and stability at points, while radically simplifying system aspects not relevant to the parameters of interest in others.

Samenvatting

Dit proefschrift betreft computersimulaties van systemen bestaande uit meerdere vloeistoffen, die interacties aan gaan met vaste grensvlakken. Drie types problemen worden behandeld, gemotiveerd door verschillende technische toepassingen: Stroming over oppervlakken met superhydrofobische patronen, het gedrag van vloeistofmengsels in poreuze media, en het gedrag van ongewenste moleculen in verdunde gasstromingen. Hoewel deze gedragingen bepaald worden door microscopische effecten lenen zij zich toch voor modellering op mesoscopische schalen. In de context van de vloeistofdynamica betekent dit het gebruik van (thermo-)statistiek van microscopische systemen om de hieruit voorkomende macroscopische effecten te modelleren, en toch ook nog toegang te hebben tot lokale eigenschappen.

Superhydrofobische oppervlakken bestaan uit ruwe waterafstotende structuren die kunnen leiden tot de opsluiting van gas tussen het oppervlak en een vloeistof. Dit leidt tot opmerkelijke eigenschappen, zoals een grote contacthoek die toelaat dat druppels over een oppervlak rollen, en verminderde weerstand van een vloeistof in contact met het oppervlak, waardoor de snelheid van de vloeistof in de grenslaag niet nul is: de zogenoemde 'slip'. Het onderzoek naar tensorische slip in kanalen met anisotrope patronen (strepen) richt zich op deze tweede situatie. Het modelleren van opgesloten gas door een effectieve slip - een randvoorwaarde waarbij de vloeistofstroming een eindige snelheid heeft - gebeurt door middel van de rooster-Boltzmann methode. Over deze configuratie is voorspeld dat zich anisotrope tensorische slip voordoet, wat niet alleen leidt tot een effectieve slip en verminderde weerstand, maar ook de richting van de stroming kan sturen. Dit hangt niet alleen af van het oppervlak, maar ook van de hoogte van het kanaal, zodat dit beschouwd kan worden als een kanaaleigenschap. In het kader van dit werk worden deze voorspellingen, die van belang zijn bij het maken van microfluidische apparaten, getoetst. De eisen die de parametrisatie en resolutie stellen worden toegepast op anisotrope slip die varieert als een cosinus. Verder wordt het gebruik van deze resultaten voor simulaties waarin bollen oppervlakken met superhydrofobische patronen naderen besproken. De gepubliceerde resultaten zijn van belang voor opstellingen met atoomkrachtmetingen.

De stroming van mengels van meerdere vloeistoffen, zoals water, olie, en oppervlakte-actieve stoffen in poreuze media is van belang voor uiteenlopende processen, zoals verbeterde oliewinning, het onderzoeken van bodemprocessen, het maken van brandstofcellen en het verwerken van gevriesdroogd voedsel. Omdat de rooster-Boltzmann methode discreet is, en makkelijk uitbreidbaar naar de simulatie van meerdere vloeistoffen, is deze methode uitermate geschikt voor het modelleren van zulke systemen. Met de populaire rooster-Bhatnagar-Gross-Krook formulering van deze methode kunnen de Navier-Stokes vergelijkingen worden teruggevonden, maar alleen met een enkele relaxatie-tijd parameter. Dit is niet altijd genoeg voor de gewenste nauwkeurigheid van randvoorwaarden: Door de enkele relaxatie-tijd is er een afhankelijkheid tussen de viscositeit van de gesimuleerde vloeistof, en de effectieve positie van de randvoorwaarden. In het bijzonder voor vloeistoffen met hoge viscositeit leidt dit tot grote fouten in de berekende stroming. Het relatief grote oppervlak ten opzichte van het vloeistofvolume in poreuze media maakt dit probleem nog groter. Multi-relaxatie-tijd botsingsschema's verhelpen dit probleem. Het werk aan een ternair multicomponentmodel voor stromingen in poreuze media betreft het samenvoegen van een multi-relaxatie-tijd schema met een pseudo-potentiaal rooster-Boltzmann methode, die zowel twee onmengbare vloeistoffen (bijvoorbeeld water en olie) als een amfifiele (oppervlakte-actieve) vloeistofcomponent kan simuleren. Deze implementatie zorgt voor correcte modellering van oppervlaktespanning en diffusie-effecten, en verbetert de meting van permeabiliteit voor hoogvisceuze vloeistoffen sterk. Het is gebleken dat toekomstige verbeteringen aan de integratie van de krachten de fout in bepaalde systemen geheel kunnen wegnemen. Het model is toegepast op een pseudo-tweedimensionaal poreus medium waarbij het gedwongen opzuigen van binaire en ternaire vloeistofmengsels wordt bestudeerd.

Op de meeste menselijke schalen kunnen de individuele bewegingen van moleculen worden verwaarloosd en kan de collectieve beweging op een statistische manier behandeld worden. Nieuwe ontwikkelingen, zoals ruimtevaart en vacuümtechnologie gebruikt in onderzoeks- en productiesystemen vinden plaats in het Knudsen-regime, waar de vrije weglengte van losse deeltjes zo lang wordt als andere schalen in het systeem en continuümbenaderingen niet meer geldig zijn. Dit doet zich voor in lithografie voor de productie van chips, waarbij de complexe optische systemen die nodig zijn voor het behalen van de resolutie die nodig is voor het maken van structuren op de nanometer-schaal doorgespoeld worden met waterstofgas onder lage druk van enkele Pascal, om zo een minimale verstoring van de lichtweg te hebben. Helaas stoten plastic onderdelen in deze opstellingen onder deze omstandigheden losse organische moleculen uit. Deze slaan in de loop van de tijd neer op de lenzen en veroorzaken vertroebeling. De wens om dit proces te beheersen, of idealiter te vermijden, is de motivatie achter het bestuderen van transportprocessen van ongewenste deeltjes in een lage-druk omgeving. Een hybride-methode gebaseerd op directe Monte Carlo simulatie van de deeltjes, gekoppeld aan een rooster-Boltzmann model, aangepast om Knudsen-effecten voor de gasstroming in acht te nemen, is ontwikkeld om de

niet-continuüm eigenschappen te kunnen simuleren. De meeste interacties kunnen hierbij verwaarloosd worden: alleen de botsingen van de deeltjes met het gas zijn van belang. Dit verhoogt de efficiëntie van de methode enorm. De implementatie is getest op consistentie door quantitative analyse van de Maxwell-Boltzmann distributie en advection/diffusie die theoretisch beschreven kan worden. Het model is toegepast op de onderdrukking van ongewenste deeltjes door stromingen onder lage druk in voorbeelden van geometrieën die relevant zijn voor technische toepassingen. De hier verkregen resultaten kunnen in de toekomst gebruikt worden voor vergelijking met experimentele resultaten.

In het bijzonder op de mesoscopische schaal ontwikkelen grofkorrelige computersimulaties zich snel tot gereedschappen die kunnen helpen bij het ontwikkelen en begrijpen van echte vloeistofsystemen. Naast de immer toenemende beschikbare rekenkracht is een beter begrip van vloeistofdynamica belangrijk, omdat zo de rekenkracht beter benut kan worden. Dit werk heeft beide aspecten van optimalisatie benut: waar nodig is de complexiteit verhoogd voor betere nauwkeurigheid en stabiliteit, en waar mogelijk zijn aspecten die niet van belang zijn voor de relevante resultaten sterk versimpeld.

Acknowledgements

The work that culminated in this document was performed in Germany, the Netherlands and the United Kingdom and has involved many people on various levels without whom you would not hold this thesis in hand.

First and foremost I like to thank Jens Harting for the opportunity to work with him towards the doctorate. Your guidance and feedback are very much appreciated. Special thanks as well to Peter for providing the opportunity to visit London as well as initialising and enabling my final push towards the finishing of the thesis.

Thank you to the members of the committee Olga Vinogradova, Anton Darhuber, Peter Coveney, Federico Toschi, Jacco Snoeijer and Hermann Clercx for their positive comments on the thesis and their willingness to participate in the defense ceremony.

Many thanks to my all my co-authors, especially Evgeny Asmolov, Alexey Belyaev and Alexander Dubov and Olga Vinogradova for their excellent theoretical and experimental work on anisotropically patterned surfaces, Ariel Narvaez and Jens Harting for discussions and work on multiphase LBM and David Sinz' work on and support with modelling low pressure multicomponent systems.

Also in numerical work technical support cannot be valued high enough. Thank you to Frank Huber in Stuttgart and Henni Manders and Jorgen van der Veen in Eindhoven. The same is true for administrative tasks where I am very grateful to Henriette Patzelt, Brigitte van de Wijdeven and Sofia Shamim in Stuttgart, Eindhoven and London, respectively.

I would like to thank all my colleagues whom I spent time with at the ICP in Cascade and at the CCS - A list like this is almost ought to be incomplete, so you feel forgotten I am sure I will notice at some point in time as well. Thank you to: Aghastya, Aniruddha, Andrea D, Andrea S, Anjan, Ariel, Badr, Ben, Berend, Calin, Charlotte, Christian, Dave, David, Dennis, Derek, Florian D, Florian F, Florian G,

Florian J, Francesca, Frank R, Gary D, Gary M, Güneş, Ghazaleh, Hans-Jörg, Hugh, Humberto, James H, James S. Jorge, Judith, Konrad, Laura, Lionel, Luca, Maarten, Mayeul, Mico, Miguel, Myra, Nadezhda, Nelly, Oliver, Oleksii, Owen, Pedro, Raoul, Riam, Rudolf, Rupert, Samantha, Serge, Simon C, Sofia, Stefan F, Stefan K, Sudhir, Tatyana, Theo, Thomas and Ulf. Then there is life outside of and around university where in addition to the intersecting colleagues I like to mention Audrey, Björn, Boris, Brice, Christine Güney, Gregor, Irene, Jochen, Julien, Michael, Michiel, Nathan, Otti, Sanne and Shani for shared time, friendship, music, fun and life and love - you know who you are.

Very special thanks to Stefan Frijters who is a brilliant person, amongst other things to share CC 3.12 with, and who as well was so nice to translate the summary of this thesis to Dutch.

Mamschen und Bobschen, vielen vielen Dank fuer Eure Liebe, Inspiration, unerschütterlichen Glauben und Unterstützung auf diesem Weg.

Thank you Anna, for motivation and being you and patient with me during the months of writing.

Finally, research and personal development require material means as well. Thank you for funding to the Eindhoven University of Technology, the University of Stuttgart, UCL and Zeiss, support by the JMBC research school for Fluid mechanics and HPC-Europa2 and UKCOMES as well as SARA, HLRS and the JSC and EPCC for computing time.

Curriculum Vitae

- 11.December 1979 **Born** in Göttingen, Germany
- 1991 - 1999 **Highschool education**
Georg-Christoph-Lichtenberg Gesamtschule, Göttingen, Germany
Abitur (General qualification for university entrance)
- 2000 - 2001 **Alternative civilian service**, Domiciliary care
German Red Cross, Göttingen, Germany
- 2001 - 2002 **Diploma programme** (M.Sc. with thesis) Technical cybernetics
University of Stuttgart, Stuttgart, Germany
- 2002 - 2008 **Diploma programme** (M.Sc. with thesis) Physics
University of Stuttgart, Stuttgart, Germany
Topic: *Lattice-Boltzmann simulation of multiphase flows in microfluidics*
Supervisor: Prof.dr. J.D.R. Harting
Graduation: 08. October 2008
- 2008 - 2009 **Graduated scientific assistant**
Fraunhofer Gesellschaft, Institut für Produktionstechnik und Automatisierung IPA, Stuttgart, Germany
- 2009 - 2011 **PhD programme** Computational physics
University of Stuttgart, Stuttgart, Germany
- 2011 - 2012 **Staff Associate**
University College London, London, United Kingdom
- 2012 - 2013 **PhD programme in applied physics**
Eindhoven University of Technology, Eindhoven, The Netherlands
Topic: *Computer simulation of boundary effects and multiphase flows on the mesoscopic scale*
Supervisor: Prof.dr. J.D.R. Harting
- 2013 - present **Research Associate**
University College London, London, United Kingdom

$\langle \dots \rangle$	Mean value	\mathcal{L}	Characteristic length
$ \mathbf{a} $	Vector value	m	Mass
$\mathbf{a} \cdot \mathbf{b}$	Scalar product	m_i	Stochastical moment
$\alpha, \bar{\alpha}$	Immiscible fluid components	Ma	Mach number
\mathbf{a}	Acceleration	\mathcal{M}	Transformation matrix
A	Area	ν	Shear viscosity
b	Slip length	ν^ν	Bulk viscosity
$b_{\text{eff}}^{(x)}$	Effective slip tensor	n	Particle density
$b_{\text{eff}}^\perp, b_{\text{eff}}^\parallel$	Min/max EV of effective slip	$n\mathbf{x}$	Maximum lattice coord.
B	Width (droplet/channel)	N	Particle count
χ	concentration	ω	Wall pseudodensity
\mathbf{c}	Lattice Velocity	Ω	Collision integral/operator
c_s	Speed of sound	π	\propto Viscous stress tensor
Ca	Capillary number	ψ	pseudoPotential
Δ	Laplace operator	p	Pressure
\mathbf{d}	Dipole moment	\mathbf{p}	Viscous stress tensor
d	Diameter	Pe	Peclét number
D	Number of dimensions	q	energyFlux
\mathcal{D}	Diffusivity	\dot{Q}	Mass flux
ϵ	Kinetic energy squared	ρ	Mass density
ϵ	Error value	ρ	Lattice density
$\dot{\epsilon}$	Strain rate	R	Radius
η	Viscosity tensor	Re	Reynolds number
η	Dynamic viscosity	σ	Deviatoric stress
e	Kinetic energy	σ	collisionalCrossSection
ϕ_1	No-slip area fraction	σ	Surfactant component
ϕ_2	Partial slip area fraction	s	Wall potential
Φ	Surface of unit sphere	\mathcal{S}	Relaxation matrix
ϕ	Number of components	\mathcal{S}	Suppression coefficient
f	Probability distribution	θ	Dipole weights
\mathbf{F}	Force	Θ	Inflow angle
γ	Surface tension	Θ	Contact angle
G	Free energy	τ	Relaxation time
\mathcal{G}	Coupling coefficient	T	Temperature
H	Height	Δt	Time step
\mathcal{J}	Unit tensor	u	Speed
\mathbf{j}	Momentum	\mathbf{u}	Velocity
κ	permeability	\mathcal{U}	Characteristic Velocity
k	Curvature	V	Volume
k_B	Boltzmann constant	w	Lattice weights
Kn	Knudsen number	Δx	Lattice discretisation
λ_0	Mean free path	\mathbf{x}	point
λ	Relaxation parameter	x, y, z	Cartesian coordinates
L	(Periodicity) Length	ζ	accommodationCoefficient